University of Nottingham
UK | CHINA | MALAYSIA

Observational Constraints on Primordial Black Hole Dark Matter

Thesis submitted to the University of Nottingham for the degree of **Doctor of Philosophy, September 2024.**

Matthew Gorton

Student ID: 10094533

Supervised by

Professor Anne Green

Abstract

In spite of compelling evidence for its existence and great experimental efforts to detect it, the nature of dark matter remains unknown. One scenario is that some or all of the dark matter consists of black holes formed from the collapse of highly overdense regions in the early Universe. Observational constraints on these 'primordial black holes' (PBHs) appear to exclude PBHs from making up all of the dark matter unless their mass, $M_{\rm PBH}$, lies in the range $10^{17}\,{\rm g} \lesssim M_{\rm PBH} \lesssim 10^{22}\,{\rm g}$, often known as the 'asteroid-mass window'. In this thesis we investigate the impact of assumptions made when calculating observational constraints on PBHs.

Firstly, we consider the effect of PBH clustering on microlensing constraints. Clustering of PBHs occurs to a greater extent than for standard cold dark matter on small scales. For PBHs formed from the collapse of large gaussian fluctuations, we find clustering has only a small effect on microlensing constraints even for very massive PBHs ($M_{\rm PBH} \sim 10^3 M_\odot$) for which the effect of clustering is largest.

Constraints on PBHs are usually obtained assuming all PBHs have the same mass, though accounting for critical collapse shows they would have an extended mass function. A lognormal fit has been widely used to parameterise the PBH mass function, though recent work has shown that other functions provide a better fit. We recalculate both current and prospec-

tive future constraints on PBHs with these improved fitting functions, to assess to what extent the asteroid-mass window remains open. For current constraints, the window is narrowed, though there remains a region where PBHs can make up all of the dark matter. Future constraints from evaporation and microlensing may together exclude all of dark matter being made of PBHs if the PBH mass function is sufficiently wide.

Acknowledgements

I could not have made it this far without the help and patience of a great number of people.

I am deeply grateful to my supervisor, Professor Anne Green. Your guidance, depth of knowledge, support and insight throughout this PhD has been invaluable. Thank you for keeping me on track and providing your judgement on what to pursue and what to avoid.

I would also like to extend my thanks to Swagat Mishra for your encouragement and insightful discussions, and to Andrew Gow for providing the data on (and answering my questions about) the mass functions used in Chapter 3.

I am thankful to everyone else in Nottingham, both in CAPT and beyond, who has supported me throughout this PhD. Thank you especially to Brad, CB, Chad, Dan, Jacob, James S, James W, Karel, Kellie, Kieran, Lauren, Lizzie, Jen, Joe, Mick, Mikey, Miquel, Molly, Roan, Sergio, Simon, Sukhi and Tomáš, for your friendship and camaraderie.

To the Lancaster lot, thank you Charlie and Ciara for making sure we continue to meet up, and to Andrew, Gurrashpal and Joe, for the board game sessions that provided much-needed joy during the long lockdown evenings early in my PhD. To you and the rest of the NB — Anna, Harry, Henry and Luke — thank you for the type-1 and type-2 fun, which often involved getting drenched half way up a mountain. I'd also like to thank Jim and Laura for your advice and for educating me about terrible (but entertaining) films.

Finally, I want to express my deepest appreciation to Mum and Dad for their unwavering support. This thesis is dedicated to you.

Declaration

All scientific results in this thesis were obtained solely by me. No part of this thesis has previously been submitted for a degree or other qualification at this or any other university.

The work contained in Chapter 2 has been published in:

- M. Gorton and A. M. Green. "Effect of clustering on primordial black hole microlensing constraints." *JCAP*, 08.08 (2022) p. 035. arXiv: 2203.04209 [astro-ph.CO]

The work contained in Chapter 3 has been published in:

- M. Gorton and A. M. Green. "How open is the asteroid-mass primordial black hole window?". *SciPost Phys.* 17 (2024) p. 032 (2024), 2403.03839 [astro-ph.CO]

Contents

Chapter 1

Introduction

1.1 Cosmology

In this section we briefly overview the aspects of cosmology most relevant to this thesis. We present the background required to explain the evidence for dark matter and also discuss inflation, which provides a mechanism for generating perturbations that can seed large-scale structure and, potentially, produce primordial black holes. For a more detailed introduction, see e.g. the book by Liddle & Lyth (Ref. [1]).

1.1.1 The homogeneous and isotropic Universe

In the standard scenario, our Universe is postulated to have been extremely hot and dense at early times and has since expanded and cooled (the Big Bang).

A key concept underlying observational cosmology is the cosmological principle. This states that, on sufficiently large scales, the Universe is well-

described as being spatially homogeneous (the same everywhere) and isotropic (the same in every direction). The spatial homogeneity and isotropy of the Universe requires that the line element takes the form (in polar coordinates) [1]

$$\mathrm{d}s^2 = -\mathrm{d}t^2 + a^2(t)\left[\frac{\mathrm{d}r^2}{1-Kr^2} + r^2\mathrm{d}\Omega^2\right], \tag{1.1}$$

where t is the coordinate time, $a(t)$ is the scale factor, K is the intrinsic spatial curvature of the Universe and the spatial coordinates are comoving. The following possibilities are allowed: $K = 0$ describes a flat universe (a Euclidean space), $K > 0$ describes a closed universe with positive spatial curvature and $K < 0$ describes an open universe with negative spatial curvature.

The expansion rate is quantified by the Hubble parameter $H \equiv \dot{a}/a$, where $a(t)$ is the scale factor and the overdot denotes a time derivative. The Hubble parameter is related to the energy density of the Universe, ρ, by the Friedmann equation,

$$H^2 = \frac{8\pi G\rho}{3} - \frac{K}{a^2} + \frac{\Lambda}{3}, \tag{1.2}$$

where G is the gravitational constant and Λ is the cosmological constant. The energy density of each component of the Universe (such as matter and radiation) evolves according to the fluid equation,

$$\dot{\rho} + 3H\left(\rho + P\right) = 0, \tag{1.3}$$

where P is its pressure. Most of these components are described by a constant equation of state parameter $w = P/\rho$, in which case Eq. (1.3) can

[1] Here, and throughout this thesis, we use natural units with $\hbar = c = k_{\mathrm{B}} = 1$ and the $(-,+,+,+)$ metric signature.

be solved to obtain

$$\rho \propto a^{-3(1+w)}. \tag{1.4}$$

The most commonly-considered sources of energy density in the Universe are non-relativistic matter ($w = 0$), radiation ($w = 1/3$) and dark energy. Dark energy drives the late-time accelerated expansion of the Universe, which was first demonstrated by observations of the apparent brightnesses of distant type-Ia supernovae [2, 3]. These observations and others, such as those from temperature anisotropies in the cosmic microwave background (CMB) (see Sec. 1.1.3 and Sec. 1.2.1) and galaxy surveys, indicate that dark energy provides most of the Universe's energy density today and that it has an equation of state parameter $w \approx -1$ [4, 5]. This is consistent with the effect of a non-zero cosmological constant, which can be written as a constant contribution to the energy density, $\rho_\Lambda \equiv \Lambda/(8\pi G)$, with an equation of state parameter $w = -1$. In the concordance cosmological model (ΛCDM), the main sources of energy density in the Universe today are in the form of a cosmological constant, Λ, and non-relativistic matter mostly in the form of cold dark matter (CDM). We will introduce dark matter in more detail at the end of this section and in Sec. 1.2.

From Eq. (1.4), the energy densities of matter ($w = 0$) and radiation ($w = 1/3$) evolve with the scale factor a as

$$\rho_{\rm m} \propto a^{-3}, \tag{1.5}$$

$$\rho_{\rm r} \propto a^{-4}. \tag{1.6}$$

Observations of temperature anisotropies in the CMB by the Planck satellite and observations of galaxies show the Universe is close to spatially flat [4]. We therefore assume spatial flatness (i.e. $K = 0$) throughout the rest of this thesis. In a spatially flat Universe, Eqs. (1.2) and (1.3) have

simple solutions when the Universe is dominated by matter or radiation. For a matter-dominated Universe:

$$\rho \propto a^{-3}, \quad a \propto t^{2/3}. \tag{1.7}$$

For a radiation-dominated Universe:

$$\rho \propto a^{-4}, \quad a \propto t^{1/2}. \tag{1.8}$$

A universe with density equal to the critical density,

$$\rho_{\rm crit} = \frac{3H^2}{8\pi G}, \tag{1.9}$$

is spatially flat (as can be seen from Eq. (1.12)). It is convenient to define the present-day energy density of a component i as a fraction of the present-day critical density, which is known as the density parameter,

$$\Omega_i \equiv \frac{\rho_{i,0}}{\rho_{\rm crit,0}}, \tag{1.10}$$

where we use the subscript 0 to denote a quantity evaluated at the present time, $t = t_0$.

Observations of the anisotropies in the cosmic microwave background (see Sec. 1.1.3 and Sec. 1.2.1) give the following values for the density parameters of the cosmological constant, matter and radiation in the ΛCDM model [4]

$$\Omega_\Lambda \approx 0.69, \quad \Omega_{\rm m} \approx 0.31, \quad \Omega_{\rm r} \approx 9.2 \times 10^{-5}. \tag{1.11}$$

Although the cosmological constant is the largest contributor to the energy density today, the energy densities of matter and radiation dominated at early times. This is because the energy density associated with the cosmo-

logical constant is fixed, while the energy densities of matter and radiation increase as one goes back in time. One can therefore neglect the cosmological constant term in the Friedmann equation (Eq. (1.2)) at early times and write

$$H^2 \simeq \frac{8\pi G\rho}{3} - \frac{K}{a^2}, \tag{1.12}$$

where ρ only includes the energy densities of matter and radiation.

Since the energy density of radiation decreases faster than that of matter, at sufficiently early times radiation is the dominant contribution to the energy density in the early Universe. From Eqs. (1.5) and (1.6), $\rho_{\rm m}/\rho_{\rm r} \propto a$. Using the density parameters from Eq. (1.10) gives the scale factor at the time when the energy densities of matter and radiation were equal ('matter-radiation equality'),

$$\frac{a_{\rm eq}}{a_0} \approx 2.9 \times 10^{-4}, \tag{1.13}$$

where a_0 is the present value of the scale factor.

Observations of the abundance of light nuclei (see Sec. 1.1.2) and cosmic microwave background anisotropies (see Sec. 1.2.1) indicate that the density parameter of visible (often known as 'baryonic') matter is $\Omega_{\rm b} \approx 0.05$, much smaller than $\Omega_{\rm m}$. These observations, as well as those of galactic rotation curves (see Sec. 1.2.1), galaxy clusters (see Sec. 1.2.1), and large-scale structure (see Sec. 1.2.1) indicate that the majority of the matter in the Universe is 'dark'. The nature of this 'dark matter' remains unknown. It is most often considered to be an undiscovered particle species, with popular candidates including weakly interacting massive particles (WIMPs) and axions (see Sec. 1.3). In this thesis, we will focus on the alternative scenario that the dark matter consists (at least in part) of black holes formed in the early Universe, so-called 'primordial black holes' (PBHs). Next, we outline the relevant background to the evidence for dark matter (nucleosynthesis

(Sec. 1.1.2), the cosmic microwave background (Sec. 1.1.3) and structure growth (Sec. 1.1.4) before briefly reviewing cosmic inflation in Sec. 1.1.5.

1.1.2 Nucleosynthesis

The primordial abundances of light nuclei are well-predicted by applying nuclear physics in the first few minutes after the Big Bang (see Refs. [6–8] for reviews). In the absence of any physics beyond the Standard Model, the only free parameter in these calculations is the baryon-to-photon ratio, i.e. the present-day ratio of the number densities of baryons and photons, $\eta \equiv n_{\mathrm{b},0}/n_{\gamma,0}$. The baryon-to-photon ratio can therefore be determined by comparing theoretical predictions of the abundances of light nuclei to observations, in particular the abundance of deuterium. This gives $\eta \approx 6 \times 10^{-10}$ [9], corresponding to $\Omega_{\mathrm{b}} h^2 \approx 0.02$ [10, 11], where $h \equiv H_0/(100\,\mathrm{km\,s^{-1}\,Mpc^{-1}})$. Using $H_0 = 67.4\,\mathrm{km\,s^{-1}\,Mpc^{-1}}$ [4] gives $\Omega_{\mathrm{b}} \approx 0.05$.

1.1.3 Cosmic microwave background

The cosmic microwave background (CMB) is an almost-exact black body [12] of microwave photons with temperature $T_0 = 2.725\,\mathrm{K}$ [13]. The CMB photons provide a snapshot of the Universe around 400,000 years after the Big Bang. The small anisotropies in the CMB temperature, which are of order $\Delta T/T \sim 10^{-5}$ [14], are an especially powerful cosmological probe.

In the early Universe, photons and baryons were tightly coupled by Thomson scattering, forming a 'baryon-photon plasma'. Once the Universe had cooled sufficiently for neutral atoms to form (an event known as 'recombination'), the scattering rate of photons greatly decreased (known as 'de-

coupling'). Since then, the photons have travelled essentially freely, so the CMB reflects the conditions from the period just before decoupling. The hotter and colder regions in the CMB correspond to overdense and underdense areas in the plasma density, respectively.

CMB observations have played a crucial role in our modern understanding of the Universe's geometry and its contents. Its near-uniform temperature and black body spectrum show that baryonic matter and radiation in the early Universe were in thermal equilibrium, providing an important motivation for inflation (see Sec. 1.1.5). Analysis of CMB temperature anisotropies suggests that the Universe is close to spatially flat (see Sec. 1.1.1) and (of greater relevance to this thesis) offers crucial evidence for the existence of dark matter (see Sec. 1.2.1). Additionally, CMB anisotropies and observational limits on the deviation of the CMB from a black body spectrum constrain the abundance of primordial black holes (see Sec. 1.4.5).

1.1.4 Structure growth

Structures in our Universe, such as galaxies, form from the gravitational collapse of small initial overdensities with a slightly higher temperature than average. These density perturbations are quantified by the density contrast $\delta = (\rho - \bar{\rho})/\bar{\rho}$, where ρ is the density of the perturbation and $\bar{\rho}$ is the average density of the background Universe.

We first consider the evolution and statistics of the density contrast in linear theory (applicable when $\delta \ll 1$). It is helpful to consider the evolution of the density contrast in Fourier space since each Fourier mode, $\delta(\mathbf{k}, t)$ (where $\mathbf{k}$ is the comoving wavevector), evolves independently in lin-

ear theory. Dark matter perturbations can only grow once their associated comoving wavenumber, $k \equiv |\mathbf{k}|$, 'enters the horizon' [2], which occurs when k^{-1} is smaller than the comoving Hubble radius $1/(aH)$, i.e. $k = aH$. The growth of dark matter overdensities on scales smaller than the Hubble radius is negligible during the radiation-dominated epoch but after matter-radiation equality they grow as $\delta \propto a$. Growth of baryonic perturbations can only occur after decoupling, since baryons are tightly coupled to photons beforehand.

The matter power spectrum, $P_\delta(k,t)$, quantifies the amplitude of the density perturbations as a function of scale. It is defined through the ensemble average of the Fourier modes of the density contrast

$$\langle \delta(\mathbf{k},t)\delta^*(\mathbf{k}',t)\rangle = (2\pi)^3\delta_{\rm D}(\mathbf{k}-\mathbf{k}')P_\delta(k,t), \tag{1.14}$$

where the superscript $*$ denotes complex conjugation and $\delta_{\rm D}(\mathbf{k}-\mathbf{k}')$ is the Dirac delta function.

Commonly, one considers the dimensionless power spectrum (often also referred to as simply the 'power spectrum'), defined as

$$\mathcal{P}_\delta(k,t) \equiv \frac{k^3}{2\pi^2}P_\delta(k,t). \tag{1.15}$$

The dimensionless power spectrum is related to its value at some initial time $t_{\rm i}$ (the 'primordial power spectrum' $\mathcal{P}_\delta(k,t_{\rm i})$), by

$$\mathcal{P}_\delta(k,t) = T^2(k,t)\mathcal{P}_\delta(k,t_{\rm i}), \tag{1.16}$$

where $T(k,t)$ is the transfer function, which describes the evolution of the

[2]Dark matter perturbations can grow outside of the horizon in certain gauges, but this is an artifact of the gauge choice.

density perturbations.

Most commonly, one considers the primordial power spectrum of the curvature perturbation, $\zeta(\mathbf{x})$, defined as [15, 16]

$$\zeta(\mathbf{x}) = -\Phi(\mathbf{x}) + \frac{aH}{\bar{\rho} + \bar{P}}\delta q(\mathbf{x}), \tag{1.17}$$

where Φ is the gravitational potential, δq is defined through the perturbed momentum density in the x^j direction, δT^0_j, as $\delta T^0_j \equiv -\partial \delta q / \partial x^j$ and $\bar{\rho}$ and $\bar{P}$ denote the background energy density and pressure, respectively.

For modes re-entering the horizon during the radiation-dominated epoch, by expanding the relation between $\delta(\mathbf{x})$ to first order in $\zeta(\mathbf{x})$, one finds their Fourier transforms are related as

$$\delta(\mathbf{k}) = \frac{4}{9}\left(\frac{k}{aH}\right)^2 \zeta(\mathbf{k}). \tag{1.18}$$

The dimensionless power spectrum of the density contrast is therefore related to the dimensionless power spectrum of ζ, $\mathcal{P}_\zeta(k,t)$, as

$$\mathcal{P}_\delta(k,t) = \frac{16}{81}\left(\frac{k}{aH}\right)^4 \mathcal{P}_\zeta(k,t). \tag{1.19}$$

Planck observations indicate that, on scales probed by the CMB ($k \sim 10^{-3} - 1\,\mathrm{Mpc}^{-1}$), the primordial power spectrum of curvature perturbations is well-parameterised as

$$\mathcal{P}_\zeta(k, t_\mathrm{i}) = A\left(\frac{k}{k_*}\right)^{n_\mathrm{s}-1}, \tag{1.20}$$

where A is the amplitude, k_* is the pivot scale and n_s is the scalar spectral index. Planck observations of CMB anisotropies find that, for $k_* = 0.05\,\mathrm{Mpc}^{-1}$, $A = 2.1 \times 10^{-9}$ and $n_\mathrm{s} = 0.965 \pm 0.004$ [4]. The fluctuations

are close to scale-invariant, with a slight 'red tilt', meaning that the power decreases with increasing k (i.e. at smaller physical length scales).

On cosmological scales observations of the CMB are consistent with the density perturbations being (largely) adiabatic, meaning that the perturbation in the number density of each component is equal. In principle there could also be an isocurvature component, in which a density perturbation in one component is compensated by perturbations of the opposite sign in one or more other components so the overall density perturbation is zero. The existence of isocurvature perturbations on cosmological scales is tightly constrained by CMB observations [17].

Spherical collapse

To describe the gravitational collapse of dark matter halos, we must go beyond linear theory since the resulting overdensities are too large, $\delta \gtrsim 1$. A simple non-linear model describing this process is the spherical collapse model [18].

In this model, one considers a spherical overdensity. The overdense region initially expands, before collapsing to form a virialised dark matter halo (i.e. a halo in which the virial theorem is satisfied, $2T + V = 0$, where T is the average kinetic energy and V is the average potential energy). One can calculate the time taken for collapse and the density of the resulting dark matter halo. In a flat matter-dominated Universe, the final dark matter halo has a density $\Delta \approx 178$ times the background matter density. Fitting functions for Δ exist for cosmologies with non-zero cosmological constant or curvature [19].

One can then compare the value of the overdensity obtained by extrapo-

lating linear theory to the time that the halo has collapsed. In a matter-dominated Universe, this value is $\delta_c \approx 1.69$, meaning that when the overdensity δ calculated using linear theory exceeds δ_c, a virialised dark matter halo forms. This value is largely cosmology-independent [20].

The smoothed density contrast

The mass, M, of a dark matter halo depends on its radius R, approximately as $M \sim \rho R^3$, where ρ is the density of the halo. To determine the abundance of halos of a given mass, it is therefore useful to smooth the density contrast on a length scale R, which removes the contributions from smaller scales. The smoothed density contrast is given by a convolution with a window function $W(\mathbf{x}; R)$,

$$\delta_R(\mathbf{x}, t) = \int \mathrm{d}^3\mathbf{x}' W(|\mathbf{x} - \mathbf{x}'|; R)\delta(\mathbf{x}', t). \tag{1.21}$$

The Fourier transform of the smoothed density contrast is then

$$\delta_R(\mathbf{k}, t) = \tilde{W}(k; R)\delta(\mathbf{k}, t), \tag{1.22}$$

where $\tilde{W}(k; R)$ is the Fourier transform of the real-space window function.

The variance of the smoothed density contrast, which gives the typical amplitude of fluctuations on a length scale R, is given by

$$\sigma^2(t; R) = \frac{1}{2\pi^2} \int \mathrm{d}k k^2 |\tilde{W}(k; R)|^2 P_\delta(k, t) \tag{1.23}$$

$$= \int \frac{\mathrm{d}k}{k} |\tilde{W}(k; R)|^2 \mathcal{P}_\delta(k, t). \tag{1.24}$$

On CMB scales, the primordial fluctuations in the density contrast have an amplitude $\sigma \sim \sqrt{\mathcal{P}_\delta(k = 1/R)} \sim 10^{-5}$ [17].

1.1.5 Inflation

As discussed in Sec. 1.1.3, the CMB temperature is essentially uniform across the sky and (as mentioned in Sec. 1.1.1) combining measurements from galaxy surveys and of CMB temperature anisotropies suggests the Universe is close to spatially flat. When considering the Big Bang model as described so far, these observations are challenging to explain, and present several problems.

- **Horizon problem:** The almost uniform temperature of the CMB suggests that baryonic matter and radiation throughout the observable Universe must have been in thermal equilibrium around the time of decoupling. Light can only have travelled a finite distance since the Big Bang and at recombination, the distance travelled corresponds to an angular size on the sky of $\approx 1^{\circ}$. It is therefore difficult to explain why patches of the sky which were apparently not in causal contact before decoupling have almost the same temperature.

- **Flatness problem:** It is possible to re-write the Friedmann equation (Eq. (1.12)) in terms of an effective energy density from spatial curvature, ρ_K, which depends on the scale factor as $\rho_K \propto a^{-2}$. This can also be expressed in terms of the density parameters as a deviation from spatial flatness, $\Omega_K = 1 - \Omega$, where Ω is the sum of the density parameters of all the components of the Universe and $\Omega = 1$ in a flat Universe. Since ρ_K dilutes away more slowly than the energy densities of matter or radiation, it must have had an unnaturally small value at early times in order to be compatible with observational constraints from the CMB and the baryon acoustic oscillation feature in the galaxy correlation function, which require $\Omega_K = 0.0007 \pm 0.0019$ [4].

- **Monopole problem:** In the 1980s, the most commonly-considered Grand Unified Theories (which describe the strong and electroweak forces as arising from a single gauge theory via symmetry breaking) predicted that heavy magnetic monopoles would be abundantly produced during symmetry-breaking phase transitions at high temperatures in the early Universe. The energy density of monopoles decreases as matter ($\rho \propto a^{-3}$). Before matter-radiation equality, the energy density of the background Universe decreases as $\rho \propto a^{-4}$, so monopoles would dominate the energy density of the Universe today. Not only is this not the case but no magnetic monopoles have been observed.

Inflation is a hypothesised period of accelerated expansion in the early Universe, that is a period when $\ddot{a} > 0$. Inflation can solve the problems outlined above in the following ways:

- **Horizon problem:** The rapid expansion of the Universe during inflation means that our entire observable Universe can arise from a single region that was in causal contact at early times.
- **Flatness problem:** The Universe's rapid expansion dilutes away any effective contribution from spatial curvature, which drives the Universe towards spatial flatness. The matter and radiation is generated after inflation ends.
- **Monopole problem:** A period of inflationary expansion causes the monopoles to be diluted so that their abundance is negligible today.

The condition for accelerated expansion can be written in terms of the equation of state parameter of the Universe, w, by combining the Friedmann

equation (Eq. (1.12)) and fluid equation (Eq. (1.3)), which gives

$$\frac{\ddot{a}}{a} = -\frac{4\pi G}{3}\rho(1+3w). \tag{1.25}$$

From Eq. (1.25), inflation occurs if the Universe is dominated by a component with equation of state parameter $w < -1/3$.

In most inflationary models, accelerated expansion is driven by a scalar field ϕ (known as the inflaton) with potential $V(\phi)$, which dominates the total energy density during inflation. Assuming the field is homogeneous and isotropic, its energy density and pressure are given by

$$\rho_\phi = \frac{1}{2}\dot{\phi}^2 + V(\phi), \tag{1.26}$$

$$P_\phi = \frac{1}{2}\dot{\phi}^2 - V(\phi), \tag{1.27}$$

and its evolution follows the Klein-Gordon equation

$$\ddot{\phi} + 3H\dot{\phi} + V'(\phi) = 0, \tag{1.28}$$

where $' \equiv \frac{\mathrm{d}}{\mathrm{d}\phi}$. From Eqs. (1.26) and (1.27), and requiring that the equation of state parameter of the scalar field $w < -1/3$ for accelerated expansion, inflation occurs in a scalar-field dominated Universe if $\dot{\phi}^2 < V(\phi)$. One can describe the dynamics of inflation by introducing the slow-roll parameters

$$\epsilon \equiv -\frac{\dot{H}}{H^2}, \tag{1.29}$$

$$\eta \equiv \frac{\dot{\epsilon}}{\epsilon H}. \tag{1.30}$$

The parameter ϵ describes the ratio of the kinetic energy to the potential energy of the inflaton. Accelerated expansion occurs when $\epsilon < 1$.

When the potential becomes steep enough that the inflaton gains enough

kinetic energy that $\dot{\phi}^2 > V(\phi)$ (or equivalently $\epsilon > 1$), the condition for accelerated expansion is no longer satisfied and inflation ends. The inflaton then decays into matter and radiation.

In addition to resolving the problems outlined above, inflation predicts the existence of primordial perturbations which arise from quantum fluctuations of the inflaton field. For a given inflationary model, one can predict the primordial power spectrum of curvature perturbations, $\mathcal{P}_\zeta(k, t_\mathrm{i})$. We now discuss how the primordial power spectrum predicted by slow-roll inflation can be related to the form inferred from CMB observations, and in Sec. 1.4.3 we consider inflation as a possible mechanism for producing primordial black holes.

Slow-roll inflation

The form of the primordial power spectrum inferred from CMB observations (Eq. (1.20)) can be obtained by considering inflation in the limit $\epsilon \ll 1$, $|\eta| \ll 1$, known as 'slow-roll' inflation. In this limit, one can relate the slow-roll parameters defined in Eq. (1.30) to the potential slow-roll parameters ϵ_V and η_V, as $\epsilon \approx \epsilon_V$ and $\eta \approx 4\epsilon_V - 2\eta_V$, where

$$\epsilon_V \equiv \frac{{M_\mathrm{Pl}}^2}{2}\left(\frac{V'}{V}\right)^2, \tag{1.31}$$

$$\eta_V \equiv {M_\mathrm{Pl}}^2 \frac{V''}{V}, \tag{1.32}$$

and $M_\mathrm{Pl} = 1/\sqrt{8\pi G} = 2.4 \times 10^{18}\,\mathrm{GeV}$ is the reduced Planck mass.

The power spectrum of primordial curvature perturbations can be written as

$$\mathcal{P}_\zeta(k) = \frac{1}{8\pi^2 {M_\mathrm{Pl}}^2}\frac{H^2}{\epsilon_V}, \tag{1.33}$$

where H and ϵ_V should be evaluated when a mode with comoving wavenumber k leaves the comoving Hubble radius $1/(aH)$, i.e. at $k = aH$. In slow-roll inflation, the probability distribution of the curvature perturbation ζ can be very well-approximated as gaussian (consistent with CMB observations [21]), in which case the power spectrum (Eq. (1.33)) completely characterises its statistics. Using the definitions of the potential slow-roll parameters, the slope of the primordial power spectrum from slow-roll inflation can be written as $n_\mathrm{s} - 1 = -6\epsilon_V + 2\eta_V$.

1.2 Dark Matter

The current concordance model of cosmology, the ΛCDM model, postulates that most of the matter in the Universe is non-baryonic and consists of 'cold' (i.e. non-relativistic well before matter-radiation equality [22]) dark matter (CDM). In order to be consistent with observations, a viable dark matter candidate must be stable, collisionless, and cannot have strong non-gravitational interactions with itself or other particle species. We outline the evidence for dark matter in Sec. 1.2.1, which comes from galactic rotation curves, the velocity dispersions in galaxy clusters and their temperatures, gravitational lensing, the CMB and large-scale structure. All the evidence for dark matter comes from its gravitational effects and therefore our understanding of gravity. Modifications to gravity offer an alternative explanation for the observed forms of galactic rotation curves [23, 24]. However, successfully reproducing CMB and large scale structure observations in this framework has proven challenging [25–27] (though see Ref. [28]). In this thesis we follow the standard interpretation that these observations provide evidence for dark matter. We discuss the distribution of dark matter in Sec. 1.2.2. We briefly discuss particle dark matter candidates

(WIMPs and axions) in Sec. 1.3 before introducing primordial black holes (PBHs) Sec. 1.4.

1.2.1 Evidence for dark matter

Galaxies

Galaxy rotation curves describe how the orbital, or circular, speeds of stars and gas in a spiral galaxy, $v_{\rm c}(R)$, depend on their distance from the galactic centre R. The dependence of $v_{\rm c}$ on R can be measured using the Doppler shift of absorption and emission lines from stars and gas.

For a spherically symmetric matter distribution, the rotational speed depends on R as

$$v_{\rm c}(R) = \sqrt{\frac{GM(<R)}{R}}, \tag{1.34}$$

where $M(<R)$ is the total mass enclosed within a radius R. Therefore, if one only considers the visible mass, the rotation curve would be expected to decrease as $v_{\rm c}(R) \propto R^{-1/2}$ at radii significantly larger than where the visible mass is concentrated.

Rubin & Ford [29] studied the rotation curve M31 and found that it is flattened at large radii. Observations of other galaxies showed a similar flattening of the rotation curve at large radii [30–33]. The simplest explanation for these observations is that there is some source of invisible mass in a halo that extends to significantly larger radii than the visible matter, and which significantly outweighs the visible matter.

Galaxy clusters

Galaxy clusters, which are the largest gravitationally bound structures in the Universe, provide several sources of evidence for the existence of dark matter. Observations indicating the need for dark matter began with Zwicky [34], who in 1933 noted the large velocity dispersion of galaxies within the Coma Cluster. He found that the mass of visible matter in the Coma cluster was insufficient to explain the observed velocity dispersion of galaxies, indicating the need for a source of non-visible mass.

X-ray observations provide additional evidence that galaxy clusters contain a large amount of non-baryonic dark matter. The intracluster medium consists of hot gas, which produces X-rays through bremsstrahlung and line emission. The X-ray spectrum can be used to calculate the dependence of the gas temperature and density with radius (from the cluster centre), which can be used to determine the cluster mass (see Refs. [35, 36] for reviews of the determination of galaxy cluster masses from X-ray observations). The observed gas temperature is too high to be explained when including only the visible mass in galaxy clusters.

Observations of merging galaxy clusters provide some of the most striking evidence for dark matter. During a cluster merger, galaxies (which behave as collisionless particles) essentially pass through one another, while the hot X-ray emitting gas experiences pressure and lags behind. The distribution of mass can be mapped by measuring the distortion of images of background galaxies caused by the gravitational deflection of light. Since the gas (rather than galaxies) makes up most of the baryonic mass of the clusters, in the absence of a substantial dark matter component, one would expect the total matter distribution to approximately follow the distribution of gas. Observations of the Bullet Cluster [37, 38] and other merging

galaxy clusters [39–41] show that the total mass distribution follows the distribution of the galaxies. This indicates that most of the mass of the clusters is made up of an invisible matter component that is essentially collisionless (requiring it to have weak non-gravitational interactions with itself or baryonic matter).

Cosmic microwave background

Anisotropies in the CMB temperature provide the most precise measurements of the abundance of dark matter. These anisotropies can be analysed statistically by measuring the correlation between the temperature fluctuations in different regions as a function of their angular separation, to obtain the angular power spectrum.

Prior to recombination and decoupling, photons and baryons were tightly coupled, forming a 'photon-baryon fluid'. Peaks in the angular power spectrum arise as a result of oscillations in this medium. Since dark matter has very weak (if any) non-gravitational interactions with itself or other particle species, after matter-radiation equality overdensities in the dark matter distribution could grow and formed gravitational wells. In the gravitational wells produced by the dark matter, the photon-baryon fluid was compressed by gravity, until radiation pressure became sufficient to resist further collapse, producing a spherical sound wave that expanded outwards. The peaks in the CMB angular power spectrum correspond to different numbers of compressions and rarefactions. The first (highest) peak corresponds to a region of plasma that had compressed once prior to decoupling, the second peak to a region of plasma that underwent one compression and one rarefaction, and so on.

The fraction of the Universe's density in baryons, Ω_{b}, affects the relative

heights of odd and even peaks, while the total matter density $\Omega_{\rm m}$ determines the overall heights of the peaks. Planck observations of CMB anisotropies find [4]

$$\Omega_{\rm m} \approx 0.31, \quad \Omega_{\rm b} \approx 0.05. \tag{1.35}$$

This value of $\Omega_{\rm b}$ is consistent with the value measured independently from the abundance of light elements (see Sec. 1.1.2), and is substantially smaller than $\Omega_{\rm m}$, indicating the need for a dark matter component making up most of the Universe's non-relativistic matter.

Large-scale structure

The existence of structures such as galaxies in the Universe today provides indirect evidence for the existence of dark matter. Baryons are tightly coupled to photons before decoupling. Therefore overdensities in the baryon density can only grow after decoupling. At decoupling, the baryon density fluctuations are proportional to the temperature fluctuations in the CMB, which are observed to be of order $\Delta T/T \sim 10^{-5}$. Without dark matter, the subsequent growth of baryonic density fluctuations would not be sufficient to form non-linear structures such as galaxies by the present day. Viewed another way, for baryons alone to form galaxies by today would require larger baryonic density fluctuations at decoupling and therefore larger temperature fluctuations in the CMB (of order $\Delta T/T \sim 10^{-4}$) than observed. On sub-horizon scales, dark matter density fluctuations grow linearly with the scale factor from matter-radiation equality onwards. This growth is sufficient to allow for a more rapid collapse of the baryonic density fluctuations after decoupling and the formation of galaxies [42].

The matter density parameter has been constrained by Dark Energy Spectroscopic Instrument (DESI) using measurements of the baryon acous-

tic oscillation (BAO) feature in the distribution of galaxies, quasars and the Lyman-α forest to give $\Omega_{\rm m} = 0.295 \pm 0.015$ [5]. Including CMB anisotropy measurements from Planck [4] and CMB lensing data from Planck [43] and the Atacama Cosmology Telescope (ACT) [44–46] leads to $\Omega_{\rm m} = 0.307 \pm 0.005$ [5].

1.2.2 The distribution of dark matter

Density profile and velocity distribution

The density profile describes the dark matter density at a distance R from the centre of the halo, $\rho(R)$. A simple but commonly considered density profile is that corresponding to an isothermal sphere, $\rho(R) \propto R^{-2}$ (where R is the distance from the halo centre). For this density profile, the mass enclosed within a radius R behaves as $M(< R) \propto R$ and from Eq. (1.34) the rotation curve $v_{\rm c}(R)$ is flat.

A variation of the isothermal sphere is the cored isothermal sphere, for which the density profile is

$$\rho(R) = \rho_0 \frac{R_{\rm c}^2 + R_0^2}{R_{\rm c}^2 + R^2}, \tag{1.36}$$

where ρ_0 is the local dark matter density, $R_{\rm c}$ is the core radius and R_0 is the distance of the Sun from the halo centre.

Halos from DM-only numerical simulations are often well-described by the Navarro-Frenk-White (NFW) density profile [47]

$$\rho(R) = \frac{\rho_0}{(R/R_{\rm s})\left[1 + (R/R_{\rm s})\right]^2}, \tag{1.37}$$

where the scale radius, $R_{\rm s}$, is defined as the radius at which the logarithmic derivative of $\rho(R)$ with respect to R, $\mathrm{d}\ln\rho/\mathrm{d}\ln R$, equals -2.

For a given density profile, the velocity distribution, $f(v)$, can be be determined by solving the collisionless Boltzmann equation. For an isothermal sphere, this gives a Maxwellian distribution [48],

$$f(v) = \frac{1}{\pi^{3/2} v_{\rm c}^3} \exp\left(-\frac{v^2}{v_{\rm c}^2}\right), \tag{1.38}$$

where $v_{\rm c}$ is the circular speed.

Local dark matter density and circular speed

The local dark matter density, ρ_0, can be determined by either local or global measurements. Local measurements use the motions of nearby stars to estimate the gravitational potential close to the Sun and thereby infer the local dark matter density. Global measurements involve fitting the observed velocities or spatial distributions of tracers (such as stars and gas) to a mass model of the Milky Way. From this model one can obtain the local circular speed, $v_{\rm c}(R_0)$, and therefore ρ_0, using a measured value of the galactocentric distance of the Sun, R_0. The values obtained generally lie in the range $\rho_0 = (0.3 - 0.6)\,\mathrm{GeV/cm^3}$ (see e.g. Table 4 of Ref. [49] and Ref. [50]).

Traditionally, the local circular speed has been taken to be $v_{\rm c}(R_0) = 220\,\mathrm{km\,s^{-1}}$ [51]. More recent measurements [52, 53] have obtained larger values. Ref. [52] found $v_{\rm c}(R_0) = 240 \pm 8\,\mathrm{km\,s^{-1}}$ using masers in star-forming regions across the Milky Way, while Ref. [53] found $v_{\rm c}(R_0) = 229.0 \pm 0.2\,\mathrm{km\,s^{-1}}$ using a Jeans analysis with red giant stars used as tracers.

Dark matter substructure

In a Universe with most of its matter made up of cold dark matter, the growth of structure is hierarchical: small halos of dark matter form at earlier times, and larger structures are formed from the mergers of smaller structures. In this process, the dense inner regions of merging halos can survive, so the resulting dark matter halos can contain a large amount of substructure. Dark matter-only numerical simulations find $\approx 10\%$ of the halo mass is in substructures sufficiently large to be resolved by the simulation [54]. This fraction is smaller in simulations which model the effects of baryonic matter [55].

1.3 Particle Dark Matter Candidates

Aside from PBHs, most DM candidates are a species of new fundamental particle. Two of the most commonly-considered particle dark matter candidates are weakly interacting massive particles (WIMPs) and axions, which we briefly discuss in the following section. See Refs. [42, 56–59] for reviews on particle dark matter.

1.3.1 Weakly Interacting Massive Particles (WIMPs)

If there exists a particle with a weak-scale self-annihilation cross-section, its relic density from thermal freeze-out matches that required to make up the dark matter [60]. Such particles, termed weakly interacting massive particles (WIMPs), have a sufficiently small interaction strength to be a viable dark matter candidate. WIMPs naturally arise from resolutions of the gauge hierarchy problem such as supersymmetry (see e.g. Ref. [61]). Su-

persymmetry introduces a new supersymmetric partner for each Standard Model particle species, such that Standard Model bosons have fermionic partner particles and vice versa. To prevent proton decay one can introduce R-parity conservation, where Standard Model particles have R-parity 1 and their supersymmetric partners have R-parity -1 [62]. As a consequence, the lightest supersymmetric particle is stable, making it a viable dark matter candidate.

Direct detection experiments search for WIMP scattering off nuclei. These require highly-sensitive, tonne-scale detectors located deep underground. At present, leading bounds are from liquid noble gas detectors such as LUX-ZEPLIN [63], PandaX-4T [64] and XENONnT [65]. Indirect detection approaches search for Standard Model products produced by WIMP annihilations, such as gamma rays from dwarf galaxies [66] or the Galactic Centre [67] and neutrinos from the Sun [68, 69].

1.3.2 Axions

Axions were first proposed in the context of the strong CP problem. The Standard Model predicts CP violation in the strong interaction, which would manifest as a non-vanishing neutron electric dipole moment. Experimental measurements constrain its value to be extremely small [70], requiring a cancellation between two seemingly unrelated terms that contribute to CP violation. The solution proposed by Peccei & Quinn [71, 72] introduces a new pseudoscalar boson (the QCD axion) [73, 74] which is a viable dark matter candidate. In addition, string theory generically predicts the existence of a large number of axion-like particles (ALPs) which may also be viable dark matter candidates [75]. We refer to QCD axions and ALPs collectively as 'axions' (see Ref. [59] for a review).

Axion coupling to photons allows them to interconvert with photons in the presence of a strong magnetic field. This coupling underlies searches using haloscopes such as ADMX [76], helioscopes such as CAST [77] and light shining through walls experiments like ALPS [78] and OSQAR [79]. Astrophysical and cosmological observations place additional constraints on the axion coupling to photons and other Standard Model particles. See Ref. [80] for a comprehensive repository of constraints on axions and Ref. [81] for a recent review of the effects of axions on astrophysical observations.

1.4 Primordial Black Holes

Primordial black holes (PBHs) may have formed from the collapse of large density perturbations in the early Universe [82, 83]. PBHs evaporate via Hawking radiation [84, 85], however PBHs with initial mass $M_{\mathrm{PBH,i}} \gtrsim 10^{15}\,\mathrm{g}$ have a lifetime longer than the age of the Universe [86, 87]. PBHs are cold and non-baryonic, and are therefore a viable dark matter candidate.

Throughout the rest of this thesis we consider the most commonly considered scenario for PBH formation: the collapse of large fluctuations (generated during inflation) in the radiation-dominated epoch [3]. In Sec. 1.4.1, we present approximate calculations for the conditions required to form PBHs, their resulting mass, and the PBH abundance. In Sec. 1.4.2 we discuss the limitations of these calculations and outline more realistic approaches. We briefly overview inflationary models for producing PBHs in Sec. 1.4.3 before discussing PBH clustering in Sec. 1.4.4. In Sec. 1.4.5, we review observational constraints on PBHs.

[3] Other proposed formation mechanisms include the collapse of cosmic string loops [88, 89] and collisions between bubbles generated during a first-order phase transition [90–92].

1.4.1 A simple model for PBH formation

In the following, we present a simplified picture of PBH formation and the requirements for PBHs to make up a significant fraction of the dark matter today.

Threshold in the density contrast

In the following, we present an approximate calculation which provides an order of magnitude estimate for the threshold overdensity required to form a PBH. We discuss more accurate results from numerical simulations in Sec. 1.4.2.

A PBH will form if a sufficiently overdense region overcomes the pressure forces resisting its collapse and the region contracts to within its Schwarzschild radius. Following Ref. [93] (see also Ref. [94], which this calculation largely follows), we consider a spherically symmetric overdense region with an initial radius, $R_{\rm i}$, larger than the Hubble radius, $R_{\rm H} \equiv 1/H$, in a spatially flat background. The overdense region evolves according to the Friedmann equation (Eq. (1.12)) for a spatially-closed Universe with positive curvature,

$$\tilde{H}^2 \equiv \left(\frac{1}{\tilde{a}}\frac{\mathrm{d}\tilde{a}}{\mathrm{d}\tilde{t}}\right)^2 = \frac{8\pi G}{3}\tilde{\rho} - \frac{\tilde{K}}{\tilde{a}^2}, \tag{1.39}$$

where the tilde denotes quantities in the overdense region. One can choose the coordinates such that both the background and the overdense region have the same expansion rate at some initial time $t = \tilde{t} = t_{\rm i}$ and the same initial scale factor $a(t_{\rm i}) = \tilde{a}(t_{\rm i})$. The initial density contrast, $\delta_{\rm i}$, can then

be expressed as

$$\delta_{\rm i} \equiv \frac{\tilde{\rho}(t_{\rm i}) - \rho(t_{\rm i})}{\rho(t_{\rm i})} = \frac{\tilde{K}}{\left(H(t_{\rm i})a(t_{\rm i})\right)^2}. \tag{1.40}$$

After some time, the overdense region will stop expanding. Its radius at this time (which can be found by setting $\tilde{H} = 0$ in Eq. (1.39)) is

$$R_{\rm c} = \sqrt{\frac{1+\delta_{\rm i}}{\delta_{\rm i}}} R_{\rm i} \approx {\delta_{\rm i}}^{-1/2} R_{\rm i}. \tag{1.41}$$

In order for the region to continue contracting its radius must exceed the Jeans radius, $R_{\rm c} > R_{\rm J} \simeq c_{\rm s} t_{\rm c}$, where $c_{\rm s}$ is the sound speed ($c_{\rm s} = 1/\sqrt{3}$ in a radiation-dominated Universe) and $t_{\rm c} \sim 2t_{\rm i}/\delta_{\rm i}$ is the time at which the overdense region stops expanding [95]. From Eq. (1.41), the condition for collapse can be written as

$$c_{\rm s} \lesssim \frac{1}{2}\frac{R_{\rm i}}{t_{\rm i}} {\delta_{\rm i}}^{1/2}. \tag{1.42}$$

Since the right-hand side of this inequality is independent of time one can evaluate it at horizon crossing ($R_{\rm i} = 1/H_{\rm i} = 2t_{\rm i}$), which gives

$$\delta_{\rm i} \geq \delta_{\rm c} \approx c_{\rm s}^2, \tag{1.43}$$

with $\delta_{\rm c} \approx 1/3$ in a radiation-dominated Universe.

The overdensity at the point of collapse is $\delta(t_{\rm c}) = (\pi/2)^4 - 1$ [95]. The Schwarzschild radius, $R_{\rm S}$, of the overdense region is then

$$R_{\rm S} = 2GM = \frac{8\pi G}{3}\tilde{\rho} R_{\rm c}^3 = \frac{\pi^4}{16} H^2 R_{\rm c}^3 = \frac{\pi^4}{64}\frac{R_{\rm c}^3}{t_{\rm c}^2} \sim c_{\rm s}^2 R_{\rm c}, \tag{1.44}$$

where $M = (4\pi/3)\tilde{\rho} R_{\rm c}^3$ is the mass within the overdense region and we have used $H = 1/(2t)$ during the radiation-dominated epoch and $R_{\rm c} \sim c_{\rm s} t_{\rm c}$. From the time-evolution of the radius of the collapsing region [95], a black

hole will form within one e-folding after the start of collapse.

PBH mass

The Jeans mass of the overdense region at the moment it stops expanding, $M_{\rm J}$, is given by $M_{\rm J} \approx c_{\rm s}^3 M_{\rm H}$, where the horizon mass, $M_{\rm H}$, is the total mass enclosed within the Hubble radius, $R_{\rm H} \equiv 1/H$,

$$M_{\rm H} = \frac{4\pi}{3} R_{\rm H}^3 \rho = \frac{1}{2GH}. \tag{1.45}$$

In Eq. (1.45), we have assumed a flat Universe ($\rho = \rho_{\rm crit}$) and used Eq. (1.9) for $\rho_{\rm crit}$. Therefore, the mass of the resulting black hole, $M_{\rm PBH}$, is of the order of the horizon mass, $M_{\rm PBH} \approx \alpha M_{\rm H}$, where $\alpha = {c_{\rm s}}^3 \approx 0.2$ during the radiation-dominated epoch [96]. Using Eq. (1.45) for the horizon mass, the initial PBH mass can be approximately related to the formation time as

$$M_{\rm PBH,\,i} \sim 10^{15} \alpha \left(\frac{t_{\rm i}}{10^{-23}{\rm s}} \right) \ {\rm g}. \tag{1.46}$$

Relation between initial and present abundance of PBHs

We now consider how the fraction of the Universe's energy density that collapses into PBHs at the PBH formation time, β, is related to $M_{\rm PBH}$ and the present-day PBH density parameter $\Omega_{\rm PBH}$. The energy density of PBHs behaves as non-relativistic matter, $\rho_{\rm PBH} \propto a^{-3}$. During the radiation-dominated era, the background density decreases as $\rho \propto a^{-4}$, so the PBH density relative to the background density increases proportional to a. Therefore, β is small even if PBHs make up all of the dark matter today.

In the following (standard) calculation, unless specified otherwise, a sub-

script 0 denotes a quantity evaluated at the present time and quantities with no subscript are evaluated at the PBH formation time. The definition of β gives

$$\beta \equiv \frac{\rho_{\rm PBH}}{\rho} = \frac{\rho_{\rm PBH,0}}{\rho}\left(\frac{a_0}{a}\right)^3 \tag{1.47}$$

$$= \Omega_{\rm PBH}\left(\frac{H_0}{H}\right)^2\left(\frac{a_0}{a}\right)^3, \tag{1.48}$$

where $\Omega_{\rm PBH}$ is the (present-day) density parameter of PBHs and in the final equality we have used the Friedmann Equation (Eq. (1.12)) and the definition of the density parameter (Eq. (1.10)).

We consider PBHs formed during the radiation-dominated era, during which the Friedmann equation (Eq. (1.12)) can be written

$$H^2 = \frac{8\pi G}{3}\frac{\rho_{\rm r}}{\rho_{\rm r,0}}\rho_{\rm r,0} = \frac{\rho_{\rm r}}{\rho_{\rm r,0}}\Omega_{\rm r}H_0^2. \tag{1.49}$$

The energy density of radiation $\rho_{\rm r} \propto g_*(T)T^4$, where $g_*(T)$ is the number of relativistic degrees of freedom at temperature T, so the energy density in radiation at the PBH formation time and the present are related as

$$\frac{\rho_{\rm r}}{\rho_{\rm r,0}} = \frac{g_*}{g_{*,0}}\left(\frac{T}{T_0}\right)^4. \tag{1.50}$$

The ratio of temperatures can be calculated using the conservation of entropy. The entropy density $s \propto g_{*,s}(T)T^3$, where $g_{*,s}$ is the effective number of entropy degrees of freedom. Conservation of the total entropy, $S \propto sa^3$, implies

$$T_0^3 g_{*,s}(T_0)a_0^3 = T^3 g_{*,s}(T)a^3. \tag{1.51}$$

In this thesis, we focus on PBHs of mass $M_{\rm PBH} \lesssim 10^4 M_\odot$, which form before electron-positron annihilation, so $g_* = g_{*,s}$ at the PBH formation

time. Using Eqs. (1.51) and (1.50), Eq. (1.49) can therefore be written as

$$H^2 = \left(\frac{g_*}{g_{*,0}}\right)^{-1/3} \left(\frac{g_{*,s}(T_0)}{g_{*,0}}\right)^{4/3} \left(\frac{a_0}{a}\right)^4 \Omega_\mathrm{r} H_0^2. \tag{1.52}$$

Substituting Eq. (1.52) into Eq. (1.48) and re-arranging for Ω_PBH gives

$$\Omega_\mathrm{PBH} = \left(\frac{g_*}{g_{*,0}}\right)^{-1/3} \left(\frac{g_{*,s}(T_0)}{g_{*,0}}\right)^{4/3} \left(\frac{a_0}{a}\right) \Omega_\mathrm{r} \beta. \tag{1.53}$$

Assuming all PBHs form at the same time and neglecting critical collapse (see Sec. 1.4.2), all PBHs have the same initial mass $M_{\mathrm{PBH,\,i}}$. For the initial mass, $M_{\mathrm{PBH,\,i}} \approx \alpha M_\mathrm{H}$ is used with $M_\mathrm{H} = 1/(2GH)$ (see Eq. (1.45)). Additionally, it is assumed that the the present-day PBH mass, M_PBH, is the same as its initial mass, $M_{\mathrm{PBH,\,i}}$. This is a reasonable assumption for PBHs of initial mass $10^{15}\,\mathrm{g} \lesssim M_{\mathrm{PBH,\,i}} \lesssim 10 M_\odot$. PBHs of initial mass $M_{\mathrm{PBH,\,i}} \lesssim 10^{15}\,\mathrm{g}$ lose a significant ($\gtrsim 10\%$) fraction of their mass over time via Hawking radiation. Accretion onto PBHs of initial mass $M_{\mathrm{PBH,\,i}} \gtrsim 10 M_\odot$ may cause their masses to grow by an order of magnitude or more, though there are significant uncertainties in modelling PBH accretion [97]. The effects of critical collapse and mass loss via Hawking evaporation are relevant to the mass function of asteroid-mass PBHs and are considered in more detail in Chapter 3. During the radiation-dominated epoch, M_PBH can therefore be written as (using Eq. (1.52) for H)

$$M_\mathrm{PBH} = \frac{\alpha}{2G} \left(\frac{g_*}{g_{*,0}}\right)^{1/6} \left(\frac{g_{*,s}(T_0)}{g_{*,0}}\right)^{-2/3} \left(\frac{a}{a_0}\right)^2 \frac{1}{(\Omega_\mathrm{r} H_0^2)^{1/2}}. \tag{1.54}$$

Re-arranging Eq. (1.54) for a_0/a and substituting into Eq. (1.53) gives

$$\Omega_\mathrm{PBH} = 4.5 \times 10^7 \left(\frac{g_*}{106.75}\right)^{1/4} \left(\frac{\alpha}{0.2}\right)^{1/2} \left(\frac{M_\mathrm{PBH}}{M_\odot}\right)^{-1/2} \beta, \tag{1.55}$$

where we have used $g_{*,0} = 3.38$, $g_{*,\mathrm{s}}(T_0) = 3.94$, $\Omega_\mathrm{r} = 9.2 \times 10^{-5}$ and

$H_0 = 67.4\,\mathrm{km\,s^{-1}\,Mpc^{-1}}$ [4].

Constraints on the abundance of PBHs are typically given in terms of the fraction of dark matter in PBHs, $f_{\rm PBH} \equiv \Omega_{\rm PBH}/\Omega_{\rm DM}$. Using $\Omega_{\rm DM} = 0.26$ [4], from Eq. (1.55),

$$f_{\rm PBH} = 1.7 \times 10^8 \left(\frac{g_*}{106.75}\right)^{1/4} \left(\frac{\alpha}{0.2}\right)^{1/2} \left(\frac{M_{\rm PBH}}{M_\odot}\right)^{-1/2} \beta. \tag{1.56}$$

A simple model for the initial PBH abundance

In the simplest calculation of the PBH abundance, using Press-Schechter theory [98], β is given by the fraction of regions of the Universe sufficiently dense to form PBHs, multiplied by the ratio of the PBH mass to the horizon mass,

$$\beta = 2\int_{\delta_{\rm c}}^{\infty} \frac{M_{\rm PBH}}{M_{\rm H}} P(\delta)\mathrm{d}\delta = 2\alpha \int_{\delta_{\rm c}}^{\infty} P(\delta)\mathrm{d}\delta, \tag{1.57}$$

where $P(\delta)$ is the probability distribution of the density contrast. The standard factor of 2 accounts for regions that are below the threshold but which are subsumed in larger regions that are sufficiently overdense to collapse. Assuming $P(\delta)$ is gaussian with variance σ^2, the PBH abundance is

$$\beta = \alpha \mathrm{erfc}\left(\frac{\delta_{\rm c}}{\sqrt{2}\sigma}\right) \simeq \frac{2\alpha\sigma}{\sqrt{2\pi}\delta_{\rm c}} \exp\left(-\frac{\delta_{\rm c}^2}{2\sigma^2}\right), \tag{1.58}$$

where for the second approximate equality we have assumed $\delta_{\rm c} \gg \sigma$, which is reasonable for values of σ that satisfy observational constraints on β. From Eq. (1.58), we can see that the PBH abundance is exponentially sensitive to the threshold overdensity, $\delta_{\rm c}$, and the width of the distribution, σ.

To roughly estimate the lower bound on σ required for PBHs to make up a significant fraction of the dark matter, we consider a population of PBHs

with initial mass $M_{\mathrm{PBH,i}} \sim 10^{15}$ g (roughly the initial mass of a PBH with a lifetime equal to the age of the Universe, see Sec. 1.4.5) making up all of the dark matter. Combining Eq. (1.56) with Eq. (1.58), and assuming that a PBH can form if the density contrast exceeds a threshold value $\delta_{\mathrm{c}} \sim 1/3$, gives a minimum value of $\sigma \sim 0.04$, which is orders of magnitude larger than the value on CMB scales ($\sigma \sim 10^{-5}$) [17].

If the primordial power spectrum were exactly scale-invariant, $\mathcal{P}_\zeta = A$ with $A = 2.1 \times 10^{-9}$ given by its value on CMB scales, no PBHs would be produced. Using Eq. (1.24) with $\mathcal{P}_\delta$ calculated using Eqs. (1.19) and (1.20) gives $\sigma \sim 10^{-5}$, so the resulting PBH abundance is negligible,

$$\beta \approx \alpha \mathrm{erfc}\left(\frac{1/3}{\sqrt{2} \times 10^{-5}}\right) \sim 0.2 \times \mathrm{erfc}(10^4) \sim 10^{-6} \exp\left(-10^9\right). \quad (1.59)$$

In order to produce a sufficient number of PBHs for them to make up a significant fraction of the dark matter, the primordial power spectrum $\mathcal{P}_\zeta$ has to be increased by approximately seven orders of magnitude compared to its value on cosmological scales [99].

1.4.2 Improvements to PBH formation and abundance calculations

PBH formation threshold

Numerical simulations show that δ_{c} depends on the shape of the energy density profile in the overdense region [100, 101], where the average profile is determined by the shape of the primordial power spectrum [102]. Ref. [101] finds a range $0.4 \lesssim \delta_{\mathrm{c}} \leq 2/3$ for PBHs formed during the radiation-dominated epoch. The value of δ_{c} is reduced during phase tran-

sitions [103–108] and periods of particle annihilation [108, 109] due to the temporary reduction in the equation of state parameter, leading to significantly increased PBH production.

Ref. [110] showed that the threshold for PBH formation from an initial spherically symmetric perturbation is universal (i.e. independent of the shape of the energy density profile) when given in terms of the compaction function C [111], which is defined as twice the mass excess δM in a sphere of radius R centred at $\mathbf{x}$ [4],

$$C(\mathbf{x}, R) = 2\frac{\delta M}{R}. \tag{1.60}$$

The criterion for PBH formation can be expressed as the requirement that the averaged value of the compaction within a sphere of radius $r_{\rm m}$ exceeds a threshold value $C_{\rm c}$, where $r_{\rm m}$ is the radius at which C is maximised [110].

Non-gaussianity

Since PBHs are formed from large density perturbations far into the tail of the distribution of δ (or the compaction C), the PBH abundance is sensitive to the exact form of the tail of the distribution. Therefore, deviation from a gaussian distribution can significantly affect the abundance of PBHs produced [112, 113].

Non-gaussianity in the tail of the distribution of ζ is expected from inflationary models that form PBHs (see Sec. 1.4.3). Furthermore, δ is related non-linearly to the curvature perturbation ζ. Therefore, even if the distribution of ζ is exactly gaussian, the distribution of δ will not be. For the large perturbations required to form PBHs, using the linear relation in

[4] The original definition in Ref. [111] differs by a factor of two.

Eq. (1.18) overpredicts the PBH abundance from a given primordial power spectrum by orders of magnitude [114–116].

Calculation method

The PBH abundance has also been calculated using excursion-set theory [117, 118], which is an improvement on Press-Schechter theory that addresses the 'cloud-in-cloud' problem. This problem describes the situation when a region of mass M_1 that is sufficiently overdense to form a PBH can be embedded in a region of mass $M_2 > M_1$ that is sufficiently overdense to collapse to form a PBH, but is counted as two separate objects. Excursion set theory addresses this problem by only considering the largest region that is sufficiently overdense to collapse. Another approach is peaks theory [119–121], which considers PBH formation to occur when the maximum value of a fluctuation exceeds a threshold, rather than the average value.

Extended mass functions

Due to near critical gravitational collapse [122], the mass of a PBH depends on the amplitude, δ, of the perturbation from which it forms as well as the horizon mass, $M_{\rm H}$: $M_{\rm PBH,i} = kM_{\rm H}(\delta - \delta_{\rm c})^{\gamma}$, where k and $\gamma \simeq 0.36$ are constants [123] [5]. PBHs will therefore have an extended mass function even if they all form at the same time, i.e. from a delta-function peak in the primordial power spectrum [123–125]. In reality the primordial power spectrum will have finite width, and PBHs will form on a range of scales. For various inflation models (see Sec. 1.4.3) the mass functions calculated,

[5] The dependence of the PBH mass on the compaction function has the same power law scaling.

taking critical collapse into account, can be roughly approximated by a log-normal distribution [126, 127]. Gow et al. [128] found that other functional forms provide a better fit to the tails of the (numerically-calculated) PBH mass functions calculated using the method from Ref. [129].

1.4.3 PBH formation from inflation

We now overview concrete inflationary models that can produce sufficiently large fluctuations to form PBHs. Viable inflation models must produce the correct form of the primordial power spectrum on cosmological scales, while greatly enhancing it on smaller scales. See Ref. [130] for a recent review of single-field and multi-field inflation models that may be able to produce PBHs.

Single-field models

To achieve sufficient growth to form PBHs in single-field inflation models requires violation of the slow-roll approximation [131]. Most often, one considers a phase of 'ultra slow-roll' (USR) inflation [132, 133], in which $|V'(\phi)| \ll |\ddot{\phi}|, |3H\dot{\phi}|$. In this limit, the first slow-roll parameter is small and rapidly decreasing, $\epsilon \propto a^{-6}$, while the second slow-roll parameter is large and negative, $\eta = -6$.

The effect of quantum diffusion, in which the quantum fluctuations of a field are larger than its classical displacement, can be significant. When quantum diffusion dominates the dynamics of the inflaton, the tail of the probability distribution of ζ changes from gaussian (as in the slow-roll case) to exponential [134, 135].

Recently, there has been an ongoing debate as to whether it is possible to form PBHs in single-field inflation models without producing quantum corrections which would cause perturbations on CMB scales to deviate from their observed form (see e.g. Refs. [136–141]).

Multi-field models

An alternative scenario is that PBHs could be formed from inflation driven by multiple fields. An example of a multi-field inflationary model with the potential to produce PBHs is hybrid inflation with a mild waterfall transition.

Hybrid inflation [142, 143] is a two-field inflationary model, with an inflaton ϕ and an auxiliary field ψ. Initially, ψ is fixed and ϕ undergoes slow-roll in a valley. Once the inflaton reaches a critical value $\phi = \phi_{\rm c}$, the auxiliary field falls into the true minimum of its potential (this is known as a 'waterfall transition').

The duration of the waterfall transition determines whether the predictions of hybrid inflation are consistent with CMB observations (whilst simultaneously providing a mechanism to produce PBHs). If the transition is too fast the primordial power spectrum of curvature perturbations on CMB scales has a blue tilt (i.e. the power spectrum is larger for larger k), which is strongly ruled out by observations. If the transition is too slow then, for values of the spectral index $n_{\rm s}$ consistent with CMB observations, the power spectrum amplitude is much larger than the observed value [144]. Ref. [145] considered the intermediate case with a mild waterfall transition. In this scenario, fluctuations on CMB scales exit the horizon while the inflaton is slowly rolling in the valley. The change in the form of the potential after the critical point leads to a tachyonic instability, generating

large fluctuations. In this case the primordial power spectrum can satisfy observational constraints on CMB scales whilst having a large peak at smaller scales [145, 146].

1.4.4 PBH clustering

Clustering of PBHs can affect observational constraints. For gaussian density fluctuations, the regions sufficiently overdense to form PBHs are randomly distributed in space, inevitably producing Poisson fluctuations in the PBH distribution [118, 147, 148]. These give rise to an isocurvature component in the PBH density field, leading to the formation of PBH clusters shortly after matter-radiation equality [149, 150]. If the density contrast is non-gaussian, the initial clustering of PBHs may be enhanced, resulting in more compact PBH clusters than in the case with no initial clustering [151–153].

1.4.5 Observational constraints

The abundance of PBHs is constrained by observations which probe a wide range of masses (see Refs. [154–157] for recent reviews). These constraints exclude PBHs from making all of the dark matter unless their mass lies in the range $10^{17}\,\mathrm{g} \lesssim M_{\mathrm{PBH}} \lesssim 10^{22}\,\mathrm{g}$, often referred to as the 'asteroid-mass window'. In this section, we briefly review the main sources of observational constraints on PBHs.

Fig. 1.1 shows the constraints on f_{PBH} (assuming all PBHs have the same mass), produced using the PBHbounds code available from https://github.com/bradkav/PBHbounds [154, 158]. We have changed the default constraints in PBHbounds (as of September 2024) to show the evaporation

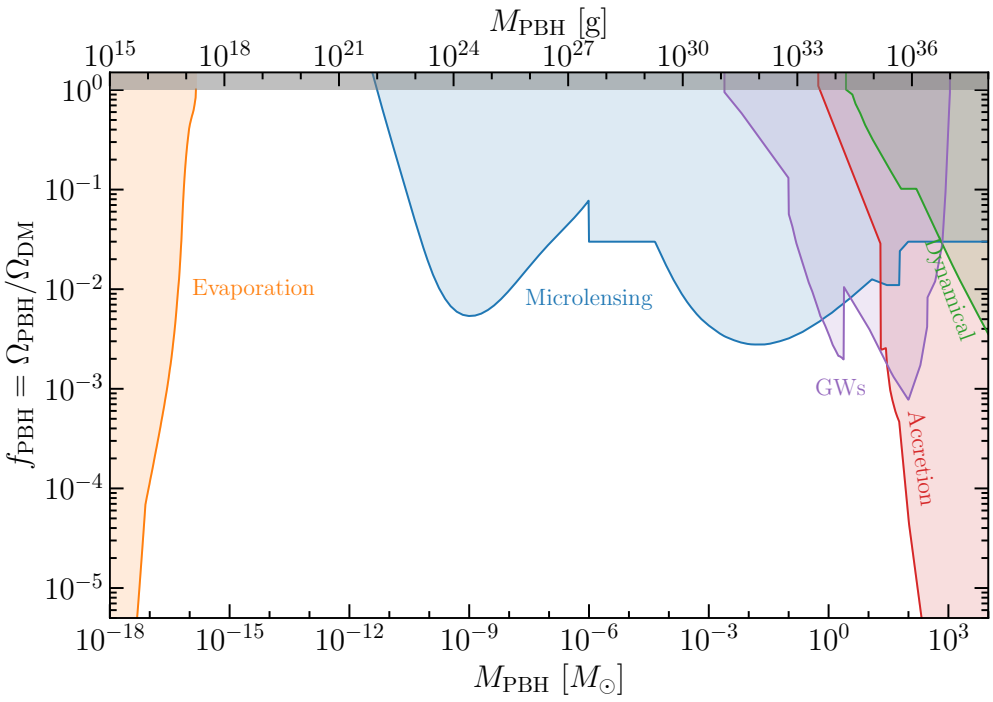

Figure 1.1: *Constraints on the fraction of dark matter in PBHs, $f_{\rm PBH}$, assuming all PBHs have the same mass $M_{\rm PBH}$, from PBH evaporation, microlensing, gravitational waves (GWs), accretion and dynamical effects. For each type of constraint, the most stringent limit is shown. This plot was produced using PBHbounds [154, 158].*

constraints from Refs. [159, 160] considered in Chapter 3 and to include the microlensing constraint from highly-magnified stars from Ref. [161].

Evaporation

Black holes radiate with a temperature inversely proportional to their mass, $T_{\rm BH} \propto 1/M_{\rm BH}$ [84, 85]. PBHs with an initial mass $M_{\rm PBH,i} \lesssim 5 \times 10^{14}\,{\rm g}$ have evaporated by the present [86, 87] and so cannot constitute the DM today, while PBHs of initial mass $M_{\rm PBH,i} \gtrsim 1 \times 10^{15}{\rm g}$ lose less than $\sim 10\%$ of their mass over their lifetimes. PBHs of mass $M_{\rm PBH} \lesssim 10^{17}\,{\rm g}$ can emit detectable levels of Hawking radiation, provided their abundance is sufficiently large. The types of particle emitted and their flux depend on the PBH temperature and therefore the PBH mass. Constraints on $f_{\rm PBH}$

can be obtained by comparing the flux of particles emtited from PBHs with observations (see Ref. [162] for a review of PBH evaporation constraints).

Evaporation constraints rule out $f_{\rm PBH} = 1$ for PBH masses up to a few times $10^{17}\,{\rm g}$. Many evaporation constraints are quite similar to one another and the uncertainties in the constraints are often larger than the differences between them. Constraints on PBH dark matter arise from (approximately in order of the maximum PBH mass for which $f_{\rm PBH} = 1$ is excluded) limits on PBH neutrino emission from Super-Kamiokande [163–165], CMB anisotropies [166–169], measurements of the flux of electrons and positrons by Voyager 1 [159, 170] and AMS-02 [171], the extragalactic gamma-ray background [156, 160, 163, 172], the 511 keV line [164, 170, 173, 174] and MeV gamma-rays from the Galactic Centre [170, 175, 176]. The 21 cm signal detected by EDGES has been used to constrain $f_{\rm PBH} < 1$ for $M_{\rm PBH} \lesssim (1-3) \times 10^{17}\,{\rm g}$ [169, 177], however the EDGES detection has not been verified by the SARAS-3 experiment [178, 179]. Constraints have also been placed on PBHs with initial masses $M_{\rm PBH,i} \lesssim 5 \times 10^{14}\,{\rm g}$ that have evaporated by today and so cannot constitute the DM (which are also covered in Ref. [162]).

Provided the contribution to the flux from astrophysical sources is well-understood, evaporation constraints can be tightened by subtracting their contribution. Ref. [180] finds constraints from the extragalactic gamma-ray background are tightened by ~ 2 orders of magnitude when accounting for gamma-ray emission from star forming galaxies and active galactic nuclei, while constraints from Voyager 1 become more stringent by more than an order of magnitude at $M_{\rm PBH} \lesssim 10^{16}\,{\rm g}$ (and by a smaller amount at larger masses) when subtracting the $e^{\pm}$ flux from pulsar wind nebulae and supernova remnants [159]. Refs. [160, 181] used a template fit, which accounts for the spatial distribution of the gamma-ray flux expected from

astrophysical sources and dark matter, to obtain tighter constraints from observations of MeV gamma rays. By isolating the gamma-ray flux from a component following an NFW profile (as expected for the dark matter), they find $f_{\rm PBH} < 1$ for PBHs of mass $M_{\rm PBH} \lesssim (3-4) \times 10^{17}\,{\rm g}$.

Microlensing

Microlensing is a form of strong gravitational lensing in which the separation between the images produced by the lensing object is too small for the images to be resolved separately. Due to the relative motion of the lens and the source, the lensing effect appears as a temporary (achromatic) brightening of the source [182]. Since the 1990s, surveys have searched for stellar microlensing events due to compact objects (such as PBHs) in the dark matter halos of the Milky Way and other nearby galaxies. The typical duration of a microlensing event scales with the mass of the lensing object, $M_{\rm lens}$, as $M_{\rm lens}^{1/2}$, so the range of lens masses a survey is sensitive to depends on the cadence and total duration of the survey.

The results of these surveys suggest that PBHs with masses $10^{-11} M_\odot \lesssim M_{\rm PBH} \lesssim 10^4 M_\odot$ cannot constitute all of the dark matter. Observations of stars in M31 by Subaru-HSC constrain PBHs of up to planetary masses ($10^{-11} M_\odot \lesssim M_{\rm PBH} \lesssim 10^{-6} M_\odot$) [183]. The OGLE Galactic Bulge survey has ruled out $f_{\rm PBH} = 1$ for PBHs of planetary to stellar masses (up to $M_{\rm PBH} \sim 10^{-1} M_\odot$) [184]. Surveys of the Large and Small Magellanic Clouds by MACHO [185], EROS [186] and OGLE [187] have constrained the mass range $10^{-7} M_\odot \lesssim M_{\rm PBH} \lesssim 10^4 M_\odot$. The most recent OGLE results, which appear in Ref. [187], were released after the work in Chapter 2 was published, so the constraints they obtained are not considered in that chapter.

These constraints are subject to uncertainties in the modelling of PBHs and in the distribution of DM. Uncertainties in the DM density profile and velocity distribution lead to an order of magnitude uncertainty in the largest PBH mass constrained by stellar microlensing and a factor of $\mathcal{O}(2-3)$ uncertainty in the strength of the constraint at a given PBH mass [188–191]. The constraints discussed above assume PBHs are unclustered and have a single mass. We investigate the effect of clustering (for PBHs formed from the collapse of large gaussian density fluctuations) in Chapter 2.

There are also observational challenges. Microlensing events can be caused by lenses of astrophysical origin, such as planets, main-sequence stars and stellar remnants (e.g. neutron stars, white dwarfs and black holes of astrophysical origin) [184]. Microlensing surveys designed to constrain PBH DM are usually directed towards sources away from the Galactic disk (such as the Magellanic Clouds and M31) to minimise this contribution. There is also a contribution from 'self-lensing', which describes microlensing by stars in the source galaxy. Additionally, due to the limited resolution of telescopes, multiple individual stars may appear as a single object, an effect known as 'blending'. If only one of the stars in the object is lensed, the change in the brightness of the lensed star will appear smaller due to the additional flux from the other star(s) in the object, making it more difficult to detect microlensing events.

Microlensing can also constrain the abundance of PBHs on cosmological scales. Quasars can be multiple-imaged due to strong lensing by galaxy clusters. Stars and other compact objects such as black holes can then temporarily magnify one of the images [192, 193]. Ref. [194] used optical observations of quasar image pairs to constrain $f_{\rm PBH} \lesssim 10^{-2}$ for $M_\odot \lesssim M_{\rm PBH} \lesssim 10^2 M_\odot$. Ref. [195] used X-ray observations of quasars to probe smaller PBH masses, finding a constraint $f_{\rm PBH} < 1$ for $10^{-3} M_\odot \lesssim M_{\rm PBH} \lesssim$

$10^{-1} M_\odot$. The mass range $10^{-1} \lesssim M_{\rm PBH} \lesssim M_\odot$ is not constrained since this method cannot distinguish BHs in this mass range from stars.

Stars that pass close to caustics (regions where the magnification becomes extremely large) of a lensing galaxy cluster can be magnified by a factor of ~ 1000. This allows stars at cosmological distances to be temporarily detected [196, 197]. Stars and other compact objects distort the smooth caustic produced by the cluster into a corrugated network of lines with an angular width proportional to their surface density. Compared to the case of a smooth lens, highly-magnified images can appear over a larger area, though the maximum image magnification is reduced [198–200]. Ref. [161] found that the positions of images of 9 highly-magnified stars can be explained by the known stellar population which contributes to the intracluster light, leading to a constraint that PBHs of mass $M_{\rm PBH} \gtrsim 10^{-6} M_\odot$ cannot make up more than $\approx 3\%$ of the DM.

Weaker constraints come from observations of type-1a supernovae. The presence of PBHs would shift the distribution of supernova magnifications to smaller values and give rise to a tail at large magnifications [201]. Ref. [202] found that observations of type-1a supernovae do not allow PBHs of mass $M_{\rm PBH} \lesssim 0.4 M_\odot$ to make up more than $\sim 40\%$ of the DM. However, Ref. [203] has argued that these constraints are too stringent since they were obtained assuming overly-narrow cosmological priors and that the supernova sizes were underestimated.

Gravitational waves

If two PBHs form sufficiently close to one another, they will decouple from the Hubble expansion due to their mutual gravitational attraction. A third PBH can induce a tidal force, preventing a head-on collision, in which

case the PBH pair forms a highly eccentric binary. If these binaries are not subsequently disrupted, the PBHs lose orbital energy by gravitational wave (GW) emission and eventually merge [204, 205]. If all the DM was in PBHs of mass $0.1M_\odot \lesssim M_{\rm PBH} \lesssim 300M_\odot$, the present-day merger rate of these early-forming binaries would be larger than that inferred from LIGO/Virgo/KAGRA (LVK) by an order of magnitude or more [206–209]. Recently, Ref. [209] constrained the PBH abundance using data from the third observation run (O3a) of LVK. They considered a variety of PBH mass functions, finding a constraint $f_{\rm PBH} \lesssim 10^{-3}$ for $M_{\rm PBH} \sim (1-300)M_\odot$ in all cases. They calculated the constraint assuming gaussian curvature perturbations, and also for the probability distributions of ζ obtained from ultra slow-roll inflation and the curvaton model (a multi-field inflationary model), finding the constraints do not change significantly compared to the gaussian case. Ref. [210] searched for mergers involving one or more subsolar-mass BHs (which must be of primordial origin) in LVK O3a data. They found no candidate merger events, leading to a constraint $f_{\rm PBH} < 1$ for PBHs of mass $2 \times 10^{-3}M_\odot \lesssim M_{\rm PBH} \lesssim 10^{-2}M_\odot$ for equal-mass PBH binaries. PBH binaries can also form at late times, by dynamical capture in DM substructures [211, 212] or three-body interactions [213], though the contribution to the present-day merger rate from late-forming binaries is subdominant compared to early-forming binaries [213, 214]. Merging PBHs which produce GW signals too weak to be resolved individually contribute to a stochastic gravitational wave background. The non-observation of such a background by LIGO/Virgo/KAGRA [215] leads to a constraint $f_{\rm PBH} \lesssim 0.1$ for $0.1M_\odot \lesssim M_{\rm PBH} \lesssim 10^3M_\odot$ [208, 216].

As discussed in Sec. 1.4.4, initially Poisson-distributed PBHs form clusters shortly after matter-radiation equality. A PBH binary in a cluster may be perturbed by the presence of surrounding PBHs [217], modifying the semi-

major axis and eccentricity of the binary. These effects tend to increase the merger timescale and suppress the present-day merger rate [218–220]. Refs. [221, 222] find that strong initial clustering of PBHs may increase the PBH merger rate and tighten constraints, while Ref. [223] comes to the opposite conclusion.

When PBHs do not make up all of the DM, particle DM halos will form around PBHs [224, 225]. Refs. [207, 226] found the presence of particle DM halos typically increases PBH merger rates by less than an order of magnitude. However, Ref. [227] found that particle DM halos may increase or decrease the merger rate by many orders of magnitude, depending on the PBH mass function and whether the steep particle DM 'spike' at the centre of the halo persists throughout the merger process.

Accretion

PBHs of masses $M_{\rm PBH} \gtrsim (1-10)M_\odot$ are constrained by the radiation emitted as gas accretes onto them. In the early Universe, the emitted radiation would affect recombination, allowing constraints to be placed from observations of CMB anisotropies [228, 229]. Ref. [230] obtained a constraint by requiring that the radiation from accreting PBHs does not heat gas more than allowed by the 21 cm signal detected by EDGES (though, as mentioned in the discussion on evaporation constraints, the EDGES signal has not been verified by other observations [179]). At late times, accretion onto PBHs would give rise to detectable radio and X-ray emission [231, 232], leading to a constraint $f_{\rm PBH} \lesssim 10^{-3}$ for $M_{\rm PBH} \sim (30-100)M_\odot$ from Chandra and the VLA survey of the Galactic Centre [232]. Ref. [233] used the number density of X-ray binaries to constrain $f_{\rm PBH} < 1$ for PBHs of mass $3M_\odot \lesssim M_{\rm PBH} \lesssim 10^7 M_\odot$. Requiring that gas in the Leo T dwarf

galaxy is not excessively heated by radiation produced during accretion onto PBHs (and dynamical heating due to PBHs) rules out $f_{\rm PBH} = 1$ for PBHs of mass $M_{\rm PBH} \sim (1 - 10^7) M_\odot$ [234, 235].

There are large theoretical uncertainties in the modelling of PBH accretion, and hence substantial variation between constraints claimed in the literature. Accounting for the formation of an accretion disk around PBHs strengthens constraints by around two orders of magnitude [236], and the impact of winds and/or jets leads to order of magnitude or greater uncertainties on constraints [237] (see also Ref. [238]). Ref. [239] has argued that accounting for ionisation of gas around the PBH relaxes constraints, though Ref. [240] finds limits comparable to those that do not include ionisation. PBH clustering (for initially Poisson-distributed PBHs) has only a small effect on CMB accretion constraints [150, 241]. Refs. [228, 242] found that accounting for the presence of particle DM halos around PBHs when $f_{\rm PBH} < 1$ can significantly increase the accretion rate and tighten constraints, though Ref. [240] finds that when considering a more realistic PBH accretion model particle DM halos have only a small effect on constraints.

Dynamical constraints

Encounters in a system consisting of two populations of objects with different masses cause the kinetic energies of each population to become more equal. In a dwarf galaxy consisting of stars and more massive compact objects (such as PBHs), the result is that the stellar component expands while the compact objects move towards the centre of the dwarf galaxy. Observations of the half-light radii of ultra-faint dwarf galaxies constrain $f_{\rm PBH} < 1$ for PBHs of mass $M_{\rm PBH} \gtrsim 10 M_\odot$ [243, 244], with the limit tightening to

$f_{\rm PBH} \lesssim 10^{-3}$ at $M_{\rm PBH} \sim 10^4 M_\odot$ [244]. There may also be constraints from the survival of the star cluster at the centre of the dwarf galaxy Eridanus II [243] and the lack of a ring feature in Segue I, which Ref. [245] predicted would be generated by PBHs of mass $M_{\rm PBH} \gtrsim M_\odot$ (though such a feature has not been observed in numerical simulations [246]). Ref. [247] performed numerical simulations including PBHs of a single mass and with a lognormal mass function, finding that $f_{\rm PBH} = 1$ appears to be ruled out for $M_{\rm PBH} \sim \mathcal{O}(1-100) M_\odot$ in both cases.

Due to their low binding energies, wide stellar binaries can be easily disrupted by compact objects [248], so the survival of wide binaries in the Milky Way places constraints on the abundance of PBHs [249]. These constraints are very sensitive to the widest binaries in a sample, and one must confirm that candidate binaries actually consist of gravitationally bound stars using radial velocity measurements [250]. Ref. [251] found $f_{\rm PBH} \lesssim 0.1$ for $M_{\rm PBH} \gtrsim 70 M_\odot$, weakening with decreasing mass to $f_{\rm PBH} \lesssim 1$ for $M_{\rm PBH} = 3 M_\odot$, using the 25 wide binaries in their catalogue that spend the most time in the Galactic halo over their lifetimes. Ref. [252] stressed that the initial semi-major axis distribution of wide binaries must be known in order to place constraints on PBHs. Ref. [253] revisited the wide binary constraints from Ref. [251], accounting for effects which increase the apparent number of wide binaries for a given number of compact objects and using an initial semi-major axis distribution motivated by simulations of wide binary formation during the dissolution of star clusters. They find significantly weaker constraints than Ref. [251]: $f_{\rm PBH} < 0.3$ for $M_{\rm PBH} \gtrsim 10^3 M_\odot$, weakening with decreasing $M_{\rm PBH}$ to $f_{\rm PBH} < 1$ for $M_{\rm PBH} \approx 300 M_\odot$.

Indirect constraints

Constraints on the primordial power spectrum indirectly constrain PBHs formed from the collapse of large overdensities. When translated to a constraint on $f_{\rm PBH}$, these indirect constraints are subject to large uncertainties in calculating the PBH abundance from a given primordial power spectrum [99, 254].

The dissipation of overdense regions (arising from having significant power in the primordial power spectrum on scales smaller than those probed by CMB observations) can drive matter and radiation out of equilibrium in the early Universe, giving rise to spectral distortions in the CMB that have been constrained by COBE/FIRAS [12]. Refs. [255, 256] found COBE/FIRAS observations exclude $f_{\rm PBH} = 1$ for $M_{\rm PBH} \gtrsim 10^4 M_\odot$. Constraints may be significantly weakened if the curvature perturbation distribution is highly non-gaussian [257–259].

Curvature perturbations inevitably generate gravitational waves upon entering the horizon after the end of inflation [260–262]. These are known as 'scalar-induced gravitational waves' (SIGWs). PBHs formed from the collapse of large density perturbations are therefore constrained by limits on the stochastic gravitational wave background [263]. Ref. [264] found a constraint $f_{\rm PBH} < 1$ for $10^{-1} M_\odot \lesssim M_{\rm PBH} \lesssim 10^3 M_\odot$ using the 15-year data release from NANOGrav [265, 266]. The constraint depends on the shape of the primordial power spectrum and is weakened in the presence of large non-gaussianity in the curvature perturbation distribution.

Another indirect probe comes from the effect of enhanced power in the primordial power spectrum on the freeze-out value of the neutron-proton ratio at the start of nucleosynthesis, which constrains $f_{\rm PBH} < 1$ for $10^3 M_\odot \lesssim$

$M_{\rm PBH} \lesssim 10^5 M_\odot$ [267]. Additionally, Poisson fluctuations in the PBH number density give rise to an enhancement in the primordial power spectrum above that expected in the standard cold DM scenario which can be probed using Lyman-α observations [149], leading to a constraint $f_{\rm PBH} M_{\rm PBH} \lesssim 60 M_\odot$ [268].

As mentioned above, when PBHs do not form all of the dark matter, they seed the formation of particle DM halos with steep density profiles. If the rest of the DM is made up of WIMPs, they will annihilate in the dense inner regions of these halos. For many WIMP models, the flux of gamma rays produced from annihilation around PBHs of mass $M_{\rm PBH} \gtrsim 10^{-6} M_\odot$ would be in tension with the observed level of the extragalactic gamma-ray background and CMB observations unless the PBH abundance is very small. This rules out scenarios in which PBHs and WIMPs can both constitute non-negligible fractions of the DM for a wide range of WIMP models [225, 269, 270].

The asteroid-mass window

Currently, there are no observational constraints on PBHs in the mass range $10^{17}\,{\rm g} \lesssim M_{\rm PBH} \lesssim 10^{22}\,{\rm g}$, often known as the 'asteroid-mass window'. A number of methods have been proposed to constrain this mass range.

An asteroid-mass PBHs passing through a neutron star may be captured by dynamical friction, after which the PBH rapidly accretes the material of the neutron star and destroys it [271, 272]. Ref. [271] placed a limit from the survival of neutron stars in globular clusters, which requires globular clusters to have high dark matter densities. It is thought that most globular clusters contain little dark matter [272] so in fact there is no constraint from neutron star survival [273]. The transit of a PBH through a white dwarf

may trigger runaway nuclear fusion and destroy the white dwarf [274]. The survival of white dwarfs is no longer believed to place a constraint on $f_{\rm PBH}$ [273], though limits may be placed if white dwarf destruction by a PBH produces a visible explosion [273]. Ref. [275] has noted the existence of a population of faint calcium-rich supernovae believed to originate from white dwarf explosions, which have an unusual spatial distribution (far from their presumed host galaxies), and suggested they might be caused by PBHs of mass $M_{\rm PBH} \gtrsim 10^{21}\,{\rm g}$. Ref. [276] proposed that PBH capture during the formation of main-sequence stars could occur at a sufficient rate to constrain PBHs of mass $10^{18}\,{\rm g} \lesssim M_{\rm PBH} \lesssim 10^{22}\,{\rm g}$ from the survival of stars in dwarf galaxies, though this depends on the maximum fraction of stars that can be destroyed (which has not yet been estimated).

Asteroid-mass PBHs could also be detected by gravitational lensing of gamma-ray bursts (GRBs). Lensing could be detected as fringes in the GRB frequency spectrum, which arise from interference between different unresolved images that travel different path lengths and experience different gravitational potentials (an effect known as 'femtolensing') [277]. Ref. [278] used the absence of femtolensing of GRBs detected by the Fermi Gamma-ray Burst Monitor to constrain $f_{\rm PBH} < 1$ for $5 \times 10^{17}\,{\rm g} \lesssim M_{\rm PBH} \lesssim 10^{20}\,{\rm g}$, though these constraints are removed when accounting for the finite size of the GRBs [279]. Another proposal is GRB microlensing parallax: two observers viewing a GRB will record the same flux in the absence of lensing (since GRBs occur at cosmological distances), while for a lensed GRB each observer would record a different flux [280–282].

Other proposed methods of constraining (or detecting) asteroid-mass PBHs include microlensing of X-ray pulsars [283, 284] and the effect on the distances between planets in the inner Solar System [285] and the orbits of satellites [286].

Constraints on PBHs with extended mass functions

For an extended mass function, constraints are 'smeared out'. For each constraint the tightest limit on $f_{\rm PBH}$ is weakened, while when considering multiple constraints the windows between constraints are narrowed or closed [126, 287, 288]. Ref. [287] presented a method to calculate extended MF constraints from a constraint calculated assuming all PBHs have the same mass (see also Ref. [289] for a similar approach) which we apply in Chapter 3. As emphasised in Ref. [287], this method has a number of caveats. For instance, the mass function may depend on position due to mass segregation (relevant for dynamical constraints from ultra-faint dwarf galaxies) and time (due to PBH mergers, accretion and evaporation). We explore the last of these caveats further in Chapter 3, since it is relevant when considering evaporation constraints on PBHs with extended mass functions.

1.5 Conclusions

We have reviewed the strong and varied evidence for the existence of dark matter and discussed its distribution. Most often, dark matter has been assumed to be a form of undiscovered particle species. In the absence of observational evidence for these particle dark matter candidates, primordial black holes (PBHs) have been considered as an alternative. We have discussed the formation of PBHs (from the collapse of large fluctuations in the radiation-dominated epoch), their abundance and observational constraints, which (taken at face value) rule out PBHs making up all of the dark matter except for PBHs of mass $10^{17}\,{\rm g} \lesssim M_{\rm PBH} \lesssim 10^{22}\,{\rm g}$, often known as the 'asteroid-mass window'.

These constraints are calculated making various assumptions about the mass and spatial distribution of PBHs. Constraints on the PBH abundance are usually calculated assuming they are smoothly distributed. However, PBHs are expected to form clusters shortly after matter-radiation equality even if they are not strongly clustered at formation. We consider the effect of clustering on microlensing constraints in Chapter 2. Another common assumption is that all PBHs have the same mass, though due to near-critical collapse, PBHs will form with an extended range of masses even if they all form at the same time. We investigate whether the asteroid-mass window remains open when considering constraints calculated using realistic extended mass functions in Chapter 3.

Chapter 2

Microlensing Constraints on Clustered Primordial Black Holes

2.1 Introduction

Stellar microlensing is the temporary magnification of a star that occurs when a compact object passes close to the line of sight to the star. Various microlensing surveys have placed tight constraints on PBHs (see Sec. 1.4.5), which if taken at face value exclude PBHs of mass $10^{-11} M_\odot \lesssim M_{\rm PBH} \lesssim 10^4 M_\odot$ from making up all of the dark matter. These constraints have been obtained assuming that the DM is smoothly distributed.

In this chapter, we assume PBHs are formed from the collapse of large gaussian density fluctuations generated by inflation. As discussed in Sec. 1.4.4, in this scenario, PBHs form at randomly-distributed points in space [118, 147, 148]. The resulting Poisson fluctuations in the initial distribution

of PBHs leads to clusters of PBHs forming shortly after matter-radiation equality [149, 150]. Refs. [109, 191, 290] have argued that clustering leads to microlensing constraints being shifted to smaller masses or evaded entirely, allowing PBHs of multiple Solar masses to make up all of the DM. These studies assumed that PBH clusters are sufficiently compact that the cluster as a whole acts as a single lens.

In this chapter, we investigate the effect of PBH clustering on stellar microlensing constraints, for PBHs formed from the collapse of large gaussian density fluctuations. In Sec. 2.2 we discuss the properties of the clusters. In Sec. 2.3, we outline the calculation of the microlensing differential event rate for smoothly-distributed DM (Sec. 2.3.1), the microlensing behaviour of PBHs in clusters (Sec. 2.3.2) and the calculation of the microlensing differential event rate for clustered DM (Sec. 2.3.3). We present our results in Sec. 2.4 and conclude in Sec. 2.5.

2.2 PBH Cluster Properties

Ref. [218] used the spherical collapse model (see Sec. 1.1.4) to calculate the properties of PBH clusters for PBHs formed from the collapse of large gaussian density fluctuations generated by inflation, assuming all PBHs have the same mass $M_{\rm PBH}$. The initial (Poisson) fluctuation in the number of PBHs in a volume containing N PBHs on average is $\delta(N) = 1/\sqrt{N}$. The growth of these isocurvature fluctuations is proportional to [150]

$$D(a) \approx \left(1 + \frac{3}{2}\frac{a}{a_{\rm eq}}\right), \tag{2.1}$$

where $a_{\rm eq}$ is the scale factor at matter-radiation equality.

In the spherical collapse model, a virialised cluster of PBHs forms at a scale factor $a_{\rm coll}$ when the linear solution for the overdensity reaches a critical value $D(a_{\rm coll})\delta(N) = \delta_{\rm c}$, where $\delta_c \approx 1.69$ [1]. From Eq. (2.1), $a_{\rm coll}$ is given by

$$a_{\rm coll} \approx \frac{2}{3}\left(\delta_{\rm c}\sqrt{N} - 1\right) a_{\rm eq}. \tag{2.2}$$

The final density of the cluster is approximately $\rho_{\rm cl} \approx 178\rho_{\rm DM}(a_{\rm coll})$, where $\rho_{\rm DM}$ is the average background DM density. Using $\rho_{\rm DM} \propto a^{-3}$, $\rho_{\rm cl}$ can be written as

$$\rho_{\rm cl}(a_{\rm coll}) \approx 178\rho_{\rm DM,0}\left(\frac{a_{\rm coll}}{a_0}\right)^{-3} \tag{2.3}$$

$$\approx 178 \times \frac{3H_0^2\Omega_{\rm DM}}{8\pi G}\left(\frac{a_{\rm coll}}{a_{\rm eq}}\right)^{-3}\left(\frac{a_{\rm eq}}{a_0}\right)^{-3}, \tag{2.4}$$

where in the second equality we have written the present DM density $\rho_{\rm DM,0} = \Omega_{\rm DM}\rho_{\rm c,0}$ and we used the Friedmann equation (Eq. (1.12)) to rewrite the present value of the critical density $\rho_{\rm c,0}$. Using $a_{\rm coll}/a_{\rm eq}$ from Eq. (2.2), $a_{\rm eq}/a_0$ from Eq. (1.13), $H_0 = 67.4\,{\rm km\,s^{-1}\,Mpc^{-1}}$ and $\Omega_{\rm DM} = 0.26$ [4], the number density, $n_{\rm cl}$, of PBHs within a cluster consisting of $N_{\rm cl}$ PBHs is then

$$n_{\rm cl} = \frac{\rho_{\rm cl}}{M_{\rm PBH}} \approx 1.7 \times 10^5 N_{\rm cl}^{-3/2}\left(\frac{M_\odot}{M_{\rm PBH}}\right)\,{\rm pc}^{-3}, \tag{2.5}$$

where we have assumed $\sqrt{N_{\rm cl}} \gg 1$. The cluster radius, $R_{\rm cl}$, can be estimated, using $N_{\rm cl} = (4\pi/3)n_{\rm cl}R_{\rm cl}^3$, to give

$$R_{\rm cl} \approx 1.1 \times 10^{-2} N_{\rm cl}^{5/6}\left(\frac{M_{\rm PBH}}{M_\odot}\right)^{1/3}\,{\rm pc}. \tag{2.6}$$

[1] The value of the critical overdensity is $\delta_c \approx 1.69$ only for collapse that occurs in a matter-dominated universe. For collapse occurring shortly after matter-radiation equality, the value of $\delta_{\rm c}$ is slightly larger (see appendix A and Fig. 14 of Ref. [150]), though the effect on the estimated cluster properties is small.

The virial velocity, $\sigma_{\rm cl}$, of PBHs within clusters is approximately given by [218]

$$\sigma_{\rm cl} \approx 0.6 \left(\frac{M_{\rm PBH}}{M_\odot}\right)^{1/3} N_{\rm cl}^{1/12} \,{\rm km\,s^{-1}}. \tag{2.7}$$

Numerical simulations [150] find that the number of PBH clusters containing $N_{\rm cl}$ objects at a given time is well-described by the theoretical prediction for initially Poisson-distributed objects [291]. For $N_{\rm cl} \gg 1$, the number of clusters containing $N_{\rm cl}$ PBHs is [150, 291]

$$\tilde{N} \propto \frac{\delta_*}{N_{\rm cl}^{3/2}} \exp\left(-\frac{N_{\rm cl}}{N_*}\right), \tag{2.8}$$

where $\delta_*(a) = \delta_c/D(a)$ and

$$N_* \equiv \left(\log(1+\delta_*) - \frac{\delta_*}{1+\delta_*}\right)^{-1}. \tag{2.9}$$

Since $\tilde{N}$ is a monotonically decreasing function of $N_{\rm cl}$, clusters with small $N_{\rm cl}$ are the most abundant at all times. However, since N_* grows with time, the number of clusters with large $N_{\rm cl}$ increases with time.

Clusters of small numbers of objects are unstable due to evaporation [48]. PBH clusters with $N_{\rm cl} \lesssim 10^3$ will have evaporated by the present [149, 218], independent of the PBH mass. Since the number of PBH clusters with $N_{\rm cl}$ members is a monotonically decreasing function of $N_{\rm cl}$, we expect most clusters today to contain $N_{\rm cl} \sim 10^3$ PBHs.

2.3 Microlensing

Microlensing can be detected as a temporary achromatic magnification of a source star. When the lens and source star are both point-like, the

amplification is [182]

$$A(u) = \frac{u^2+2}{u(u^2+4)^{1/2}}, \tag{2.10}$$

where u is the distance of the source from the lens on the sky, in units of the Einstein radius $R_{\rm E}$,

$$R_{\rm E}(x) = 2\left[GM_{\rm PBH}x(1-x)L\right]^{1/2} \tag{2.11}$$

$$\approx 10^{-4}\,{\rm pc}\left[\left(\frac{M_{\rm PBH}}{M_\odot}\right)\left(\frac{L}{50\,{\rm kpc}}\right)x(1-x)\right]^{1/2}, \tag{2.12}$$

where $M_{\rm PBH}$ is the mass of the lens, L is the distance of the source from the observer (normalised to the LMC distance $L \approx 50\,{\rm kpc}$ [292]) and x is the observer-lens distance in units of L. When the separation of the source and the lens on the sky is no greater than $R_{\rm E}$ (i.e. $u \leq 1$), from Eq. (2.10) the amplification of the source star is $A \geq 1.34$. The duration of a microlensing event is the time taken for a lens to cross the Einstein diameter [2],

$$\hat{t} = 2R_{\rm E}(x)/v_\perp \tag{2.13}$$

$$\approx 300\left[\left(\frac{M_{\rm PBH}}{M_\odot}\right)\left(\frac{L}{50\,{\rm kpc}}\right)x(1-x)\right]^{1/2}\left(\frac{220\,{\rm km\,s^{-1}}}{v_\perp}\right)\,{\rm days}, \tag{2.14}$$

where $v_\perp$ is the transverse velocity of the lens.

2.3.1 Differential event rate (smooth halo)

For a smooth DM halo consisting entirely of compact objects of mass $M_{\rm PBH}$ with a density profile $\rho(x)$ and a Maxwellian velocity distribution (Eq. (1.38)), the microlensing differential event rate (the rate of microlens-

[2]Some microlensing studies (e.g. Refs. [186, 187]) define the event duration as the time taken to cross the Einstein radius rather than the Einstein diameter.

ing events per source star as a function of $\hat{t}$), $\mathrm{d}\Gamma/\mathrm{d}\hat{t}$, is [188, 293]

$$\frac{\mathrm{d}\Gamma}{\mathrm{d}\hat{t}} = \frac{32L}{\hat{t}^4 M_{\mathrm{PBH}} v_{\mathrm{c}}^4} \int_0^1 \rho(x) R_{\mathrm{E}}^4(x) e^{-Q(x)} \mathrm{d}x, \tag{2.15}$$

where $Q(x) = 4R_{\mathrm{E}}^2(x)/(\hat{t}^2 v_{\mathrm{c}}^2)$ and $v_{\mathrm{c}} = 220\,\mathrm{km\,s^{-1}}$ is the Milky Way circular speed.

We adopt the standard halo model for microlensing studies (the 'Model S' in Ref. [188]). In this model, the halo has a cored isothermal density profile (Eq. (1.36)) with a local DM density $\rho_0 = 7.9 \times 10^{-3}\,M_\odot\,\mathrm{pc}^{-3}$ and a Galactic core radius $R_{\mathrm{c}} = 5\,\mathrm{kpc}$, while the Galactocentric distance of the Sun is $R_0 = 8.5\,\mathrm{kpc}$ [3]. For this model, the differential event rate can be written as [188]

$$\frac{\mathrm{d}\Gamma}{\mathrm{d}\hat{t}} = \frac{512\rho_0(R_{\mathrm{c}}^2 + R_0^2)LG^2 M_{\mathrm{PBH}}}{\hat{t}^4 v_{\mathrm{c}}^2} \int_0^1 \frac{x^2(1-x)^2}{A + Bx + x^2} e^{-Q(x)} \mathrm{d}x, \tag{2.16}$$

where $A = (R_{\mathrm{c}}^2 + R_0^2)/L^2$, $B = -2(R_0/L)\cos b \cos l$ and $(b, l) = (-32.8^\circ, 281^\circ)$ are the galactic latitude and longitude of the LMC, respectively.

Strictly speaking, the Maxwellian velocity distribution should only be used for a density profile of the form $\rho(R) \propto R^{-2}$ (see Sec. 1.2.2), though in practice it is widely used with the cored isothermal profile of the standard halo model [185, 186, 188]. This is a reasonable choice since microlensing events of LMC stars are most likely to be caused by lenses at galactocentric distances R for which $(R/R_{\mathrm{c}})^2 \gg 1$, where the R-dependence of the standard halo model density profile is well-approximated as $\rho(R) \propto R^{-2}$.

[3] We use these 'traditional' values for consistency with previous analyses of microlensing surveys, though we note that more recent measurements have found different best-fit values for some of these parameters. For example, the GRAVITY collaboration has measured a smaller value for the galactocentric distance of the Sun with a very high precision, $R_0 = (8.18 \pm 0.01 \pm 0.02)\,\mathrm{kpc}$ [294]. The effect of the differences from the traditional values on the differential event rate is smaller than the uncertainty from the choice of density profile [190, 191].

The expected number of events, $N_{\rm exp}$, is

$$N_{\rm exp} = E \int_0^\infty \epsilon(\hat{t}) \frac{{\rm d}\Gamma}{{\rm d}\hat{t}} {\rm d}\hat{t}, \tag{2.17}$$

where E is the exposure (number of stars observed multiplied by the survey duration), and $\epsilon(\hat{t})$ is the detection efficiency for events of duration $\hat{t}$ (the probability that a microlensing event of duration $\hat{t}$ will be detected). The actual number of events follows a Poisson distribution with a mean given by Eq. (2.17) [293].

2.3.2 Microlensing behaviour of clustered PBHs

The spherical collapse model predicts the typical separation of PBHs in a cluster, $n_{\rm cl}^{-1/3}$, is much larger than the Einstein radius of a single PBH. For instance, for Solar-mass PBHs, $n_{\rm cl}^{-1/3} \sim 10^{-2} N_{\rm cl}^{1/2}\,{\rm pc}$ while $R_{\rm E} \sim 10^{-4}\,{\rm pc}$. In such diffuse clusters, each PBH behaves as an independent lens. This is different from the compact clusters considered in Refs. [191, 290] in which the entire cluster acts as a single lens. For large $N_{\rm cl}$ and/or $M_{\rm PBH}$, Eq. (2.6) predicts cluster radii so large that the clusters could overlap. To avoid this issue we follow Ref. [295] and set $R_{\rm cl} = 10\,{\rm pc}$. The condition for PBHs to act as independent lenses ($n_{\rm cl}^{-1/3} \gg R_{\rm E}$) is satisfied when using $R_{\rm cl} = 10\,{\rm pc}$ even for the most massive clusters we consider.

We next outline some arguments about how clustering could affect microlensing by PBHs, and explain why they do not apply for PBH clusters from the collapse of gaussian density fluctuations.

Binary PBHs Some fraction of PBHs are expected to form binaries [204, 206, 218]. If these binaries form in the early Universe and survive to

the present, or PBHs form binaries at sufficiently late times, this presents the possibility of PBHs causing multiple microlensing events of the same source star while it is being observed. Since repeated variability in the source brightness is usually attributed to intrinsic variability in the source star, repeated microlensing events caused by PBHs in binaries may be missed [295]. However, Ref. [295] calculated that the minimum time between lensing events from PBHs in a binary would be on the order of 100 years, much longer than the duration of any microlensing survey.

Lensing by the whole cluster Ref. [109] argued that the deflection of light by a PBH cluster as a whole would make microlensing by individual PBHs undetectable. However, this conclusion relies on an underestimate of the Einstein radius. We outline their argument below, using the corrected Einstein radius.

Light rays from a source star are deflected by an axially symmetric mass distribution $M(\xi)$ (where ξ is the radial coordinate perpendicular to the line of sight from the observer to the centre of mass of the lens) by an angle

$$\alpha = \frac{4GM(\xi)}{\xi}, \tag{2.18}$$

where $M(\xi)$ is the lensing mass enclosed within a cylinder of radius ξ. Eq. (2.18) is maximised for a light ray passing at a distance $\xi = R_{\rm cl}$ from the cluster centre. The largest deflection possible is therefore

$$\alpha = 5 \times 10^{-11} \frac{M_{\rm cl}}{10^3 M_\odot} \frac{4 \text{ pc}}{R_{\rm cl}}, \tag{2.19}$$

where $R_{\rm cl}$ and the cluster mass, $M_{\rm cl} = N_{\rm cl} M_{\rm PBH}$, are normalised to the approximate values for the lowest-mass PBH clusters we consider ($N_{\rm cl} = 10^3$, $M_{\rm PBH} = M_\odot$).

Ref. [109] argues that $l \gg R_{\rm E}$ for Solar-mass PBHs in clusters of mass $M_{\rm cl} \gtrsim 10^3\,M_\odot$, so the magnification of the star's light due to individual PBHs is too small to be observed. The Einstein radius they adopt for Solar-mass PBHs ($R_{\rm E} \sim 10^{-8}\,{\rm pc}$) is much smaller than the typical value from Eq. (2.12) of $R_{\rm E} \sim 10^{-4}\,{\rm pc}$. From Eqs. (2.12) and (2.19), we find

$$\frac{l}{R_{\rm E}} \approx 0.02 \left(\frac{x}{1-x}\right)^{1/2} \left(\frac{M_{\rm cl}}{M_\odot}\right) \left(\frac{4\ {\rm pc}}{R_{\rm cl}}\right) \left(\frac{L}{50\ {\rm kpc}}\right)^{1/2} \left(\frac{M_\odot}{M_{\rm PBH}}\right)^{1/2}. \tag{2.20}$$

Using Eq. (2.6) for $R_{\rm cl}$ and $M_{\rm cl} = N_{\rm cl} M_{\rm PBH}$, we obtain

$$\frac{l}{R_{\rm E}} \approx 0.02 \left(\frac{x}{1-x}\right)^{1/2} \left(\frac{N_{\rm cl}}{10^3}\right)^{1/6} \left(\frac{L}{50\ {\rm kpc}}\right)^{1/2} \left(\frac{M_{\rm PBH}}{M_\odot}\right)^{1/6}. \tag{2.21}$$

Therefore, $l/R_{\rm E} \ll 1$ for what we expect to be the most common number of PBHs per cluster cluster, $N_{\rm cl} \sim 10^3$, in the whole range of PBH masses we consider ($M_\odot \leq M_{\rm PBH} \leq 10^3\,M_\odot$), for typical cluster distances x.

2.3.3 Differential event rate (clustered halo)

To calculate the differential event rate for clustered PBHs, we follow a similar approach to Refs. [295–297]. We assume a fraction f [4] of DM is in PBHs, and assume all PBHs are found in clusters containing $N_{\rm cl}$ PBHs. As discussed in Sec. 2.2, clusters containing $N_{\rm cl} \lesssim 10^3$ PBHs are expected to have evaporated by the present. Furthermore, from Eq. (2.8), small clusters are the most abundant at formation. It is therefore likely that a significant fraction of PBHs are unclustered today, so our results represent an upper limit of the effect of clustering on stellar microlensing constraints.

We approximate the LMC as a circle on the sky subtending a solid angle

[4] The standard notation for this quantity is $f_{\rm PBH}$. In this Chapter, we adopt the notation f to make later expressions clearer and more concise.

$\Omega_{\rm LMC} = 84\,{\rm deg}^2$, matching the area of the LMC observed by EROS-2 [186]. The region in which PBHs can cause microlensing of LMC stars is therefore a cone (the 'microlensing cone') with half-angle $\theta = 5.2°$. The total mass of DM within the microlensing cone, which can be calculated using Eq. (1.36) for the standard halo model, is $M_{\rm cone} \sim 10^9 M_\odot$. PBH clusters that lie either fully or partially in the microlensing cone contribute to the differential event rate. Therefore, we consider all clusters with centres lying in a region which is centred on the microlensing cone and has radius equal to the width of the microlensing cone plus the cluster radius at each x: $R_{\rm tcone}(x) = R_{\rm cone}(x) + R_{\rm cl}$, where $R_{\rm cone}(x) = xL\tan\theta$ is the width of the microlensing cone. This region has the shape of a truncated cone.

Clustering introduces stochasticity into the spatial distribution of PBHs and their velocities, so we use Monte Carlo simulations to determine the differential event rate, $\mathrm{d}\Gamma/\mathrm{d}\hat{t}$. First, for each pair of $M_{\rm PBH}$ and $N_{\rm cl}$, we find the mean number of clusters with centres in the truncated cone,

$$N_{\rm tcone} = \frac{f M_{\rm tcone}}{M_{\rm PBH} N_{\rm cl}}, \tag{2.22}$$

where $M_{\rm tcone}$ is the total mass of DM in the truncated cone. For each realisation, the actual number of clusters is drawn from a Poisson distribution with mean $N_{\rm tcone}$.

We generate a cluster line-of-sight distance, $x_{\rm cl}$, following a probability distribution function $P(x_{\rm cl}) \propto \rho(x_{\rm cl}) R^2_{\rm tcone}(x_{\rm cl})$ to account for the varying DM density and width of the truncated cone along the line of sight. The cluster radius is much smaller than the LMC distance, $L = 50\,{\rm kpc}$, or the typical cluster distance, $x_{\rm cl}L \sim \mathcal{O}(10)\,{\rm kpc}$, so we approximate all PBHs within a given cluster as having the same line-of-sight distance, $x_{\rm cl}$. The cluster transverse velocity, $v_{\perp,{\rm cl}}$, is generated following a 2-dimensional Maxwellian

distribution with $v_c = 220\ \mathrm{km\,s^{-1}}$. Since the virial velocity from Eq. (2.7) is negligible compared to the typical cluster transverse velocity, we neglect it and assume all PBHs within a cluster move with the cluster transverse velocity, $v_{\perp,\mathrm{cl}}$. To calculate the fractional cross-sectional area of the cluster lying within the microlensing cone, $\hat{f}$, we also generate a distance between the centre of the cluster and the line-of-sight from the observer to the LMC, assuming that the cluster centres are uniformly distributed across the cross-section of the truncated cone at all x.

We next calculate the rate of microlensing events from each cluster. The optical depth is the probability that the separation between a lens and source star on the sky is smaller than the Einstein radius R_E (see e.g. Ref. [298]). The optical depth of a cluster, τ_cl, is the product of the lensing cross-section of a PBH (πR_E^2), the surface number density of PBHs in the cluster and the fraction of the solid angle of the LMC that is covered by the cluster [297]:

$$\tau_\mathrm{cl} = (\pi R_\mathrm{E}^2)\frac{N_\mathrm{cl}}{\pi R_\mathrm{cl}^2}\frac{\Omega_\mathrm{cl}}{\Omega_\mathrm{LMC}}\hat{f} = \frac{N_\mathrm{cl}\pi R_\mathrm{E}^2}{x_\mathrm{cl}^2 L^2 \Omega_\mathrm{LMC}}\hat{f}, \tag{2.23}$$

where $\Omega_\mathrm{cl} = \pi R_\mathrm{cl}^2/(x_\mathrm{cl}L)^2$ is the solid angle subtended by the cluster. The event rate for a given cluster, Γ_cl, is given by the time derivative of the optical depth. Since all PBHs within a cluster have the same transverse velocity $v_{\perp,\mathrm{cl}}$, the area swept out by each lens in a time $\mathrm{d}t$ is $\mathrm{d}A_\mathrm{lens} = 2R_\mathrm{E}v_{\perp,\mathrm{cl}}\mathrm{d}t$. The area on the sky within the Einstein radius of each lens is $A_\mathrm{lens} = \pi R_\mathrm{E}^2$, so from Eq. (2.23),

$$\Gamma_\mathrm{cl} = \frac{\mathrm{d}\tau_\mathrm{cl}}{\mathrm{d}t} = \frac{\mathrm{d}\tau_\mathrm{cl}}{\mathrm{d}A_\mathrm{lens}}\frac{\mathrm{d}A_\mathrm{lens}}{\mathrm{d}t} \tag{2.24}$$

$$= \frac{2N_\mathrm{cl}R_\mathrm{E}v_{\perp,\mathrm{cl}}}{x_\mathrm{cl}^2 L^2 \Omega_\mathrm{LMC}}\hat{f}. \tag{2.25}$$

Since the Einstein radius, R_E, and transverse velocity, $v_{\perp,\mathrm{cl}}$, are the same

for all PBHs in a given cluster, every PBH in a given cluster generates events of equal duration, $\hat{t}_{\rm cl} = 2R_{\rm E}/v_{\perp,{\rm cl}}$. In each realisation, we calculate the total differential event rate, $\mathrm{d}\Gamma/\mathrm{d}\hat{t}$, by binning the events (weighted by the event rate $\Gamma_{\rm cl}$) according to their durations.

The mean number of events from each cluster is

$$\bar{N}_{\rm cl} = E\epsilon(\hat{t}_{\rm cl})\Gamma_{\rm cl}. \tag{2.26}$$

The number of microlensing events from each cluster, $N_{\rm obs,cl}$, is generated from a Poisson distribution with mean $\bar{N}_{\rm cl}$. The total number of events in each realisation, $N_{\rm obs}$, is the sum of $N_{\rm obs,cl}$ over all clusters.

2.4 Results

2.4.1 Differential event rate

We calculate the differential event rate from 10^4 realisations of each combination of the number of PBHs per cluster, $N_{\rm cl}$, and the PBH mass, $M_{\rm PBH}$, using the approach described in Sec. 2.3.3. When the PBH cluster mass $M_{\rm cl} \lesssim 10^6 M_\odot$ (equivalently, the number of PBH clusters in the microlensing cone $N_{\rm cone} \gtrsim 10^3$), the differential event rate for each realisation has only small stochastic deviations from the smooth DM result. When the cluster mass $M_{\rm cl} \gtrsim 10^6 M_\odot$ (equivalently, the number of clusters in the microlensing cone is $N_{\rm cone} \lesssim 10^3$), most realisations have a deficit of short-duration events, while a small number show a strong excess in the differential event rate at small $\hat{t}$. Fig. 2.1 shows several realisations of the differential event rate, $\mathrm{d}\Gamma/\mathrm{d}\hat{t}$, for clusters containing $N_{\rm cl} = 10^6$ PBHs, for PBHs with masses $M_{\rm PBH} = M_\odot$ and $M_{\rm PBH} = 10M_\odot$, compared to the re-

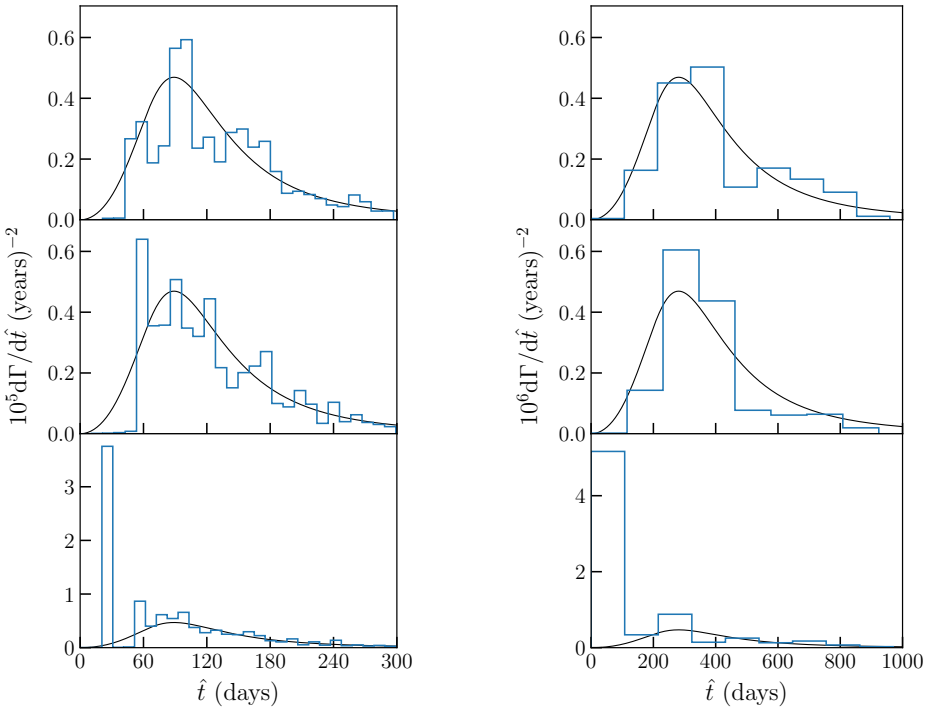

Figure 2.1: *Example realisations of the differential event rate for clustered PBHs (blue lines) and the result for smoothly-distributed DM (black lines). In each realisation, all clusters contain $N_{\rm cl} = 10^6$ PBHs. The PBH mass is $M_{\rm PBH} = M_\odot$ ($M_{\rm PBH} = 10\ M_\odot$) in the left (right) column. The top two rows show 'typical' realisations in which there are no clusters close to the observer, leading to a deficit in short-duration events. The bottom row shows rare realisations in which a cluster close to the observer produces a high rate of short-duration events (notice the different y-axis range shown for these cases).*

sult for smoothly-distributed DM. We show two 'typical' realisations and one 'rare' realisation for each PBH mass.

This behaviour can be understood by considering the dependence of the Einstein radius, $R_{\rm E}$, and the width of the microlensing cone, on x. The rare realisations all include PBH clusters at small x. They are rare because the width of the microlensing cone is proportional to x^2, so the probability of finding a cluster close to the observer is small. Since the Einstein radius (and therefore the event duration) is proportional to $[x(1-x)]^{1/2}$ while the transverse velocity distribution is independent of x (for a Maxwellian

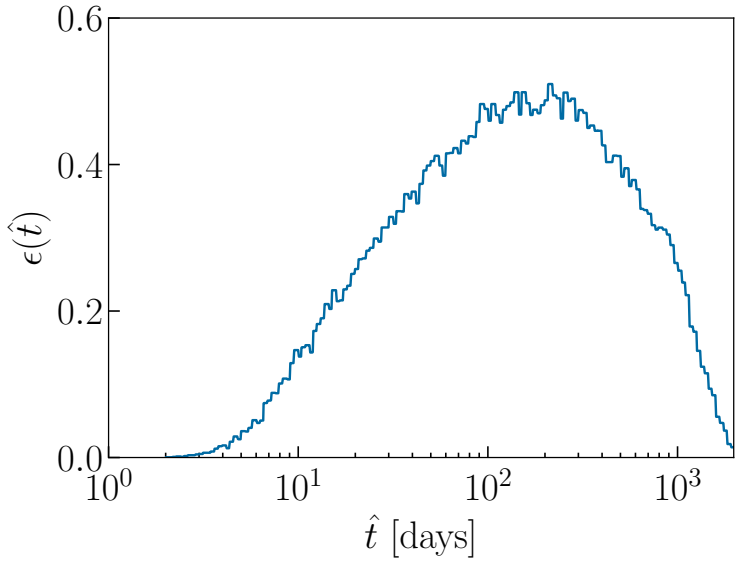

Figure 2.2: *Microlensing detection efficiency for the EROS-2 survey as a function of the Einstein diameter crossing time, $\hat{t}$, for observations towards the Large Magellanic Cloud, as shown in Fig. 11 of Ref. [186]. The efficiency used for calculations in our model survey based on EROS-2 (and the original EROS-2 survey) observing the LMC is the efficiency shown here multiplied by a factor of 0.9 to account for binary lenses.*

velocity distribution), short-duration events are typically caused by clusters at small or large x. The event rate $\Gamma_{\rm cl} \propto R_{\rm E}/x_{\rm cl}^2$, so clusters close to the observer can cause a high rate of microlensing events, giving rise to large peaks in the differential event rate at small $\hat{t}$. Since the Einstein radius increases with the PBH mass, the largest value of $\hat{t}$ for which deviations from the smoothly-distributed DM result appear increases with $M_{\rm PBH}$.

2.4.2 Distribution of number of observed events

We consider the probability distribution of the number of observed events for a given fraction of DM in PBHs, $P[N_{\rm obs}(f)]$, for two model microlensing surveys towards the LMC:

- An EROS-2-like survey, with an exposure $E = 3.77 \times 10^7$ star-years

and efficiency $\epsilon(\hat{t})$ from Fig. 11 of Ref. [186] (reproduced in Fig. 2.2), multiplied by a factor of 0.9 to account for lensing by binary lenses, which detects zero microlensing events.

- A 'toy' survey sensitive to long-duration events, with an exposure $E = 2.5 \times 10^9$ star-years and an efficiency given by $\epsilon(\hat{t}) = 0.4$ for 400 days $< \hat{t} <$ 15 years and $\epsilon(\hat{t}) = 0$ outside this range, which also detects zero microlensing events.

For smoothly-distributed DM, constraints on f from the EROS-2-like survey are within $\sim 10\%$ of those found by the EROS collaboration [126]. For the 'toy' survey, the lower cutoff in the efficiency (at $\hat{t} < 400$ days) corresponds to the cut chosen in Ref. [299] (which combined MACHO and EROS-2 data to produce a survey sensitive to long-duration events) to remove supernovae and short-lived fluctuations in stellar brightness, and the efficiency roughly matches the value obtained in Ref. [299]. The upper cutoff at $\hat{t} = 15$ years approximately matches the value at which the predicted efficiency drops off sharply in a proposed long-duration survey combining data from EROS, MACHO and OGLE [300] [5].

In Fig. 2.3 we show the probability distribution of the number of events in the case that all the DM is in clusters containing $N_{\rm cl}$ PBHs, $P[N_{\rm obs}(f = 1)]$, for PBHs of mass $M_{\rm PBH} = M_\odot$ in the EROS-2-like survey and PBHs of mass $M_{\rm PBH} = 10^3 M_\odot$ in the 'toy' survey. Each distribution is obtained from 10^4 realisations. Our results for the EROS-2-like survey are in very good agreement with Ref. [295], which includes some effects we neglect (the variation of the stellar surface density in the LMC and a density profile of clusters).

[5] The published version of this work (Ref. [301]) incorrectly states that the choice of of exposure approximately corresponds to that from catalogs 2-3 from Ref. [300]. The exposure used is in fact a factor of ≈ 10 larger.

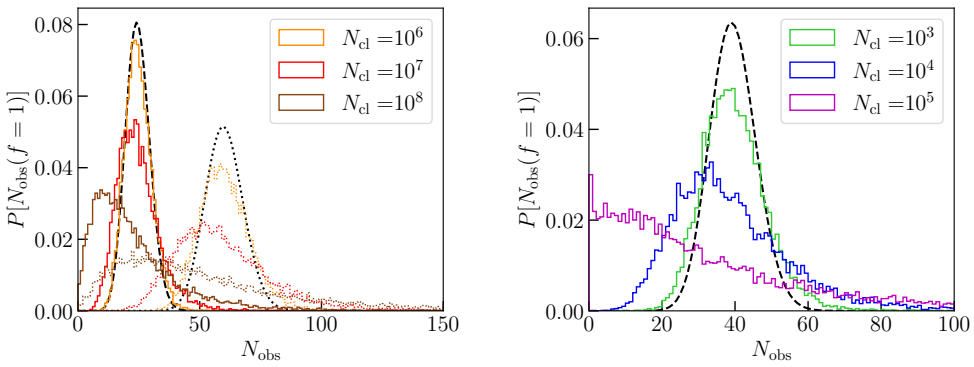

Figure 2.3: *Probability distribution of the number of observed microlensing events, $P[N_{\rm obs}(f=1)]$, assuming all the DM is made of PBHs of mass $M_{\rm PBH}=M_\odot$ (left panel) and $M_{\rm PBH}=10^3 M_\odot$ (right panel).*
Left panel: The orange, red and brown lines are obtained assuming all PBHs are in clusters containing $N_{\rm cl}=10^6, 10^7$ and 10^8 PBHs respectively. Results are shown for the EROS-2 efficiency (solid lines) and assuming perfect detection efficiency $\epsilon(\hat{t})=1$ for all $\hat{t}$ (dotted lines). The distribution for smoothly-distributed DM is Poissonian, with a mean observed number of events $N_{\rm exp}(f=1)=25$ (60), and is shown with a black dashed (dotted) line for the EROS-2 efficiency (perfect efficiency).
Right panel: The green, blue and purple lines are obtained assuming all of the DM is in clusters containing $N_{\rm cl}=10^3, 10^4$ and 10^5 PBHs respectively, for a 'toy' survey sensitive to long-duration events. The black dashed line shows the Poisson distribution for smoothly-distributed DM with mean $N_{\rm exp}(f=1)=40$.

For $M_{\rm cl} \lesssim 10^6 M_\odot$, the distributions $P[N_{\rm obs}(f=1)]$ are close to the Poisson distribution expected for smoothly-distributed DM. For larger $M_{\rm cl}$, the distribution deviates from Poissonian, with a peak at smaller numbers of events and a long tail out to large numbers of events. The deviation from a Poisson distribution is relatively small for $M_{\rm cl} \sim 10^6 M_\odot$ and becomes more significant for larger cluster masses. This behaviour arises from the deviation in the differential event rate from the smoothly-distributed DM result at short event durations. For $M_{\rm cl} \gtrsim 10^6 M_\odot$, most realisations of the differential event rate have a deficit of short-duration events, resulting in fewer microlensing events compared to smoothly-distributed DM. Therefore $P[N_{\rm obs}(f=1)]$ peaks at smaller numbers of events. The rare realisations with a cluster at small x generate a high rate of microlensing events, giving

rise to the long tails out to large numbers of events. In the left hand panel of Fig. 2.3, we have also presented the results using the exposure from EROS-2 but with perfect detection efficiency ($\epsilon(\hat{t}) = 1$ for all $\hat{t}$). The deviation from a Poisson distribution is more pronounced when using perfect efficiency than when using the EROS-2 efficiency from Ref. [186]. This is because the EROS-2 efficiency is largest for events of duration $\hat{t} \approx 200\,\text{days}$, while for Solar-mass PBHs the impact of clustering on the differential event rate is most apparent at smaller values of $\hat{t}$ where the efficiency is lower.

2.4.3 Constraints on the PBH abundance

Since both model surveys detect zero events, a 95% exclusion limit on the fraction of DM in PBHs, f, can be obtained by finding f such that $P[N_{\rm obs}(f) = 0] = 0.05$. For smoothly-distributed DM, $P[N_{\rm obs}(f)]$ is Poissonian, in which case

$$P[N_{\rm obs}(f) = 0] = \exp\left(-N_{\rm exp}(f)\right), \tag{2.27}$$

where $N_{\rm exp}(f)$ is the mean number of expected events for a fraction of DM in PBHs f. Since the differential event rate (Eq. (2.16)) is proportional to the local DM density, ρ_0, the expected number of events (Eq. (2.17)) is proportional to f, so $N_{\rm exp}(f) = fN_{\rm exp}(f = 1)$. Here, $N_{\rm exp}(f = 1)$ is the number of events expected if all of DM is in PBHs, given by Eq. (2.17). Requiring $P[N_{\rm obs}(f) = 0] = 0.05$ gives a 95% exclusion limit $f < 3.0/N_{\rm exp}(f = 1)$ [302]. For clustered DM, $P[N_{\rm obs}(f)]$ deviates from a Poisson distribution when $M_{\rm cl} \gtrsim 10^6 M_\odot$. To calculate the 95% exclusion limit in this case, one must explicitly calculate $P[N_{\rm obs}(f)]$ for a range of f values to find the value of f for which $P[N_{\rm obs}(f) = 0] = 0.05$.

For the EROS-2-like survey, assuming all PBHs are found in clusters containing $N_{\rm cl} = 10^3$ PBHs, the change in f from the smoothly-distributed DM result is negligible over the entire PBH mass range constrained by this survey. This is because the differential event rate closely approximates that found for smoothly-distributed DM, so $P[N_{\rm obs}(f)]$ is very close to Poissonian. To significantly weaken constraints on f, $N_{\rm cl}$ would need to be several orders of magnitude larger than what is expected for PBHs formed from the collapse of large gaussian density fluctuations.

Since the most common cluster size today is expected to be $N_{\rm cl} \sim 10^3$, the deviation of $P[N_{\rm obs}(f)]$ from a Poisson distribution is only non-negligible for $M_{\rm PBH} \gtrsim 10^3 M_\odot$, a mass range that is probed by the 'toy' survey. We use Monte Carlo simulations to find the 95% exclusion limit on f in the 'toy' survey for $M_{\rm PBH} = 10^3 M_\odot$ (approximately the largest PBH mass constrained in by the long-duration survey in Ref. [299]) and $N_{\rm cl} = 10^3$. We find a 95% exclusion limit $f < 0.096$, compared to $f < 0.076$ for smoothly-distributed DM.

2.5 Conclusions

We have considered the effect of PBH clustering, for PBHs formed from the collapse of large gaussian density fluctuations generated by inflation, on constraints from stellar microlensing of stars in the LMC. In this PBH formation scenario, PBHs within clusters are well-separated and therefore act as independent lenses. We expect PBH clusters containing $N_{\rm cl} \sim 10^3$ PBHs to be most abundant, since smaller clusters will have evaporated and larger clusters form much more rarely. We have assumed every PBH has the same mass and that all are found in clusters containing a fixed number

of PBHs. A significant fraction of PBHs are expected to be unclustered, so our results are an upper limit on the effects of clustering on LMC stellar microlensing constraints.

When the total cluster mass $M_{\rm cl} \lesssim 10^6 M_\odot$, the differential event rate and therefore the probability distribution for the total number of events is very close to that found for smoothly-distributed DM, so clustering has a negligible effect on constraints. When the cluster mass $M_{\rm cl} \gtrsim 10^6 M_\odot$, the differential event rate deviates from that found for smoothly-distributed DM. The probability of a cluster being close to the observer is small, so most realisations of the differential event rate have a deficit of short-duration events compared to the result for smoothly-distributed DM (see the top two rows of Fig. 2.1). Rare realisations feature clusters close to the observer, which can produce a high rate of short-duration events (see the bottom row of Fig. 2.1).

As shown in Fig. 2.3, the probability distribution for the total number of events therefore deviates from the Poisson distribution that arises for smoothly-distributed DM. Compared to the Poisson distribution, the distribution for clustered PBHs peaks at smaller numbers of events due to the deficit of short-duration events in most realisations of the differential event rate, while rare realisations with an excess of short-duration events give rise to a long tail in the probability distribution up to large numbers of events.

Since we expect clusters containing $N_{\rm cl} \sim 10^3$ PBHs to be the most abundant, the effect of clustering is only non-negligible for PBHs of mass $M_{\rm PBH} \gtrsim 10^3 M_\odot$. At the time this work was completed, the only microlensing constraints in this mass range were from the long-duration survey performed in Ref. [299], which ruled out $f = 1$ for $10 M_\odot \lesssim M_{\rm PBH} \lesssim 10^3 M_\odot$ (where

f is the fraction of DM in PBHs). By considering a model microlensing survey sensitive to long-duration events, we find that, for $M_{\rm PBH} = 10^3 M_\odot$, the weakening of constraints on f is only of order 10%, even if all PBHs are in clusters. For clustering to significantly affect stellar microlensing constraints (for $M_{\rm PBH} \lesssim 10^3 M_\odot$) therefore requires conditions not expected for PBHs formed from the collapse of large gaussian density fluctuations: either PBH clusters contain $N_{\rm cl} \gg 10^3$ PBHs or the clusters are compact so the whole cluster acts as a single lens. Since this work was completed, Ref. [303] has shown that clusters of stellar-mass PBHs that are sufficiently compact or sufficiently massive to evade microlensing constraints are constrained by Lyman-α observations, so stellar-mass PBHs cannot make up a dominant fraction of the DM.

Chapter 3

How open is the asteroid-mass window?

3.1 Introduction

Typically observational constraints on PBHs are calculated assuming that PBHs have a delta-function mass function (MF). However, PBHs formed from the collapse of large density perturbations are expected to have an extended mass function (see Sec. 1.4.2). Due to critical collapse, the mass of a PBH depends on both the horizon mass and the amplitude of the density fluctuation from which it forms. Consequently even if PBHs all form at the same time, from a narrow peak in the primordial power spectrum, they have a range of masses [123–125]. Furthermore, the peaks in the primordial power spectrum that are produced by concrete inflation models, for instance hybrid inflation with a mild waterfall transition [145] (see Sec. 1.4.3), can be broad.

With an extended PBH MF the constraints are 'smeared out'; for each

constraint the tightest limit on the fraction of DM in the form of PBHs, $f_{\rm PBH}$, is weakened, however the range of peak masses [1] for which $f_{\rm PBH} = 1$ is excluded is wider [126, 287, 288]. Refs. [126, 287, 288] calculated constraints on PBHs with a lognormal MF, which provides a reasonable fit to the MFs found for PBHs produced by various inflation models [126, 127]. However, Gow et al. [128] found that the MFs they calculate are better fit by other functions, specifically a skew-lognormal distribution and a form motivated by critical collapse. As Gow et al. [128] mention, the shape of the low mass tail is important when considering evaporation constraints on PBHs with MFs which peak in the asteroid-mass window. It is important to ascertain how the extent to which the asteroid-mass window remains open (i.e. for what range of peak masses $f_{\rm PBH} = 1$ is allowed) depends on the shape of the PBH MF.

We recalculate constraints on $f_{\rm PBH}$ in the asteroid-mass window for the MF fitting functions presented in Ref. [128]. Sec. 3.2 presents the constraints we consider, the fits to the PBH MF that we use and their time evolution, and the method for applying the constraints to extended mass functions. We present the current and prospective future constraints on PBHs with extended MFs in Sec. 3.3 and conclude with discussion in Sec. 3.4.

3.2 Method

In Sec. 3.2.1 we overview the (current and proposed future) evaporation and stellar microlensing constraints that we use. In Sec. 3.2.2 we overview the best-performing MF fitting functions from Ref. [128] and the evolution of the MF due to evaporation, and in Sec. 3.2.3 we outline how the constraints

[1] Here and throughout this chapter peak mass refers to the mass at which the mass function is maximal.

are applied to extended mass functions.

3.2.1 Constraints on PBHs around the asteroid-mass window

As discussed in Sec. 3.2.1, the constraints on PBHs with masses $M_{\rm PBH} \lesssim 10^{17}\,{\rm g}$ and $M_{\rm PBH} \gtrsim 10^{22}\,{\rm g}$ arise from PBH evaporation via Hawking radiation (Sec. 3.2.1) and stellar microlensing (Sec. 3.2.1) respectively. The constraints that we consider (both existing and prospective) are shown in Fig. 3.1 for a delta-function PBH MF.

PBH evaporation

PBHs formed from the collapse of large density perturbations rapidly lose angular momentum and charge [86, 304]. Hawking [84, 85] showed that a non-rotating, uncharged black hole (BH) of mass $M_{\rm BH}$ radiates with a temperature

$$T_{\rm BH} = \frac{1}{8\pi G M_{\rm BH}} = 1.06 \left(\frac{M_{\rm BH}}{10^{16}\,{\rm g}}\right)^{-1} {\rm MeV}. \tag{3.1}$$

As a result of Hawking radiation, in the absence of accretion or mergers, the mass of a BH decreases at a rate [85, 86]

$$\frac{{\rm d}M_{\rm BH}}{{\rm d}t} = -\frac{1}{G^2}\frac{\alpha(M_{\rm BH})}{M_{\rm BH}^2}, \tag{3.2}$$

where $\alpha(M_{\rm BH})$ parameterizes the number of particle species which can be emitted at a significant rate from a BH of mass $M_{\rm BH}$. BHs with mass $M_{\rm BH} \gg 10^{17}\,{\rm g}$ can only emit photons and neutrinos, while those with smaller masses (and higher temperatures) can emit other particle species,

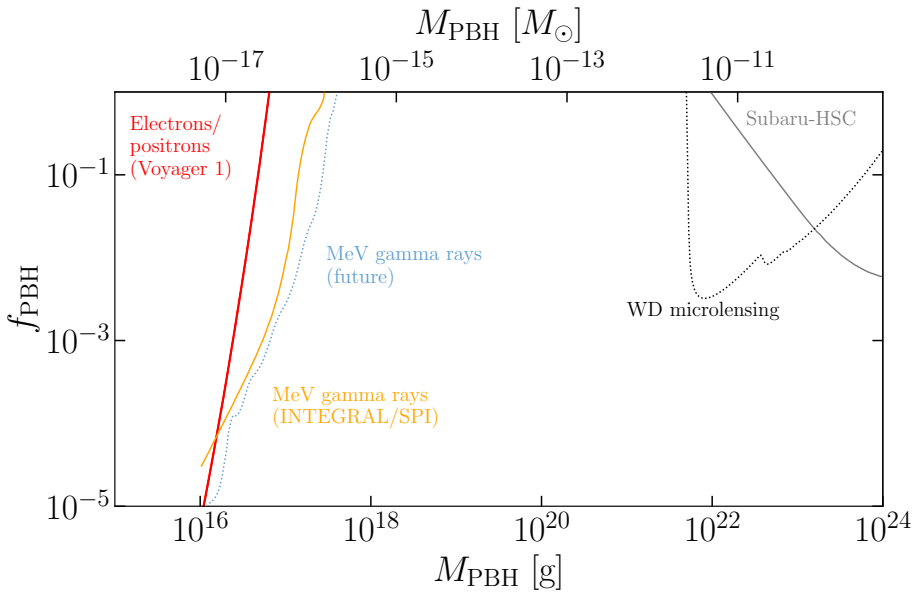

Figure 3.1: *The constraints we use on the fraction of dark matter in PBHs, $f_{\rm PBH}$, as a function of the PBH mass, $M_{\rm PBH}$, assuming a delta-function PBH mass function. Current constraints are shown as solid lines and prospective future constraints as dotted lines. The current evaporation constraints are from Voyager 1 measurements of the local flux of electrons and positrons [159] (red) and INTEGRAL/SPI observations of MeV gamma rays [160] (orange). The current stellar microlensing constraints in this mass range are from Subaru-HSC [183], as calculated in Ref. [306] (grey). The prospective future evaporation constraints are from a MeV gamma-ray telescope [307] (light blue) while the microlensing constraints are for a LMC white dwarf survey [308] (black).*

such as electrons and positrons [86, 305]. Unstable particles emitted by PBHs decay to stable secondary particles, such as photons and electrons. The total emission of a given species from a PBH is the combination of the primary (i.e. directly emitted) and secondary components. As a result of Hawking evaporation, the PBH mass changes with time and PBHs have a finite lifetime. Since the PBH mass is time-dependent, the PBH mass function (MF) also evolves with time (see Sec. 3.2.2).

As discussed in Sec. 1.4.5, there are various evaporation constraints, from different particle species and observations, calculated using different assumptions, with different uncertainties. We consider two illustrative constraints: the INTEGRAL/SPI MeV gamma-ray limits from Ref. [160] which tightly constrain $f_{\rm PBH}$ (for a delta-function MF) for $10^{16}\,{\rm g} \lesssim M_{\rm PBH} \lesssim$

10^{17} g, and the Voyager 1 $e^{\pm}$ limits from Ref. [159] which tightly constrain $f_{\rm PBH}$ for $M_{\rm PBH} \lesssim 10^{16}$ g. As we will see in Sec. 3.3, the constraint that rules out $f_{\rm PBH} = 1$ for the largest value of $M_{\rm PBH}$ doesn't necessarily exclude $f_{\rm PBH} = 1$ for the largest peak mass for broad, extended MFs.

Ref. [160] calculates constraints from gamma rays produced by positrons from PBH evaporation annihilating with electrons in the interstellar medium, including the contribution from positrons that first form a positronium bound state. We use the constraint (shown with a dashed purple line in Fig. 1 of Ref. [160]) obtained using the INTEGRAL/SPI limit on the flux of MeV gamma rays from a component with a Navarro-Frenk-White (NFW) density profile (see Sec. 1.2.2) from Ref. [181]. We use the Voyager 1 $e^{\pm}$ constraint in the left panel of Fig. 2 of Ref. [159] with astrophysical background subtraction for their propagation model A, which has strong diffusive reacceleration.

Proposed future MeV gamma-ray telescopes have the potential to place tighter constraints on evaporating PBHs, extending the range of masses where $f_{\rm PBH} = 1$ is excluded to larger $M_{\rm PBH}$. As an illustrative case we consider the projected constraints from observations towards the Galactic Centre (assuming a NFW profile) by the proposed GECCO telescope from Fig. 9 of Ref. [307] [2].

Microlensing

As discussed in Sec. 1.4.5 and Sec. 2.3, stellar microlensing is the temporary amplification of a background star that occurs when a compact object passes close to the line of sight to the star [182]. Observations of stars in

[2]The proposed AMEGO telescope would be able to exclude $f_{\rm PBH} = 1$ to somewhat larger $M_{\rm PBH}$ [309, 310].

M31 by Subaru-HSC [183] have been used to constrain $f_{\rm PBH}$ in the mass range $10^{22}\,{\rm g} \lesssim M_{\rm PBH} \lesssim 10^{28}\,{\rm g}$ [183, 306].

Accounting for the finite size of the source stars weakens the constraints significantly from those calculated assuming a point-like source [273, 311]. Additionally, for PBHs with masses $M_{\rm PBH} \lesssim 10^{-11} M_\odot \sim 10^{22}\,{\rm g}$, the Schwarzschild radius of the PBHs is comparable to the wavelength of the light used to observe the stars, resulting in diffraction and interference effects. Due to these 'wave optics' effects, it is not possible to constrain PBHs with $M_{\rm PBH} \lesssim 10^{-11} M_\odot \sim 10^{22}\,{\rm g}$ using microlensing surveys of main-sequence stars [273, 308]. We use the point-like lens constraint from Fig. 4 of Ref. [306].

To minimise the finite source and wave optics effects, Ref. [308] suggests a survey of white dwarfs in the Large Magellanic Cloud (LMC) using shorter wavelength observations. They find such a survey could place significantly tighter constraints on PBHs with mass $M_{\rm PBH} \sim 10^{(22-23)}\,{\rm g}$. We use the constraint from Fig. 8 of Ref. [308] that accounts for both finite source and wave optics effects.

3.2.2 PBH mass functions and evolution

Initial mass functions

The initial PBH mass function (MF) can be defined as

$$\psi(M_{\rm PBH,\,i}, t_{\rm i}) \equiv \frac{1}{\rho_{\rm i}} \frac{{\rm d}\rho(M_{\rm PBH,\,i}, t_{\rm i})}{{\rm d}M_{\rm PBH,\,i}}\,, \tag{3.3}$$

where $\rho(M_{\rm PBH,\,i}, t_{\rm i})$ is the comoving mass density in PBHs of initial mass $M_{\rm PBH,\,i}$ at the time they form, $t_{\rm i}$, and $\rho_{\rm i}$ is the initial total comoving mass

density of PBHs.

As discussed in Sec. 1.4.2, due to near-critical gravitational collapse [122], PBHs will have a range of masses even if all PBHs form at the same time, i.e. from a delta-function peak in the primordial power spectrum [123–125]. In this case the critical collapse (CC) initial MF is well approximated, assuming the probability distribution of the amplitude of the fluctuations is gaussian, by

$$\psi_{\rm CC}(M_{\rm PBH,\,i}, t_{\rm i}) = \frac{1}{\gamma M_{\rm p} \Gamma\left(\gamma+1\right)} \left(\frac{M_{\rm PBH,\,i}}{M_{\rm p}}\right)^{1/\gamma} \times \exp\left[-\left(\frac{M_{\rm PBH,\,i}}{M_{\rm p}}\right)^{1/\gamma}\right], \tag{3.4}$$

where $M_{\rm p}$ is the mass at which the MF peaks and Γ is the gamma function.

In reality the primordial power spectrum will have finite width, and PBHs will form on a range of scales. For various inflation models the MFs calculated, taking critical collapse into account, can be roughly approximated by a lognormal (LN) distribution [126, 127]:

$$\psi_{\rm LN}(M_{\rm PBH,\,i}, t_{\rm i}) = \frac{1}{\sqrt{2\pi}\sigma M_{\rm PBH,\,i}} \exp\left(-\frac{\ln^2(M_{\rm PBH,\,i}/M_{\rm c})}{2\sigma^2}\right), \tag{3.5}$$

where σ is the width and $M_{\rm c}$ is the mean of $M_{\rm PBH,\,i}\psi_{\rm LN}(M_{\rm PBH,\,i}, t_{\rm i})$. The lognormal MF has been widely adopted as the canonical extended PBH MF (for instance when applying observational constraints to extended mass functions [287, 288]).

Gow et al. [128] investigated more accurate fitting functions for the initial MF of PBHs formed from a symmetric peak in the primordial power spectrum. They parameterise the peak in the power spectrum of the curvature

perturbation, $\mathcal{P}_\zeta(k)$, as lognormal,

$$\mathcal{P}_\zeta(k) = A\frac{1}{\sqrt{2\pi}\Delta}\exp\left(-\frac{\ln^2(k/k_\mathrm{p})}{2\Delta^2}\right), \tag{3.6}$$

where A and Δ are the amplitude and width of the peak and k_p is the comoving wavenumber at which it occurs. We have found that the broad peak in the primordial power spectrum produced by hybrid inflation with a mild waterfall transition [145] (see Sec. 1.4.3) is fairly well-approximated by a lognormal with $\Delta \sim 5$. Ref. [128] calculates the PBH MF numerically as in Ref. [129], using the traditional (BBKS) peaks theory method [119] with a modified gaussian window function [3].

Gow et al. [128, 129] find that for narrow peaks in the power spectrum, $\Delta \lesssim 0.3$, critical collapse dominates the PBH MF; the MF is independent of the width of the power spectrum and skewed towards low masses. For $\Delta \gtrsim 0.5$ the width of the peak becomes important. As Δ is increased the width of the MF increases and the skew towards low masses decreases, and for large Δ (the transition occurs between $\Delta = 2$ and 5) their MFs are skewed towards large masses [128]. Of the fitting functions considered in Ref. [128], the two that best reproduce this behaviour are the skew-lognormal and generalised critical collapse functions. The skew-lognormal (SLN) MF is a generalisation of the lognormal with non-zero skewness:

$$\begin{aligned}\psi_\mathrm{SLN}(M_{\mathrm{PBH,i}}, t_\mathrm{i}) = \frac{1}{\sqrt{2\pi}\sigma M_{\mathrm{PBH,i}}}\exp\left(-\frac{\ln^2(M_{\mathrm{PBH,i}}/M_\mathrm{c})}{2\sigma^2}\right) \\ \times\left[1+\mathrm{erf}\left(\alpha\frac{\ln(M_{\mathrm{PBH,i}}/M_\mathrm{c})}{\sqrt{2}\sigma}\right)\right],\end{aligned} \tag{3.7}$$

[3] More recently Germani and Sheth [312] have formulated a procedure for calculating the abundance and MF of PBHs, using the statistics of the compaction function (see Sec. 1.4.2). They find (assuming a gaussian distribution for the perturbations) that the low mass tail of the MF is generically (i.e. for any primordial power spectrum) a power law, $\psi(M_{\mathrm{PBH,i}}, t_\mathrm{i}) \propto M_{\mathrm{PBH,i}}^{1/\gamma}$, while at large masses there is a cut off, which depends on the shape and amplitude of the power spectrum.

where α controls the skewness of the MF; for negative (positive) α the MF is skewed to low (high) masses [4]. The generalised critical collapse (GCC) MF [5] is given by

$$\psi_{\rm GCC}(M_{\rm PBH,i}, t_{\rm i}) = \frac{\beta}{M_{\rm p}} \left[\Gamma\left(\frac{\alpha+1}{\beta}\right)\right]^{-1} \left(\frac{\alpha}{\beta}\right)^{\frac{\alpha+1}{\beta}} \left(\frac{M_{\rm PBH,i}}{M_{\rm p}}\right)^{\alpha} \times \exp\left[-\frac{\alpha}{\beta}\left(\frac{M_{\rm PBH,i}}{M_{\rm p}}\right)^{\beta}\right], \tag{3.8}$$

where $M_{\rm p}$ is the mass at which the generalised critical collapse MF peaks, and α and β are parameters that control its behaviour in the low and high-mass tails respectively (for $M_{\rm PBH,i} \ll M_{\rm p}$, $\psi_{\rm GCC}(M_{\rm PBH,i}, t_{\rm i}) \propto M^{\alpha}_{\rm PBH,i}$). The generalised critical collapse MF is a generalisation of the critical collapse MF obtained assuming all PBHs form at the same time, Eq. (3.4), which corresponds to Eq. (3.8) with $\alpha = \beta = 1/\gamma$ [124]. Gow et al. [128] find that the generalised critical collapse MF is a better fit to their calculated MFs than the skew-lognormal for narrow peaks ($\Delta \lesssim 0.5$) where critical collapse dominates the PBH MF and it has negative skew, while for broad peaks ($\Delta \gtrsim 5$) the skew-lognormal is a better fit.

Ref. [128] focuses on stellar-mass PBHs. For the three fitting functions we consider (lognormal, skew-lognormal and generalised critical collapse), we choose values for the mass parameters ($M_{\rm c}$ or $M_{\rm p}$) in the asteroid-mass window. For the parameters which govern the shape of the MF (α, β and σ), we adopt the best-fit parameter values in Table II of Ref. [128] [6], i.e. for simplicity we assume that these parameters do not depend on the PBH mass, or equivalently the position of the peak in the primordial power

[4] For consistency we use the same notation for the parameters of the fitting functions as Gow et al. [128], however the α parameters in the skew-lognormal and generalised critical collapse fitting functions affect their shapes in different ways.

[5] In Ref. [128], this is referred to as the 'CC3' model.

[6] Table II of Ref. [128] contains the best-fit parameter values for the skew-lognormal and generalised critical collapse MFs, we are grateful to Andrew Gow for providing those for the lognormal MF via email.

spectrum, k_p. To facilitate comparison between the constraints obtained with different fitting functions, we present the constraints for the lognormal and skew-lognormal MF in terms of the peak mass, i.e. the mass at which the MF is maximal, M_p. For the lognormal, $M_\mathrm{p} = M_\mathrm{c}\exp(-\sigma^2)$, while for the skew-lognormal there is no analytic expression for M_p.

Time evolution of the mass function

The MFs presented in Sec. 3.2.2 are fits to the initial MFs calculated in Ref. [128]. For PBHs with initial mass $M_{\mathrm{PBH,\,i}} \lesssim 1\times10^{15}\,\mathrm{g}$, Hawking evaporation leads to significant ($>10\%$) mass loss by the present day, and hence the MF varies with time [163, 313–315]. Therefore for extended MFs that are peaked at sufficiently small M_p and/or are sufficiently broad that there is a significant abundance of PBHs with initial masses $M_{\mathrm{PBH,\,i}} \lesssim 1\times10^{15}$ g, the time evolution of the MF should be taken into account.

To evaluate the PBH mass today at time $t = t_0$, we follow Ref. [315] (see also Ref. [316]) and approximate $\alpha(M_\mathrm{PBH})$ as depending only on the initial mass, $\alpha(M_\mathrm{PBH}) \approx \alpha_\mathrm{eff}(M_{\mathrm{PBH,\,i}})$. Integrating Eq. (3.2), the PBH mass today, $M_\mathrm{PBH}(t_0)$, can be expressed as

$$M_\mathrm{PBH}(t_0) \approx \left(M_{\mathrm{PBH,\,i}}^3 - \frac{3\alpha_\mathrm{eff}(M_{\mathrm{PBH,\,i}})t_0}{G^2}\right)^{1/3}, \tag{3.9}$$

where the formation time, t_i, has been set to zero since $t_0 \gg t_\mathrm{i}$. Here, $\alpha_\mathrm{eff}(M_{\mathrm{PBH,\,i}})$ is defined as

$$\alpha_\mathrm{eff}(M_{\mathrm{PBH,\,i}}) \equiv \frac{G^2 M_{\mathrm{PBH,\,i}}^3}{3\tau_\mathrm{i}}, \tag{3.10}$$

where τ_i is the PBH lifetime (which can be calculated numerically e.g. using `BlackHawk` [317, 318]). This definition ensures that the PBH lifetime is

calculated accurately for all initial masses $M_{\mathrm{PBH,\,i}}$.

Using the conservation of the number of PBHs, the PBH MF today, $\psi(M_{\mathrm{PBH}}, t_0)$, defined as

$$\psi(M_{\mathrm{PBH}}, t_0) \equiv \frac{1}{\rho_{\mathrm{i}}} \frac{\mathrm{d}\rho(M_{\mathrm{PBH}}, t_0)}{\mathrm{d}M_{\mathrm{PBH}}}\,, \tag{3.11}$$

where $\rho(M_{\mathrm{PBH}}, t_0)$ is the comoving mass density in PBHs with present day mass M_{PBH}, can be expressed in terms of the initial PBH MF, $\psi(M_{\mathrm{PBH,\,i}}, t_{\mathrm{i}})$, defined in Eq. (3.3), as [163, 169, 315, 319]

$$\psi(M_{\mathrm{PBH}}, t_0) = \left(\frac{M_{\mathrm{PBH}}}{M_{\mathrm{PBH,\,i}}}\right)^3 \psi(M_{\mathrm{PBH,\,i}}, t_{\mathrm{i}}). \tag{3.12}$$

The equivalent expression in Ref. [315] contains a factor that can be written as $(M_{\mathrm{PBH}}/M_{\mathrm{PBH,\,i}})$ squared, rather than cubed, since they are considering number, rather than mass, densities.

3.2.3 Calculating constraints for extended MFs

We use the method introduced in Ref. [287] to apply constraints to extended MFs (a similar method is presented in Ref. [289]). The constraint on the fraction of dark matter in PBHs can be expressed as [287]

$$f_{\mathrm{PBH}} \leq \left[\int \mathrm{d}M_{\mathrm{PBH}} \frac{\psi_{\mathrm{N}}(M_{\mathrm{PBH}}, t_0)}{f_{\mathrm{max}}(M_{\mathrm{PBH}})}\right]^{-1}, \tag{3.13}$$

where $f_{\mathrm{max}}(M_{\mathrm{PBH}})$ is the maximum fraction of dark matter in PBHs allowed for a delta-function MF, and $\psi_{\mathrm{N}}(M_{\mathrm{PBH}}, t_0)$ is defined as

$$\psi_{\mathrm{N}}(M_{\mathrm{PBH}}, t_0) \equiv \frac{1}{\rho(t_0)} \frac{\mathrm{d}\rho(M_{\mathrm{PBH}}, t_0)}{\mathrm{d}M_{\mathrm{PBH}}}, \tag{3.14}$$

where $\rho(t_0)$ is the total comoving mass density in PBHs today. This definition of the MF is normalised to unity today $\int \mathrm{d}M_{\rm PBH}\psi_{\rm N}(M_{\rm PBH}, t_0) = 1$, while the MF $\psi(M_{\rm PBH}, t_0)$ defined in Eq. (3.11) in Sec. 3.2.2 is not, since the total mass in PBHs decreases with time due to evaporation. As discussed in Sec. 3.2.2 PBHs with initial mass $M_{\rm PBH,\,i} \lesssim 1 \times 10^{15}\,\mathrm{g}$ lose a non-negligible fraction of their mass by the present day. Therefore for the evaporation constraints the MF should be evolved to the present day using Eq. (3.12) before calculating $\psi_{\rm N}(M_{\rm PBH}, t_0)$ by renormalizing to the present day PBH mass density.

For the evaporation constraints $f_{\rm max}(M_{\rm PBH})$ decreases rapidly with decreasing $M_{\rm PBH}$, as the Hawking temperature is inversely proportional to the mass, Eq. (3.1). Consequently, for sufficiently wide MFs peaked at the lower end of the asteroid-mass range, the contribution to Eq. (3.13) from $f_{\rm max}(M_{\rm PBH})$ at smaller masses than the constraints are publicly available for ($M_{\rm PBH} \lesssim 10^{15}\,\mathrm{g}$ for the Voyager 1 constraints [159] and $M_{\rm PBH} < 10^{16}\,\mathrm{g}$ for the INTEGRAL/SPI MeV gamma-ray constraints [160]) may be important. At the smallest masses where constraints are publicly available, $f_{\rm max}(M_{\rm PBH}) \propto M_{\rm PBH}^q$ with $q \approx 2 - 3$ to a good approximation, and we assume that the power-law form, $f_{\rm max}(M_{\rm PBH}) \propto M_{\rm PBH}^q$, continues to smaller masses. We have checked that the resulting extended MF constraints do not change significantly (by no more than a factor of a few at peak masses where $f_{\rm PBH} \sim 1$) if instead $f_{\rm max}(M_{\rm PBH})$ becomes constant at small masses.

3.3 Results

In this section we calculate the constraints on the time-evolved lognormal, skew-lognormal, and generalised critical collapse PBH mass functions pre-

sented in Sec. 3.2.2, for the constraints reviewed in Sec. 3.2.1 using the method presented in Sec. 3.2.3. We do this first for the existing limits in Sec. 3.3.1, and then for the future prospective limits in Sec. 3.3.2. We discuss the apparent differences in our results from previous constraints obtained using a lognormal mass function in Sec. 3.3.3.

3.3.1 Existing constraints

Fig. 3.2 shows current constraints on the fraction of DM in PBHs, $f_{\rm PBH}$, for the fitting functions presented in Sec. 3.2.2 for PBHs arising from a log-normal peak in the power spectrum, Eq. (3.6), with width $\Delta = 0, 2$ and 5 ($\Delta = 0$ corresponds to a delta-function peak). These values span the range of values considered by Ref. [128]. As discussed in Sec. 3.2.1, the constraints we consider are from INTEGRAL/SPI observations of MeV gamma rays [160], Voyager 1 measurements of the local flux of electrons and positrons [159], and the Subaru-HSC microlensing survey [183] as calculated in Ref. [306].

As previously seen in e.g. Refs. [156, 287], compared to the delta-function MF constraints, the tightest extended MF constraint is weakened, while $f_{\rm PBH} = 1$ is excluded over a wider range of peak masses $M_{\rm p}$. As anticipated in Ref. [128], the constraints depend on the shape of the low and high mass tails of the MF. Nevertheless, even for the widest power spectrum considered, $\Delta = 5$, there remains a range of peak masses for which $f_{\rm PBH} = 1$ is allowed for all three extended mass functions. Our evaporation constraints for extended MFs appear closer to the delta-function MF constraints than previously found for the lognormal MF (see e.g. Fig. 20 of Ref. [156]). As we discuss in Sec. 3.3.3, this is largely an artefact of the lognormal MF constraints previously being plotted in terms of the parame-

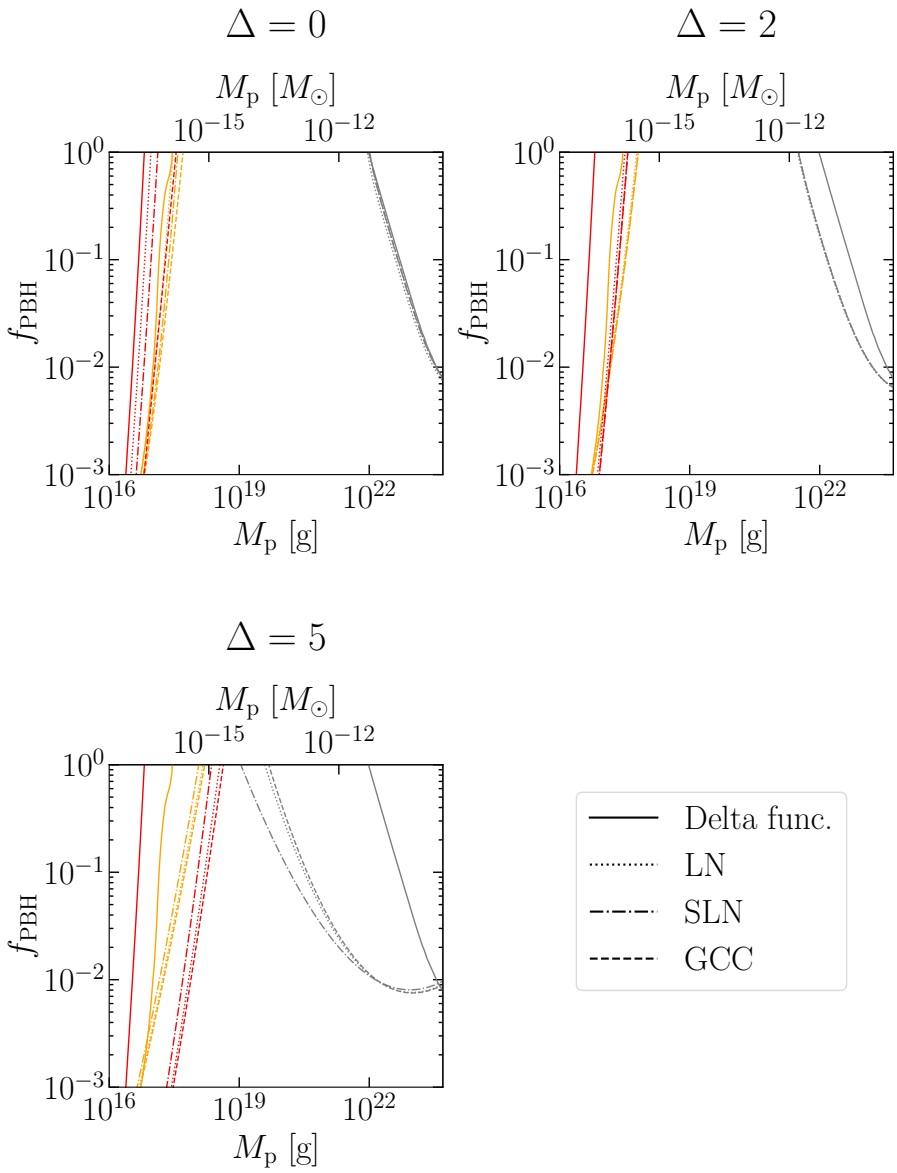

Figure 3.2: *Current constraints on the fraction of dark matter in PBHs, $f_{\rm PBH}$, as a function of the mass at which the PBH MF peaks, $M_{\rm p}$, for PBHs formed from a lognormal peak in the primordial power spectrum, Eq. (3.6), with width $\Delta = 0$ (top left), $\Delta = 2$ (top right) and $\Delta = 5$ (bottom left). Constraints for the lognormal (LN), skew-lognormal (SLN) and generalised critical collapse (GCC) MFs are shown with dotted, dot-dashed, and dashed lines respectively, while the original constraints, calculated assuming a delta-function MF are shown with solid lines. The constraints shown are from Voyager 1 measurements of the local flux of electrons and positrons [159] (red), INTEGRAL/SPI observations of MeV gamma rays [160] (orange), and the Subaru-HSC microlensing survey [183] as calculated in Ref. [306] (grey). In the $\Delta = 2$ case, the constraints for the skew-lognormal and generalised critical collapse MFs are indistinguishable.*

ter $M_{\rm c}$ which appears in the definition of the lognormal MF (see Eq. (3.5)) rather than the peak mass, $M_{\rm p}$.

For small Δ the MFs calculated in Ref. [128] are skewed towards low masses and the best-fit lognormal underestimates the low-mass tail and overestimates the fhigh-mass tail. At a given $M_{\rm p}$, the evaporation and microlensing constraints for a lognormal MF are therefore less and slightly more stringent, respectively, than those for the better fitting skew-lognormal and generalised critical collapse MFs. For $\Delta = 0$, the Voyager 1 constraint for the generalised critical collapse MF (the best-performing function for $\Delta \lesssim 0.5$ [128]) at a given $M_{\rm p}$ is more stringent than the constraints for the lognormal and skew-lognormal MFs by an order of magnitude or more. This is because the power-law tail of the generalised critical collapse MF at low masses is much larger than the low-mass tails of the lognormal and skew-lognormal MFs, and the constraint from Voyager 1 is especially tight at low $M_{\rm PBH}$. The INTEGRAL/SPI MeV gamma-ray constraints for the different extended MFs are more similar, as this constraint is relatively weak for the range of $M_{\rm PBH}$ where the differences between the MFs are large. Since the microlensing constraints for each MF agree closely, and the extended MF constraints from INTEGRAL/SPI observations of MeV gamma rays are more stringent than those from Voyager 1, the range of $M_{\rm p}$ where $f_{\rm PBH} = 1$ is allowed is fairly similar for each MF. For $\Delta = 0$, for the best fitting generalised critical collapse MF, $f_{\rm PBH} = 1$ is allowed for $5 \times 10^{17}\,{\rm g} \lesssim M_{\rm p} \lesssim 1 \times 10^{22}\,{\rm g}$, a slightly narrower mass range than for the lognormal MF.

For $\Delta = 2$, the MF calculated in Ref. [128] is close to symmetric, and all three MFs provide a very good fit [128]. Therefore the constraints for the extended MFs are very similar, with $f_{\rm PBH} = 1$ being allowed for $6 \times 10^{17}\,{\rm g} \lesssim M_{\rm p} \lesssim 3 \times 10^{21}\,{\rm g}$. For $\Delta = 5$, the MF calculated in

Ref. [128] is skewed towards large masses and the skew-lognormal MF provides a significantly better fit than the lognormal and generalised critical collapse MFs. For the skew-lognormal MF $f_{\rm PBH} = 1$ is allowed for $2 \times 10^{18}\,{\rm g} \lesssim M_{\rm p} \lesssim 1 \times 10^{19}\,{\rm g}$. The lognormal and generalised critical collapse MFs over (under) estimate the MF at low (high) masses, resulting in overly stringent evaporation (overly weak microlensing) constraints. The range of $M_{\rm p}$ where $f_{\rm PBH} = 1$ is allowed is therefore wider and shifted to larger $M_{\rm p}$ (compared to the better-fitting skew-lognormal MF). For $\Delta = 5$ the strongest evaporation constraints come from Voyager 1, even though for a delta-function MF the INTEGRAL/SPI MeV gamma-ray constraint excludes $f_{\rm PBH} = 1$ at larger masses than the Voyager 1 constraint (see Fig. 3.1). This is because for $\Delta = 5$ the MF is sufficiently wide that it is non-negligible in the mass range $M_{\rm PBH} \lesssim 10^{16}$ g where the Voyager 1 constraint is more stringent than the INTEGRAL/SPI MeV gamma-ray constraint, and for the Voyager 1 constraint the integral in Eq. (3.13) is dominated by this mass range. This highlights that for a broad MF the tightest constraint (i.e. the constraint that rules out $f_{\rm PBH} = 1$ at the largest peak mass) might not be the constraint which is tightest for a delta-function MF.

For $\Delta \lesssim 2$, the difference between the evaporation constraints calculated using the time-evolved MF $\psi_{\rm N}(M_{\rm PBH}, t_0)$ and the initial MF $\psi(M_{\rm PBH,\,i}, t_{\rm i})$ is no more than 10%, for $M_{\rm p} \gtrsim 10^{17}\,{\rm g}$. For $\Delta = 5$, the constraints obtained using $\psi_{\rm N}(M_{\rm PBH}, t_0)$ and $\psi(M_{\rm PBH,\,i}, t_{\rm i})$ differ by no more than a factor of two at $M_{\rm p} = 10^{17}\,{\rm g}$ and less than $\approx 20\%$ at peak masses where $f_{\rm PBH} \sim 1$. For broader mass functions (or for MFs peaked at smaller masses [315]) the effect on the constraints on $f_{\rm PBH}$ would be larger.

3.3.2 Prospective future constraints

Fig. 3.3 shows prospective future constraints obtained from MeV gamma-ray telescopes [307] and a proposed microlensing survey of white dwarfs in the LMC [308], as discussed in Sec. 3.2.1. Due to the improved sensitivity compared to existing observations, $f_{\rm PBH} = 1$ is excluded over a wider peak mass range than for existing constraints. In particular for the broadest peak in the primordial power spectrum, $\Delta = 5$, $f_{\rm PBH} = 1$ is excluded across the whole asteroid-mass window for all three MFs, and the maximum allowed PBH dark matter fraction is $f_{\rm PBH} \sim 0.2 - 0.4$. For $\Delta = 5$ the current Voyager 1 constraint [159] rules out $f_{\rm PBH} = 1$ at larger $M_{\rm p}$ than the projected future MeV gamma-ray constraint that we consider, even though the largest mass for which $f_{\rm PBH} = 1$ is excluded for a delta-function MF is smaller for the Voyager 1 $e^{\pm}$ constraint. As for the current MeV gamma-ray constraint, this is because the low-mass tails of the widest MFs are large at $M_{\rm PBH} \lesssim 10^{16}\,{\rm g}$, where the delta-function MF constraint from Voyager 1 [159] is tighter.

3.3.3 Comparison with previous constraints for lognormal mass function

Carr and collaborators [156, 287] have previously calculated constraints on $f_{\rm PBH}$ for a lognormal MF with width $\sigma = 2$. In Fig. 3.4, we reproduce the evaporation and microlensing constraints shown in Fig. 20 of Ref. [156] for a lognormal MF with width $\sigma = 2$ (as well as the original delta-function MF constraints). Their constraints differ significantly more from the delta-function MF constraints than is the case for the widest lognormal MF we consider, which has $\sigma = 1.8$ [128]. In this section we outline the reasons

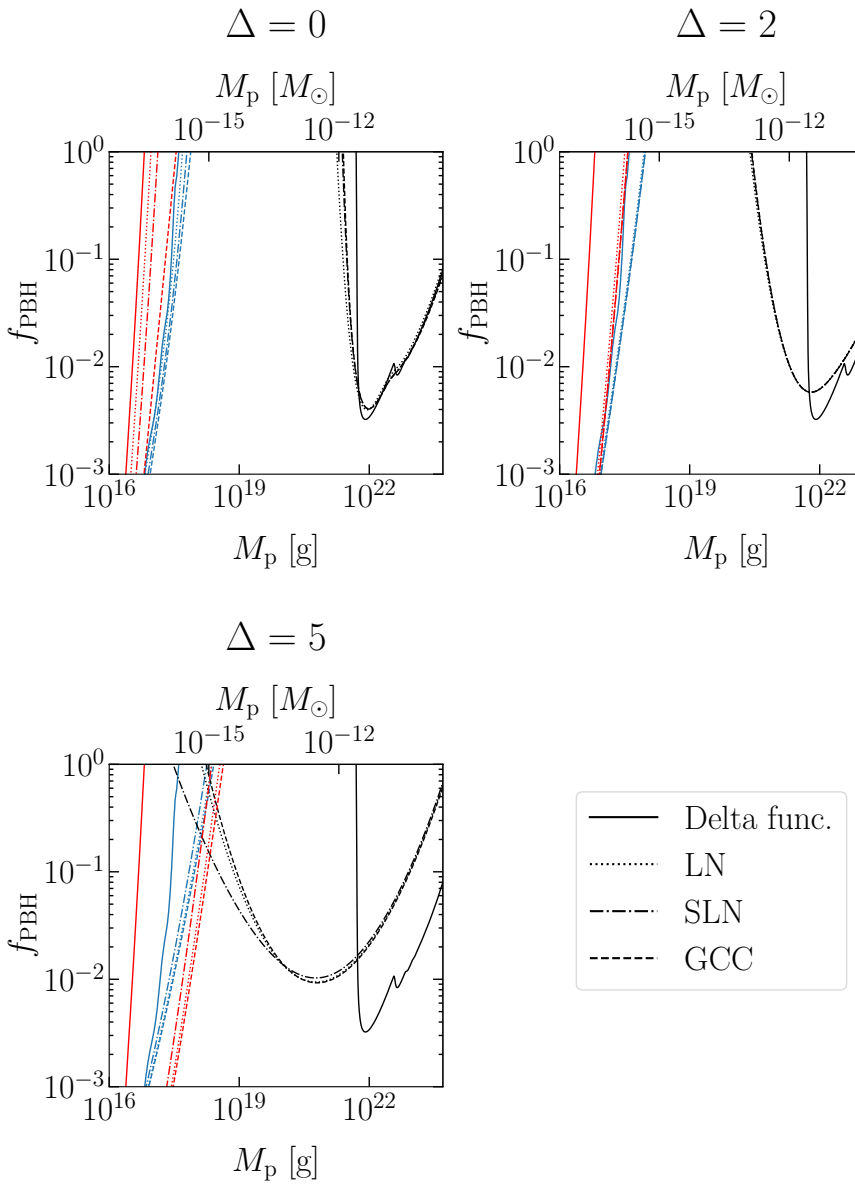

Figure 3.3: *Prospective future constraints on the fraction of dark matter in PBHs, $f_{\rm PBH}$, as a function of the mass at which the PBH MF peaks, $M_{\rm p}$, for PBHs formed from a lognormal peak in the primordial power spectrum with width $\Delta = 0$ (top left), $\Delta = 2$ (top right) and $\Delta = 5$ (bottom left). The line styles for the MFs are the same as in Fig. 3.2. The future constraints shown are from future MeV gamma-ray telescopes (assuming a NFW profile for the Galactic DM halo) [307] (light blue) and stellar microlensing of white dwarfs in the LMC [308] (black). For comparison we also show the current constraints from Voyager 1 measurements of the $e^{\pm}$ flux (red) from Fig. 3.2.*

for this apparent difference.

Fig. 3.5 shows the most stringent constraints on $f_{\rm PBH}$, from Voyager 1 [159], for a lognormal MF with $\sigma = 1.8$ and $\sigma = 2$ plotted as a function of both $M_{\rm c}$

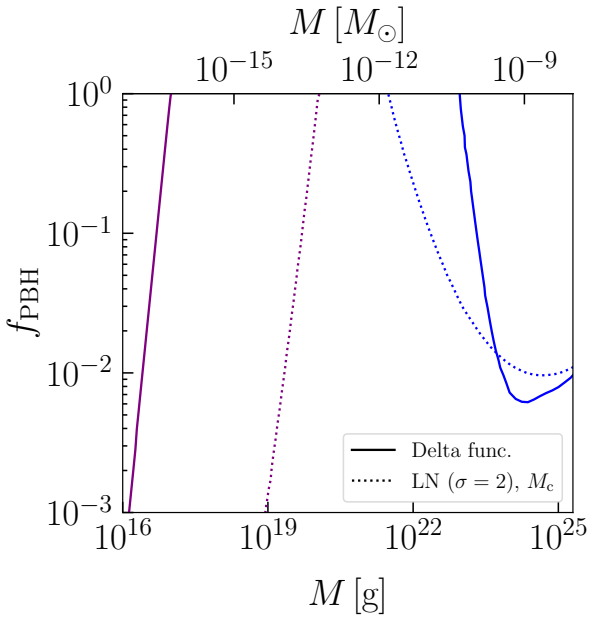

Figure 3.4: *Constraints on the fraction of dark matter in PBHs, $f_{\rm PBH}$, from extragalactic gamma rays as calculated in Ref. [156] (purple) and microlensing from Subaru-HSC as calculated in Ref. [311] (blue), for a delta-function MF and a lognormal (LN) MF with width $\sigma = 2$, as shown in Fig. 20 of Ref. [156]. The constraints for a delta-function MF are shown with solid lines as a function of the PBH mass $M_{\rm PBH}$. The constraints for a LN MF, Eq. (3.5), are shown as a function of $M_{\rm c}$ (as in Fig. 20 of Ref. [156]) with dotted lines.*

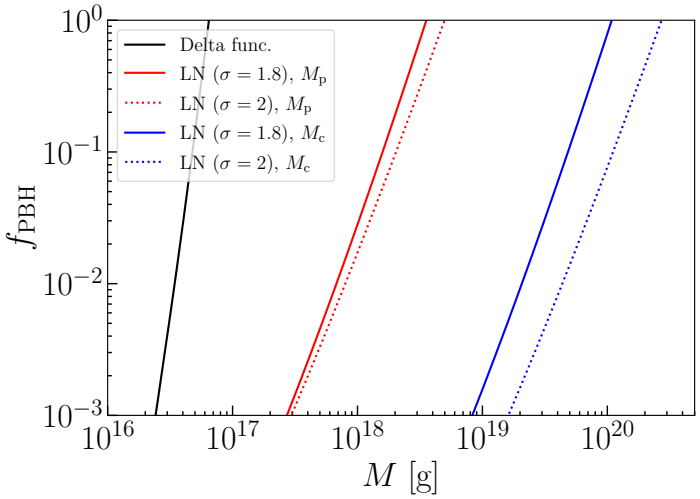

Figure 3.5: *The constraints on the fraction of dark matter in PBHs, $f_{\rm PBH}$, from Voyager 1 measurements of the local flux of electrons and positrons [159] for a delta-function MF and a lognormal (LN) MF. The constraint for a delta-function MF is shown with a black solid line as a function of the PBH mass $M_{\rm PBH}$. The constraint for the LN MF, Eq. (3.5), is shown as a function of both $M_{\rm p}$ (red) and $M_{\rm c}$ (blue) for $\sigma = 1.8$ and 2 (solid and dotted lines respectively).*

and $M_{\rm p}$. The main reason for the apparent difference between our results in Fig. 3.2 and those in Fig. 20 of Ref. [156] is that the constraints appear significantly different when plotted in terms of the peak mass, $M_{\rm p}$, than when plotted in terms of the parameter $M_{\rm c}$, which appears in the definition of the lognormal MF (Eq. (3.5)). This mass parameter, $M_{\rm c}$, is the mean of $M_{\rm PBH,i}\psi(M_{\rm PBH,i}, t_{\rm i})$ for the lognormal MF and is related to the peak mass by $M_{\rm c} = M_{\rm p}\exp(\sigma^2)$, so that for $\sigma \approx 2$, $M_{\rm c} \approx 50 M_{\rm p}$. The peak mass better reflects the typical mass of the PBHs, and plotting constraints in terms of the peak mass also allows comparison with other mass functions with a single peak. Furthermore the value for the width of the lognormal used in Refs. [156, 287], $\sigma = 2$, is larger than that of the best fit lognormal to the widest power spectrum considered by Gow et al. [128], $\sigma = 1.8$, and this relatively small difference in σ leads to a significant shift in the evaporation constraint when it is plotted as a function of $M_{\rm c}$.

3.4 Conclusions

If the PBH mass function is a delta-function then PBHs with mass in the asteroid-mass window, $10^{17}\,{\rm g} \lesssim M_{\rm p} \lesssim 10^{22}\,{\rm g}$, can make up all of the DM, i.e. $f_{\rm PBH} = 1$. However, due to critical collapse, PBHs formed from the collapse of large density perturbations are expected to have an extended MF, even if they form from a narrow peak in the power spectrum. Refs. [156, 287] found that the range of masses for which $f_{\rm PBH} = 1$ is allowed is much smaller for the commonly used lognormal MF than for a delta-function MF. We have explored how constraints on $f_{\rm PBH}$ in the asteroid-mass window depend on the shape of the PBH MF. In addition to a lognormal MF, we use the skew-lognormal and generalised critical collapse MFs, which Gow et al. [128] found provided a better fit to the MFs they calculated than the

lognormal.

We find, using the constraints from Voyager 1 measurements of the local $e^{\pm}$ flux [159], INTEGRAL/SPI observations of MeV gamma rays [160], and microlensing constraints from Subaru-HSC [183, 306], that the asteroid-mass window is typically narrower (i.e. $f_{\rm PBH} = 1$ is allowed for a smaller range of peak masses, $M_{\rm p}$) for the better fitting MFs than for the lognormal MF. Nevertheless, for the widest primordial power spectrum considered by Gow et al. [128], there is still a range of $M_{\rm p}$ values (2×10^{18} g $\lesssim M_{\rm p} \lesssim 1 \times 10^{19}$ g) where $f_{\rm PBH} = 1$ is allowed for the skew-lognormal mass function, which is the best-fitting mass function in this case.

The constraint that excludes $f_{\rm PBH} = 1$ over the widest range of PBH masses for a delta-function MF does not always exclude $f_{\rm PBH} = 1$ for the widest range of peak masses for extended mass functions. For instance the largest mass for which $f_{\rm PBH} = 1$ is excluded for a delta-function MF is smaller for the Voyager 1 $e^{\pm}$ constraint than for the MeV gamma-ray constraints (see Fig. 3.1). However for the widest MFs we consider, the Voyager 1 constraint rules out $f_{\rm PBH} = 1$ at larger $M_{\rm p}$ than the current INTEGRAL/SPI MeV gamma-ray constraint and also the projected future MeV gamma-ray constraint that we consider. This shows that tighter constraints on PBHs with $M_{\rm PBH} \lesssim 10^{16}\,{\rm g}$ would be beneficial for constraining PBHs with broad MFs.

Future gamma-ray observations will improve limits on the abundance of PBHs with masses $M_{\rm PBH} \lesssim 5 \times 10^{17}\,{\rm g}$, while a proposed LMC white dwarf microlensing survey could provide tighter constraints for $5 \times 10^{21}\,{\rm g} \lesssim M_{\rm PBH} \lesssim 2 \times 10^{23}\,{\rm g}$. Together, these constraints could potentially exclude asteroid-mass PBHs with a broad MF making up all of the DM. However the evaporation and microlensing constraints are sensitive to the shape of

the low and high mass tails of the MF respectively. An accurate calculation of the shape of the tails of the MF will therefore be essential in future for assessing whether evaporation and microlensing constraints allow asteroid-mass PBHs to make up all of the DM. This also demonstrates the importance of developing new observational probes of PBHs with mass $10^{18}\,\mathrm{g} \lesssim M_{\mathrm{PBH}} \lesssim 10^{22}\,\mathrm{g}$ (see Sec. 1.4.5).

Chapter 4

Conclusions

Observations of galaxies, galaxy clusters, anisotropies in the cosmic microwave background and the growth of large-scale structure provide compelling evidence for the existence of cold non-baryonic dark matter that makes up $\approx 85\%$ of the total matter content in the Universe. The nature of dark matter remains a major unresolved question in cosmology. Particle dark matter candidates, such as weakly interacting massive particles (WIMPs) and axions, have not been detected in spite of great experimental efforts. An alternative scenario is that dark matter consists (in whole or in part) of black holes formed in the early Universe, so-called 'primordial black holes' (PBHs).

Constraints on the abundance of PBHs arise from their Hawking evaporation, microlensing, gravitational waves, dynamical effects and accretion. These constraints appear to exclude PBHs from making up all of the dark matter unless their mass is in the range $10^{17}\,\mathrm{g} \lesssim M_{\mathrm{PBH}} \lesssim 10^{22}\,\mathrm{g}$, often known as the 'asteroid-mass window'. Constraints are calculated under various assumptions and a more realistic treatment may modify the excluded mass range. In this thesis, we recalculate constraints using more

realistic PBH mass and spatial distributions.

In Chapter 2, we study the effect of PBH clustering on microlensing constraints. Previous work found that if PBHs are in clusters sufficiently compact that each cluster acts as a single lens, constraints are shifted to smaller masses and limits on PBHs of mass $M_{\rm PBH} \sim 10 M_\odot$ may be weakened or evaded. We consider the scenario that PBHs form from the collapse of large gaussian density fluctuations generated by inflation. In this case, Poisson noise in their initial distribution leads to the formation of PBH clusters shortly after matter-radiation equality. We review the properties of these clusters, showing that each PBH acts as a single lens (rather than the cluster as a whole). We assume all PBHs have the same mass, $M_{\rm PBH}$, and all are found in clusters containing the same number of PBHs, $N_{\rm cl}$. Some fraction of PBHs would not be in clusters today, since some PBHs would have once been in clusters that have now evaporated and others never became part of a cluster at all. Our results are therefore an upper limit to the effect of clustering on microlensing constraints.

Assuming all PBHs are in clusters of mass $M_{\rm cl} \lesssim 10^6 M_\odot$, the differential event rate is very close to that for smoothly-distributed dark matter and hence the effect of clustering on microlensing constraints is negligible. Assuming all PBHs are in more massive clusters, $M_{\rm cl} \gtrsim 10^6 M_\odot$, the differential event rate deviates substantially from that found for smoothly-distributed dark matter. We explored how this deviation arises due to rare clusters close to the observer that produce a high rate of short-duration events. In this case the behaviour of the differential event rate causes the probability distribution of the number of microlensing events to peak at smaller numbers of events, resulting in weaker constraints than for smoothly-distributed dark matter.

We expect clusters containing $N_{\rm cl} \sim 10^3$ PBHs to be the most common, since smaller clusters will have evaporated and larger clusters form much more rarely. Since clustering has a negligible effect on observations if the cluster mass $M_{\rm cl} \lesssim 10^6 M_\odot$, it has a negligible effect on constraints from the EROS-2 survey (which constrains PBHs of mass $M_{\rm PBH} \lesssim 10 M_\odot$). To understand the effects on more massive PBHs we considered a prospective survey sensitive to PBHs of mass $M_{\rm PBH} \gtrsim 10^3 M_\odot$ (since this work was completed the OGLE-III and OGLE-IV surveys have constrained PBHs of mass up to $M_{\rm PBH} \sim 10^4 M_\odot$). Assuming all PBHs have a mass $M_{\rm PBH} = 10^3 M_\odot$ and are in clusters containing $N_{\rm cl} = 10^3$ PBHs, the constraints from this prospective survey are only $\mathcal{O}(10\%)$ weaker than those calculated for smoothly-distributed dark matter. We therefore conclude that clustering of PBHs has only a small effect on microlensing constraints for PBHs formed from the collapse of large gaussian density fluctuations.

In Chapter 3, we recalculate current and prospective constraints from evaporation and microlensing (which constrain PBHs of mass $M_{\rm PBH} \lesssim 10^{17}\,{\rm g}$ and $M_{\rm PBH} \gtrsim 10^{22}\,{\rm g}$, respectively), to assess how open the asteroid-mass window remains when considering more realistic PBH mass functions. Near-critical gravitational collapse means that PBHs will have an extended mass function even if they all form at the same time (from a delta-function peak in the power spectrum). We consider the widely-used lognormal mass function, as well as the fitting functions found by Gow et al. [128], which provide a better fit to the tails of the mass function than the lognormal. Constraints on PBHs with an extended mass function are sensitive to the tails of the mass function (especially for wide mass functions), so an accurate calculation of the tails is crucial for assessing whether evaporation and microlensing constraints allow asteroid-mass PBHs to make up all of the dark matter.

For existing constraints, we find the asteroid-mass window is typically narrower when using the fitting functions from Gow et al. [128] than for the log-normal, though it is not entirely closed even for the widest mass functions considered. Prospective evaporation and microlensing constraints may be able to close the window, depending on the width of the mass function. We also observe that stringent constraints on PBHs of masses $M_{\rm PBH} \lesssim 10^{16}\,{\rm g}$ play an important role in narrowing (or closing) the asteroid-mass window for wide mass functions.

This work contributes to ongoing efforts to understand whether PBHs are a viable dark matter candidate. In recent years, there have been significant developments in observational constraints and theoretical modelling of PBHs, and further progress is expected. Proposed gamma-ray telescopes such as GECCO and AMEGO could probe the currently unconstrained mass range at the lower end of the asteroid-mass window, and a proposed microlensing survey of white dwarfs in the Large Magellanic Cloud may tighten constraints on PBHs of mass $M_{\rm PBH} \sim 10^{22}\,{\rm g}$. These techniques are limited, however, by the rapid decrease of rate of particle emission from PBHs (due to their Hawking radiation) with increasing mass ($\dot{M}_{\rm PBH} \propto 1/M_{\rm PBH}^2$) and wave optics effects which make it impossible for microlensing surveys of main-sequence stars to constrain PBHs of mass $M_{\rm PBH} \lesssim 10^{22}\,{\rm g}$. Probing asteroid-mass PBHs (to either detect or exclude them) therefore requires other techniques, and there are a variety of proposals that may make this possible in the near-future. Challenges remain in accurately modelling PBHs. These include the calculation of the probability distribution of large fluctuations in inflation models (and therefore the resulting PBH abundance and mass function) and understanding the evolution of PBH clusters to the present. Continued work on observational probes of PBHs, particularly those sensitive to asteroid-mass PBHs, com-

plemented by advances in theoretical modelling of PBH formation and their clustering evolution, will allow for a better understanding of the viability of PBHs as a dark matter candidate.

Bibliography

[1] A. R. Liddle and D. H. Lyth. *Cosmological inflation and large scale structure*. 2000. ISBN: 978-0-521-57598-0, 978-0-521-82849-9.

[2] A. G. Riess et al. "Observational evidence from supernovae for an accelerating universe and a cosmological constant". *Astron. J.* 116 (1998), pp. 1009–1038. arXiv: astro-ph/9805201.

[3] S. Perlmutter et al. "Measurements of Ω and Λ from 42 High Redshift Supernovae". *Astrophys. J.* 517 (1999), pp. 565–586. arXiv: astro-ph/9812133.

[4] N. Aghanim et al. "Planck 2018 results. VI. Cosmological parameters". *Astron. Astrophys.* 641 (2020). [Erratum: Astron.Astrophys. 652, C4 (2021)], A6. arXiv: 1807.06209 [astro-ph.CO].

[5] A. G. Adame et al. "DESI 2024 VI: Cosmological Constraints from the Measurements of Baryon Acoustic Oscillations" (2024). arXiv: 2404.03002 [astro-ph.CO].

[6] G. Steigman. "Primordial Nucleosynthesis in the Precision Cosmology Era". *Ann. Rev. Nucl. Part. Sci.* 57 (2007), pp. 463–491. arXiv: 0712.1100 [astro-ph].

[7] R. H. Cyburt et al. "Big Bang Nucleosynthesis: 2015". *Rev. Mod. Phys.* 88 (2016), p. 015004. arXiv: 1505.01076 [astro-ph.CO].

[8] C. Pitrou et al. "Precision big bang nucleosynthesis with improved Helium-4 predictions". *Phys. Rept.* 754 (2018), pp. 1–66. arXiv: 1801.08023 [astro-ph.CO].

[9] T.-H. Yeh et al. "Probing physics beyond the standard model: limits from BBN and the CMB independently and combined". *JCAP* 10 (2022), p. 046. arXiv: 2207.13133 [astro-ph.CO].

[10] O. Pisanti et al. "Primordial Deuterium after LUNA: concordances and error budget". *JCAP* 04 (2021), p. 020. arXiv: 2011.11537 [astro-ph.CO].

[11] T.-H. Yeh, K. A. Olive, and B. D. Fields. "The impact of new $d(p,\gamma)3$ rates on Big Bang Nucleosynthesis". *JCAP* 03 (2021), p. 046. arXiv: 2011.13874 [astro-ph.CO].

[12] D. J. Fixsen et al. "The Cosmic Microwave Background spectrum from the full COBE/FIRAS data set". *Astrophys. J.* 473 (1996), p. 576. arXiv: astro-ph/9605054.

[13] D. J. Fixsen. "The Temperature of the Cosmic Microwave Background". *Astrophys. J.* 707 (2009), pp. 916–920. arXiv: 0911.1955 [astro-ph.CO].

[14] G. F. Smoot et al. "Structure in the COBE differential microwave radiometer first year maps". *Astrophys. J. Lett.* 396 (1992), pp. L1–L5.

[15] K. A. Malik and D. Wands. "Cosmological perturbations". *Phys. Rept.* 475 (2009), pp. 1–51. arXiv: 0809.4944 [astro-ph].

[16] D. Baumann. *Advanced Cosmology lecture notes*. 2016. URL: http://cosmology.amsterdam/education/advanced-cosmology/.

[17] Y. Akrami et al. "Planck 2018 results. X. Constraints on inflation". *Astron. Astrophys.* 641 (2020), A10. arXiv: 1807.06211 [astro-ph.CO].

[18] J. E. Gunn and J. R. Gott III. "On the Infall of Matter into Clusters of Galaxies and Some Effects on Their Evolution". *Astrophys. J.* 176 (1972), pp. 1–19.

[19] G. L. Bryan and M. L. Norman. "Statistical properties of x-ray clusters: Analytic and numerical comparisons". *Astrophys. J.* 495 (1998), p. 80. arXiv: astro-ph/9710107.

[20] F. Pace, J. C. Waizmann, and M. Bartelmann. "Spherical collapse model in dark energy cosmologies". *Mon. Not. Roy. Astron. Soc.* 406 (2010), p. 1865. arXiv: 1005.0233 [astro-ph.CO].

[21] Y. Akrami et al. "Planck 2018 results. IX. Constraints on primordial non-Gaussianity". *Astron. Astrophys.* 641 (2020), A9. arXiv: 1905.05697 [astro-ph.CO].

[22] M. Taoso, G. Bertone, and A. Masiero. "Dark Matter Candidates: A Ten-Point Test". *JCAP* 03 (2008), p. 022. arXiv: 0711.4996 [astro-ph].

[23] M. Milgrom. "A Modification of the Newtonian dynamics as a possible alternative to the hidden mass hypothesis". *Astrophys. J.* 270 (1983), pp. 365–370.

[24] J. D. Bekenstein. "Relativistic gravitation theory for the MOND paradigm". *Phys. Rev. D* 70 (2004). [Erratum: Phys.Rev.D 71, 069901 (2005)], p. 083509. arXiv: astro-ph/0403694.

[25] A. Slosar, A. Melchiorri, and J. Silk. "Did Boomerang hit MOND?" *Phys. Rev. D* 72 (2005), p. 101301. arXiv: astro-ph/0508048.

[26] C. Skordis et al. "Large Scale Structure in Bekenstein's theory of relativistic Modified Newtonian Dynamics". *Phys. Rev. Lett.* 96 (2006), p. 011301. arXiv: astro-ph/0505519.

[27] J. Zuntz et al. "Vector field models of modified gravity and the dark sector". *Phys. Rev. D* 81 (2010), p. 104015. arXiv: 1002.0849 [astro-ph.CO].

[28] C. Skordis and T. Zlosnik. "New Relativistic Theory for Modified Newtonian Dynamics". *Phys. Rev. Lett.* 127.16 (2021), p. 161302. arXiv: 2007.00082 [astro-ph.CO].

[29] V. C. Rubin and W. K. Ford Jr. "Rotation of the Andromeda Nebula from a Spectroscopic Survey of Emission Regions". *Astrophys. J.* 159 (1970), pp. 379–403.

[30] K. C. Freeman. "On the disks of spiral and SO Galaxies". *Astrophys. J.* 160 (1970), p. 811.

[31] D. H. Rogstad and G. S Shostak. "Gross Properties of Five Scd Galaxies as Determined from 21-centimeter Observations". *Astrophysical Journal* 176 (1972), p. 315.

[32] A. Bosma. "The distribution and kinematics of neutral hydrogen in spiral galaxies of various morphological types". PhD thesis. University of Groningen, Netherlands, 1978.

[33] V. C. Rubin, J. Ford W. K., and N. Thonnard. "Extended rotation curves of high-luminosity spiral galaxies. IV. Systematic dynamical properties, Sa -> Sc." *Astrophysical Journal, Letters* 225 (1978), pp. L107–L111.

[34] F. Zwicky. "Die Rotverschiebung von extragalaktischen Nebeln". *Helv. Phys. Acta* 6 (1933), pp. 110–127.

[35] H. Boehringer and N. Werner. "X-ray Spectroscopy of Galaxy Clusters". *Astron. Astrophys. Rev.* 18 (2010), pp. 127–196. arXiv: 0907.4277 [astro-ph.CO].

[36] S. Ettori et al. "Mass profiles of Galaxy Clusters from X-ray analysis". *Space Sci. Rev.* 177 (2013), pp. 119–154. arXiv: 1303.3530 [astro-ph.CO].

[37] D. Clowe, A. Gonzalez, and M. Markevitch. "Weak lensing mass reconstruction of the interacting cluster 1E0657-558: Direct evidence for the existence of dark matter". *Astrophys. J.* 604 (2004), pp. 596–603. arXiv: astro-ph/0312273.

[38] D. Clowe et al. "A direct empirical proof of the existence of dark matter". *Astrophys. J. Lett.* 648 (2006), pp. L109–L113. arXiv: astro-ph/0608407.

[39] M. Bradac et al. "Revealing the properties of dark matter in the merging cluster MACSJ0025.4-1222". *Astrophys. J.* 687 (2008), p. 959. arXiv: 0806.2320 [astro-ph].

[40] W. A. Dawson et al. "Discovery of a Dissociative Galaxy Cluster Merger with Large Physical Separation". *Astrophys. J. Lett.* 747 (2012), p. L42. arXiv: 1110.4391 [astro-ph.CO].

[41] D. Harvey et al. "The non-gravitational interactions of dark matter in colliding galaxy clusters". *Science* 347 (2015), pp. 1462–1465. arXiv: 1503.07675 [astro-ph.CO].

[42] S. Profumo, L. Giani, and O. F. Piattella. "An Introduction to Particle Dark Matter". *Universe* 5.10 (2019), p. 213. arXiv: 1910.05610 [hep-ph].

[43] J. Carron, M. Mirmelstein, and A. Lewis. "CMB lensing from Planck PR4 maps". *JCAP* 09 (2022), p. 039. arXiv: 2206.07773 [astro-ph.CO].

[44] F. J. Qu et al. "The Atacama Cosmology Telescope: A Measurement of the DR6 CMB Lensing Power Spectrum and Its Implications

for Structure Growth". *Astrophys. J.* 962.2 (2024), p. 112. arXiv: 2304.05202 [astro-ph.CO].

[45] M. S. Madhavacheril et al. "The Atacama Cosmology Telescope: DR6 Gravitational Lensing Map and Cosmological Parameters". *Astrophys. J.* 962.2 (2024), p. 113. arXiv: 2304.05203 [astro-ph.CO].

[46] N. MacCrann et al. "The Atacama Cosmology Telescope: Mitigating the Impact of Extragalactic Foregrounds for the DR6 Cosmic Microwave Background Lensing Analysis". *Astrophys. J.* 966.1 (2024), p. 138. arXiv: 2304.05196 [astro-ph.CO].

[47] J. F. Navarro, C. S. Frenk, and S. D. M. White. "A Universal density profile from hierarchical clustering". *Astrophys. J.* 490 (1997), pp. 493–508. arXiv: astro-ph/9611107.

[48] J. Binney and S. Tremaine. *Galactic Dynamics: Second Edition*. Princeton University Press, 2008.

[49] Y. Sofue. "Rotation Curve of the Milky Way and the Dark Matter Density". *Galaxies* 8.2 (2020), p. 37. arXiv: 2004.11688 [astro-ph.GA].

[50] P. F. de Salas and A. Widmark. "Dark matter local density determination: recent observations and future prospects". *Rept. Prog. Phys.* 84.10 (2021), p. 104901. arXiv: 2012.11477 [astro-ph.GA].

[51] F. J. Kerr and D. Lynden-Bell. "Review of galactic constants." *Mon. Not. Roy. Astron. Soc.* 221 (1986), pp. 1023–1038.

[52] M. J. Reid et al. "Trigonometric Parallaxes of High Mass Star Forming Regions: The Structure and Kinematics of the Milky Way". *Astrophysical Journal* 783.2, 130 (2014), p. 130. arXiv: 1401.5377 [astro-ph.GA].

[53] A.-C. Eilers et al. "The Circular Velocity Curve of the Milky Way from 5 to 25 kpc". *Astrophysical Journal* 871.1, 120 (2019), p. 120. arXiv: 1810.09466 [astro-ph.GA].

[54] V. Springel et al. "The Aquarius Project: the subhalos of galactic halos". *Mon. Not. Roy. Astron. Soc.* 391 (2008), pp. 1685–1711. arXiv: 0809.0898 [astro-ph].

[55] J. Richings et al. "Subhalo destruction in the APOSTLE and AURIGA simulations". *Mon. Not. Roy. Astron. Soc.* 492.4 (2020), pp. 5780–5793. arXiv: 1811.12437 [astro-ph.GA].

[56] G. Bertone, D. Hooper, and J. Silk. "Particle dark matter: Evidence, candidates and constraints". *Phys. Rept.* 405 (2005), pp. 279–390. arXiv: hep-ph/0404175.

[57] L. Roszkowski, E. M. Sessolo, and S. Trojanowski. "WIMP dark matter candidates and searches—current status and future prospects". *Rept. Prog. Phys.* 81.6 (2018), p. 066201. arXiv: 1707.06277 [hep-ph].

[58] J. Billard et al. "Direct detection of dark matter—APPEC committee report". *Rept. Prog. Phys.* 85.5 (2022), p. 056201. arXiv: 2104.07634 [hep-ex].

[59] F. Chadha-Day, J. Ellis, and D. J. E. Marsh. "Axion dark matter: What is it and why now?" *Sci. Adv.* 8.8 (2022), abj3618. arXiv: 2105.01406 [hep-ph].

[60] R. J. Scherrer and M. S. Turner. "On the Relic, Cosmic Abundance of Stable Weakly Interacting Massive Particles". *Phys. Rev. D* 33 (1986). [Erratum: Phys.Rev.D 34, 3263 (1986)], p. 1585.

[61] S. P. Martin. "A Supersymmetry primer". *Adv. Ser. Direct. High Energy Phys.* 18 (1998). Ed. by G. L. Kane, pp. 1–98. arXiv: hep-ph/9709356.

[62] G. R. Farrar and P. Fayet. "Phenomenology of the Production, Decay, and Detection of New Hadronic States Associated with Supersymmetry". *Phys. Lett. B* 76 (1978), pp. 575–579.

[63] J. Aalbers et al. "Dark Matter Search Results from 4.2 Tonne-Years of Exposure of the LUX-ZEPLIN (LZ) Experiment" (2024). arXiv: 2410.17036 [hep-ex].

[64] Z. Bo et al. "Dark Matter Search Results from 1.54 Tonne·Year Exposure of PandaX-4T" (2024). arXiv: 2408.00664 [hep-ex].

[65] E. Aprile et al. "First Dark Matter Search with Nuclear Recoils from the XENONnT Experiment". *Phys. Rev. Lett.* 131.4 (2023), p. 041003. arXiv: 2303.14729 [hep-ex].

[66] M. Ackermann et al. "Searching for Dark Matter Annihilation from Milky Way Dwarf Spheroidal Galaxies with Six Years of Fermi Large Area Telescope Data". *Phys. Rev. Lett.* 115.23 (2015), p. 231301. arXiv: 1503.02641 [astro-ph.HE].

[67] M. Ackermann et al. "The Fermi Galactic Center GeV Excess and Implications for Dark Matter". *Astrophys. J.* 840.1 (2017), p. 43. arXiv: 1704.03910 [astro-ph.HE].

[68] K. Choi et al. "Search for neutrinos from annihilation of captured low-mass dark matter particles in the Sun by Super-Kamiokande". *Phys. Rev. Lett.* 114.14 (2015), p. 141301. arXiv: 1503.04858 [hep-ex].

[69] R. Abbasi et al. "Search for GeV-scale dark matter annihilation in the Sun with IceCube DeepCore". *Phys. Rev. D* 105.6 (2022), p. 062004. arXiv: 2111.09970 [astro-ph.HE].

[70] C. Abel et al. "Measurement of the Permanent Electric Dipole Moment of the Neutron". *Phys. Rev. Lett.* 124.8 (2020), p. 081803. arXiv: 2001.11966 [hep-ex].

[71] R. D. Peccei and H. R. Quinn. "CP Conservation in the Presence of Instantons". *Phys. Rev. Lett.* 38 (1977), pp. 1440–1443.

[72] R. D. Peccei and H. R. Quinn. "Constraints Imposed by CP Conservation in the Presence of Instantons". *Phys. Rev. D* 16 (1977), pp. 1791–1797.

[73] S. Weinberg. "A New Light Boson?" *Phys. Rev. Lett.* 40 (1978), pp. 223–226.

[74] F. Wilczek. "Problem of Strong P and T Invariance in the Presence of Instantons". *Phys. Rev. Lett.* 40 (1978), pp. 279–282.

[75] A. Arvanitaki et al. "String Axiverse". *Phys. Rev. D* 81 (2010), p. 123530. arXiv: 0905.4720 [hep-th].

[76] S. J. Asztalos et al. "A SQUID-based microwave cavity search for dark-matter axions". *Phys. Rev. Lett.* 104 (2010), p. 041301. arXiv: 0910.5914 [astro-ph.CO].

[77] K. Altenmüller et al. "New Upper Limit on the Axion-Photon Coupling with an Extended CAST Run with a Xe-Based Micromegas Detector". *Phys. Rev. Lett.* 133.22 (2024), p. 221005. arXiv: 2406.16840 [hep-ex].

[78] K. Ehret et al. "New ALPS Results on Hidden-Sector Lightweights". *Phys. Lett. B* 689 (2010), pp. 149–155. arXiv: 1004.1313 [hep-ex].

[79] R. Ballou et al. "New exclusion limits on scalar and pseudoscalar axionlike particles from light shining through a wall". *Phys. Rev. D* 92.9 (2015), p. 092002. arXiv: 1506.08082 [hep-ex].

[80] C. O'Hare. *cajohare/AxionLimits: AxionLimits*. https://cajohare.github.io/AxionLimits/. Version v1.0. 2020.

[81] P. Carenza et al. "Axion Astrophysics" (2024). arXiv: 2411.02492 [hep-ph].

[82] Y. B. Zel'dovich and I. D. Novikov. "The Hypothesis of Cores Retarded during Expansion and the Hot Cosmological Model". *Soviet Astron. AJ (Engl. Transl.),* 10 (1967), p. 602.

[83] S. Hawking. "Gravitationally collapsed objects of very low mass". *Mon. Not. Roy. Astron. Soc.* 152 (1971), p. 75.

[84] S. W. Hawking. "Black hole explosions". *Nature* 248 (1974), pp. 30–31.

[85] S. W. Hawking. "Particle Creation by Black Holes". *Commun. Math. Phys.* 43 (1975). Ed. by G. W. Gibbons and S. W. Hawking. [Erratum: Commun.Math.Phys. 46, 206 (1976)], pp. 199–220.

[86] D. N. Page. "Particle Emission Rates from a Black Hole: Massless Particles from an Uncharged, Nonrotating Hole". *Phys. Rev. D* 13 (1976), pp. 198–206.

[87] J. H. MacGibbon, B. J. Carr, and D. N. Page. "Do Evaporating Black Holes Form Photospheres?" *Phys. Rev. D* 78 (2008), p. 064043. arXiv: 0709.2380 [astro-ph].

[88] S. W. Hawking. "Black Holes From Cosmic Strings". *Phys. Lett. B* 231 (1989), pp. 237–239.

[89] A. Polnarev and R. Zembowicz. "Formation of Primordial Black Holes by Cosmic Strings". *Phys. Rev. D* 43 (1991), pp. 1106–1109.

[90] M. Crawford and D. N. Schramm. "Spontaneous Generation of Density Perturbations in the Early Universe". *Nature* 298 (1982), pp. 538–540.

[91] S. W. Hawking, I. G. Moss, and J. M. Stewart. "Bubble Collisions in the Very Early Universe". *Phys. Rev. D* 26 (1982), p. 2681.

[92] H. Kodama, M. Sasaki, and K. Sato. "Abundance of Primordial Holes Produced by Cosmological First Order Phase Transition". *Prog. Theor. Phys.* 68 (1982), p. 1979.

[93] B. J. Carr. "The Primordial black hole mass spectrum". *Astrophys. J.* 201 (1975), pp. 1–19.

[94] J. Yokoyama. "Formation of MACHO primordial black holes in inflationary cosmology". *Astron. Astrophys.* 318 (1997), p. 673. arXiv: astro-ph/9509027.

[95] E. R. Harrison. "Fluctuations at the threshold of classical cosmology". *Phys. Rev. D* 1 (1970), pp. 2726–2730.

[96] A. M. Green and A. R. Liddle. "Constraints on the density perturbation spectrum from primordial black holes". *Phys. Rev. D* 56 (1997), pp. 6166–6174. arXiv: astro-ph/9704251.

[97] V. De Luca et al. "Constraints on Primordial Black Holes: the Importance of Accretion". *Phys. Rev. D* 102.4 (2020), p. 043505. arXiv: 2003.12589 [astro-ph.CO].

[98] W. H. Press and P. Schechter. "Formation of galaxies and clusters of galaxies by self-similar gravitational condensation". *Astrophys. J.* 187 (1974), pp. 425–438.

[99] A. Kalaja et al. "From Primordial Black Holes Abundance to Primordial Curvature Power Spectrum (and back)". *JCAP* 10 (2019), p. 031. arXiv: 1908.03596 [astro-ph.CO].

[100] T. Nakama et al. "Identifying the most crucial parameters of the initial curvature profile for primordial black hole formation". *JCAP* 01 (2014), p. 037. arXiv: 1310.3007 [gr-qc].

[101] I. Musco. "Threshold for primordial black holes: Dependence on the shape of the cosmological perturbations". *Phys. Rev. D* 100.12 (2019), p. 123524. arXiv: 1809.02127 [gr-qc].

[102] I. Musco et al. "Threshold for primordial black holes. II. A simple analytic prescription". *Phys. Rev. D* 103.6 (2021), p. 063538. arXiv: 2011.03014 [astro-ph.CO].

[103] K. Jedamzik. "Primordial black hole formation during the QCD epoch". *Phys. Rev. D* 55 (1997), pp. 5871–5875. arXiv: astro-ph/9605152.

[104] K. Jedamzik and J. C. Niemeyer. "Primordial black hole formation during first order phase transitions". *Phys. Rev. D* 59 (1999), p. 124014. arXiv: astro-ph/9901293.

[105] C. T. Byrnes et al. "Primordial black holes with an accurate QCD equation of state". *JCAP* 08 (2018), p. 041. arXiv: 1801.06138 [astro-ph.CO].

[106] A. Escrivà, E. Bagui, and S. Clesse. "Simulations of PBH formation at the QCD epoch and comparison with the GWTC-3 catalog". *JCAP* 05 (2023), p. 004. arXiv: 2209.06196 [astro-ph.CO].

[107] T. Papanikolaou. "Toward the primordial black hole formation threshold in a time-dependent equation-of-state background". *Phys. Rev. D* 105.12 (2022), p. 124055. arXiv: 2205.07748 [gr-qc].

[108] I. Musco, K. Jedamzik, and S. Young. "Primordial black hole formation during the QCD phase transition: Threshold, mass distribution, and abundance". *Phys. Rev. D* 109.8 (2024), p. 083506. arXiv: 2303.07980 [astro-ph.CO].

[109] B. Carr et al. “Cosmic conundra explained by thermal history and primordial black holes”. *Phys. Dark Univ.* 31 (2021), p. 100755. arXiv: 1906.08217 [astro-ph.CO].

[110] A. Escrivà, C. Germani, and R. K. Sheth. “Universal threshold for primordial black hole formation”. *Phys. Rev. D* 101.4 (2020), p. 044022. arXiv: 1907.13311 [gr-qc].

[111] M. Shibata and M. Sasaki. “Black hole formation in the Friedmann universe: Formulation and computation in numerical relativity”. *Phys. Rev. D* 60 (1999), p. 084002. arXiv: gr-qc/9905064.

[112] J. S. Bullock and J. R. Primack. “Non-Gaussian fluctuations and primordial black holes from inflation”. *Phys. Rev. D* 55 (1997), pp. 7423–7439. arXiv: astro-ph/9611106.

[113] P. Ivanov. “Nonlinear metric perturbations and production of primordial black holes”. *Phys. Rev. D* 57 (1998), pp. 7145–7154. arXiv: astro-ph/9708224.

[114] M. Kawasaki and H. Nakatsuka. “Effect of nonlinearity between density and curvature perturbations on the primordial black hole formation”. *Phys. Rev. D* 99.12 (2019), p. 123501. arXiv: 1903.02994 [astro-ph.CO].

[115] S. Young, I. Musco, and C. T. Byrnes. “Primordial black hole formation and abundance: contribution from the non-linear relation between the density and curvature perturbation”. *JCAP* 11 (2019), p. 012. arXiv: 1904.00984 [astro-ph.CO].

[116] V. De Luca et al. “The Ineludible non-Gaussianity of the Primordial Black Hole Abundance”. *JCAP* 07 (2019), p. 048. arXiv: 1904.00970 [astro-ph.CO].

[117] J. R. Bond et al. “Excursion set mass functions for hierarchical Gaussian fluctuations”. *Astrophys. J.* 379 (1991), p. 440.

[118] A. Moradinezhad Dizgah, G. Franciolini, and A. Riotto. “Primordial Black Holes from Broad Spectra: Abundance and Clustering”. *JCAP* 11 (2019), p. 001. arXiv: 1906.08978 [astro-ph.CO].

[119] J. M. Bardeen et al. “The Statistics of Peaks of Gaussian Random Fields”. *Astrophys. J.* 304 (1986), pp. 15–61.

[120] A. M. Green et al. “A New calculation of the mass fraction of primordial black holes”. *Phys. Rev. D* 70 (2004), p. 041502. arXiv: astro-ph/0403181.

[121] S. Young, C. T. Byrnes, and M. Sasaki. “Calculating the mass fraction of primordial black holes”. *JCAP* 07 (2014), p. 045. arXiv: 1405.7023 [gr-qc].

[122] M. W. Choptuik. “Universality and scaling in gravitational collapse of a massless scalar field”. *Phys. Rev. Lett.* 70 (1993), pp. 9–12.

[123] J. C. Niemeyer and K. Jedamzik. “Near-critical gravitational collapse and the initial mass function of primordial black holes”. *Phys. Rev. Lett.* 80 (1998), pp. 5481–5484. arXiv: astro-ph/9709072.

[124] J. Yokoyama. “Cosmological constraints on primordial black holes produced in the near critical gravitational collapse”. *Phys. Rev. D* 58 (1998), p. 107502. arXiv: gr-qc/9804041.

[125] J. C. Niemeyer and K. Jedamzik. “Dynamics of primordial black hole formation”. *Phys. Rev. D* 59 (1999), p. 124013. arXiv: astro-ph/9901292.

[126] A. M. Green. “Microlensing and dynamical constraints on primordial black hole dark matter with an extended mass function”. *Phys. Rev. D* 94.6 (2016), p. 063530. arXiv: 1609.01143 [astro-ph.CO].

[127] K. Kannike et al. “Single Field Double Inflation and Primordial Black Holes”. *JCAP* 09 (2017), p. 020. arXiv: 1705.06225 [astro-ph.CO].

[128] A. D. Gow, C. T. Byrnes, and A. Hall. “Accurate model for the primordial black hole mass distribution from a peak in the power spectrum”. *Phys. Rev. D* 105.2 (2022), p. 023503. arXiv: 2009.03204 [astro-ph.CO].

[129] A. D. Gow et al. “The power spectrum on small scales: Robust constraints and comparing PBH methodologies”. *JCAP* 02 (2021), p. 002. arXiv: 2008.03289 [astro-ph.CO].

[130] O. Özsoy and G. Tasinato. “Inflation and Primordial Black Holes”. *Universe* 9.5 (2023), p. 203. arXiv: 2301.03600 [astro-ph.CO].

[131] H. Motohashi and W. Hu. “Primordial Black Holes and Slow-Roll Violation”. *Phys. Rev. D* 96.6 (2017), p. 063503. arXiv: 1706.06784 [astro-ph.CO].

[132] N. C. Tsamis and R. P. Woodard. “Improved estimates of cosmological perturbations”. *Phys. Rev. D* 69 (2004), p. 084005. arXiv: astro-ph/0307463.

[133] W. H. Kinney. “Horizon crossing and inflation with large eta”. *Phys. Rev. D* 72 (2005), p. 023515. arXiv: gr-qc/0503017.

[134] C. Pattison et al. “Quantum diffusion during inflation and primordial black holes”. *JCAP* 10 (2017), p. 046. arXiv: 1707.00537 [hep-th].

[135] J. M. Ezquiaga, J. García-Bellido, and V. Vennin. “The exponential tail of inflationary fluctuations: consequences for primordial black holes”. *JCAP* 03 (2020), p. 029. arXiv: 1912.05399 [astro-ph.CO].

[136] J. Kristiano and J. Yokoyama. "Constraining Primordial Black Hole Formation from Single-Field Inflation". *Phys. Rev. Lett.* 132.22 (2024), p. 221003. arXiv: 2211.03395 [hep-th].

[137] A. Riotto. "The Primordial Black Hole Formation from Single-Field Inflation is Not Ruled Out" (2023). arXiv: 2301.00599 [astro-ph.CO].

[138] J. Fumagalli. "Absence of one-loop effects on large scales from small scales in non-slow-roll dynamics" (2023). arXiv: 2305.19263 [astro-ph.CO].

[139] H. Firouzjahi and A. Riotto. "Primordial Black Holes and loops in single-field inflation". *JCAP* 02 (2024), p. 021. arXiv: 2304.07801 [astro-ph.CO].

[140] H. Firouzjahi. "Revisiting loop corrections in single field ultraslow-roll inflation". *Phys. Rev. D* 109.4 (2024), p. 043514. arXiv: 2311.04080 [astro-ph.CO].

[141] K. Inomata. "Curvature Perturbations Protected Against One Loop" (2024). arXiv: 2403.04682 [astro-ph.CO].

[142] A. D. Linde. "Hybrid inflation". *Phys. Rev. D* 49 (1994), pp. 748–754. arXiv: astro-ph/9307002.

[143] E. J. Copeland et al. "False vacuum inflation with Einstein gravity". *Phys. Rev. D* 49 (1994), pp. 6410–6433. arXiv: astro-ph/9401011.

[144] S. Clesse, B. Garbrecht, and Y. Zhu. "Non-Gaussianities and Curvature Perturbations from Hybrid Inflation". *Phys. Rev. D* 89.6 (2014), p. 063519. arXiv: 1304.7042 [astro-ph.CO].

[145] S. Clesse and J. García-Bellido. "Massive Primordial Black Holes from Hybrid Inflation as Dark Matter and the seeds of Galaxies". *Phys. Rev. D* 92.2 (2015), p. 023524.

[146] I. D. Stamou. "Exploring critical overdensity thresholds in inflationary models of primordial black holes formation". *Phys. Rev. D* 108.6 (2023), p. 063515. arXiv: 2306.02758 [astro-ph.CO].

[147] Y. Ali-Haïmoud. "Correlation Function of High-Threshold Regions and Application to the Initial Small-Scale Clustering of Primordial Black Holes". *Phys. Rev. Lett.* 121.8 (2018), p. 081304. arXiv: 1805.05912 [astro-ph.CO].

[148] V. Desjacques and A. Riotto. "Spatial clustering of primordial black holes". *Phys. Rev. D* 98.12 (2018), p. 123533. arXiv: 1806.10414 [astro-ph.CO].

[149] N. Afshordi, P. McDonald, and D. N. Spergel. "Primordial black holes as dark matter: The Power spectrum and evaporation of early structures". *Astrophys. J. Lett.* 594 (2003), pp. L71–L74. arXiv: astro-ph/0302035.

[150] D. Inman and Y. Ali-Haïmoud. "Early structure formation in primordial black hole cosmologies". *Phys. Rev. D* 100.8 (2019), p. 083528. arXiv: 1907.08129 [astro-ph.CO].

[151] Y. Tada and S. Yokoyama. "Primordial black holes as biased tracers". *Phys. Rev. D* 91.12 (2015), p. 123534. arXiv: 1502.01124 [astro-ph.CO].

[152] S. Young and C. T. Byrnes. "Signatures of non-gaussianity in the isocurvature modes of primordial black hole dark matter". *JCAP* 04 (2015), p. 034. arXiv: 1503.01505 [astro-ph.CO].

[153] T. Suyama and S. Yokoyama. "Clustering of primordial black holes with non-Gaussian initial fluctuations". *PTEP* 2019.10 (2019), 103E02. arXiv: 1906.04958 [astro-ph.CO].

[154] A. M. Green and B. J. Kavanagh. "Primordial Black Holes as a dark matter candidate". *J. Phys. G* 48.4 (2021), p. 043001. arXiv: 2007.10722 [astro-ph.CO].

[155] B. Carr and F. Kuhnel. "Primordial Black Holes as Dark Matter: Recent Developments". *Ann. Rev. Nucl. Part. Sci.* 70 (2020), pp. 355–394. arXiv: 2006.02838 [astro-ph.CO].

[156] B. Carr et al. "Constraints on primordial black holes". *Rept. Prog. Phys.* 84.11 (2021), p. 116902. arXiv: 2002.12778 [astro-ph.CO].

[157] P. Villanueva-Domingo, O. Mena, and S. Palomares-Ruiz. "A brief review on primordial black holes as dark matter". *Front. Astron. Space Sci.* 8 (2021), p. 87. arXiv: 2103.12087 [astro-ph.CO].

[158] B. J. Kavanagh. *PBHbounds*. https://doi.org/10.5281/zenodo.3538999. Accessed: 07-09-2024. 2019.

[159] M. Boudaud and M. Cirelli. "Voyager 1 $e^{\pm}$ Further Constrain Primordial Black Holes as Dark Matter". *Phys. Rev. Lett.* 122.4 (2019), p. 041104.

[160] M. Korwar and S. Profumo. "Updated constraints on primordial black hole evaporation". *JCAP* 05 (2023), p. 054.

[161] C. V. Müller and J. Miralda-Escudé. "Limits on Dark Matter Compact Objects implied by Supermagnified Stars in Lensing Clusters" (2024). arXiv: 2403.16989 [astro-ph.CO].

[162] J. Auffinger. "Primordial black hole constraints with Hawking radiation—A review". *Prog. Part. Nucl. Phys.* 131 (2023), p. 104040. arXiv: 2206.02672 [astro-ph.CO].

[163] B. J. Carr et al. "New cosmological constraints on primordial black holes". *Phys. Rev. D* 81 (2010), p. 104019. arXiv: 0912.5297 [astro-ph.CO].

[164] B. Dasgupta, R. Laha, and A. Ray. "Neutrino and positron constraints on spinning primordial black hole dark matter". *Phys. Rev. Lett.* 125.10 (2020), p. 101101. arXiv: 1912.01014 [hep-ph].

[165] N. Bernal et al. "Current and future neutrino limits on the abundance of primordial black holes". *JCAP* 10 (2022), p. 068. arXiv: 2203.14979 [hep-ph].

[166] V. Poulin, J. Lesgourgues, and P. D. Serpico. "Cosmological constraints on exotic injection of electromagnetic energy". *JCAP* 03 (2017), p. 043. arXiv: 1610.10051 [astro-ph.CO].

[167] P. Stöcker et al. "Exotic energy injection with ExoCLASS: Application to the Higgs portal model and evaporating black holes". *JCAP* 03 (2018), p. 018. arXiv: 1801.01871 [astro-ph.CO].

[168] S. K. Acharya and R. Khatri. "CMB and BBN constraints on evaporating primordial black holes revisited". *JCAP* 06 (2020), p. 018. arXiv: 2002.00898 [astro-ph.CO].

[169] J. Cang, Y. Gao, and Y.-Z. Ma. "21-cm constraints on spinning primordial black holes". *JCAP* 03.03 (2022), p. 012. arXiv: 2108.13256 [astro-ph.CO].

[170] P. De la Torre Luque, J. Koechler, and S. Balaji. "Refining Galactic primordial black hole evaporation constraints" (2024). arXiv: 2406.11949 [astro-ph.HE].

[171] B.-Y. Su et al. "Constraining primordial black holes as dark matter using AMS-02 data". *Eur. Phys. J. C* 84.6 (2024), p. 606. arXiv: 2403.04988 [astro-ph.HE].

[172] J. Iguaz et al. "Isotropic X-ray bound on Primordial Black Hole Dark Matter". *Phys. Rev. D* 103.10 (2021). [Erratum: Phys.Rev.D 107, 069902 (2023)], p. 103025. arXiv: 2104.03145 [astro-ph.CO].

[173] W. DeRocco and P. W. Graham. "Constraining Primordial Black Hole Abundance with the Galactic 511 keV Line". *Phys. Rev. Lett.* 123.25 (2019), p. 251102. arXiv: 1906.07740 [astro-ph.CO].

[174] R. Laha. "Primordial Black Holes as a Dark Matter Candidate Are Severely Constrained by the Galactic Center 511 keV γ -Ray Line". *Phys. Rev. Lett.* 123.25 (2019), p. 251101. arXiv: 1906.09994 [astro-ph.HE].

[175] C. Keith and D. Hooper. "511 keV excess and primordial black holes". *Phys. Rev. D* 104.6 (2021), p. 063033. arXiv: 2103.08611 [astro-ph.CO].

[176] J. Auffinger. "Limits on primordial black holes detectability with Isatis: a BlackHawk tool". *Eur. Phys. J. C* 82.4 (2022), p. 384.

[177] S. Mittal et al. "Constraining primordial black holes as dark matter using the global 21-cm signal with X-ray heating and excess radio background". *JCAP* 03 (2022), p. 030. arXiv: 2107.02190 [astro-ph.CO].

[178] A. K. Saha and R. Laha. "Sensitivities on nonspinning and spinning primordial black hole dark matter with global 21-cm troughs". *Phys. Rev. D* 105.10 (2022), p. 103026.

[179] S. Singh et al. "On the detection of a cosmic dawn signal in the radio background". *Nature Astron.* 6.5 (2022), pp. 607–617.

[180] S. Chen, H.-H. Zhang, and G. Long. "Revisiting the constraints on primordial black hole abundance with the isotropic gamma-ray background". *Phys. Rev. D* 105.6 (2022), p. 063008. arXiv: 2112.15463 [astro-ph.CO].

[181] J. Berteaud et al. "Strong constraints on primordial black hole dark matter from 16 years of INTEGRAL/SPI observations". *Phys. Rev. D* 106.2 (2022), p. 023030. arXiv: 2202.07483 [astro-ph.HE].

[182] B. Paczynski. "Gravitational microlensing by the galactic halo". *Astrophys. J.* 304 (1986), pp. 1–5.

[183] H. Niikura et al. "Microlensing constraints on primordial black holes with Subaru/HSC Andromeda observations". *Nature Astron.* 3.6 (2019), pp. 524–534.

[184] H. Niikura et al. "Constraints on Earth-mass primordial black holes from OGLE 5-year microlensing events". *Phys. Rev. D* 99.8 (2019), p. 083503. arXiv: 1901.07120 [astro-ph.CO].

[185] R. A. Allsman et al. "MACHO project limits on black hole dark matter in the 1-30 solar mass range". *Astrophys. J. Lett.* 550 (2001), p. L169. arXiv: astro-ph/0011506.

[186] P. Tisserand et al. "Limits on the Macho Content of the Galactic Halo from the EROS-2 Survey of the Magellanic Clouds". *Astron. Astrophys.* 469 (2007), pp. 387–404. arXiv: astro-ph/0607207.

[187] P. Mróz et al. "No massive black holes in the Milky Way halo". *Nature* 632.8026 (2024), pp. 749–751. arXiv: 2403.02386 [astro-ph.GA].

[188] C. Alcock et al. "The MACHO project first year LMC results: The Microlensing rate and the nature of the galactic dark halo". *Astrophys. J.* 461 (1996), p. 84. arXiv: astro-ph/9506113.

[189] M. R. S. Hawkins. "A new look at microlensing limits on dark matter in the Galactic halo". *Astron. Astrophys.* 575 (2015), A107. arXiv: 1503.01935 [astro-ph.GA].

[190] A. M. Green. "Astrophysical uncertainties on stellar microlensing constraints on multi-Solar mass primordial black hole dark matter". *Phys. Rev. D* 96.4 (2017), p. 043020. arXiv: 1705.10818 [astro-ph.CO].

[191] J. Calcino, J. Garcia-Bellido, and T. M. Davis. "Updating the MACHO fraction of the Milky Way dark halowith improved mass models". *Mon. Not. Roy. Astron. Soc.* 479.3 (2018), pp. 2889–2905. arXiv: 1803.09205 [astro-ph.CO].

[192] K. Chang and S. Refsdal. "Flux variations of QSO 0957+561 A, B and image splitting by stars near the light path". *Nature* 282 (1979), pp. 561–564.

[193] J. Wambsganss. "Gravitational Microlensing". *33rd Advanced Saas Fee Course on Gravitational Lensing: Strong, Weak, and Micro.* 2006, pp. 453–540. arXiv: astro-ph/0604278.

[194] A. Esteban-Gutiérrez et al. "Abundance of LIGO/Virgo Black Holes from Microlensing Observations of Quasars with Reverberation Mapping Size Estimates". *Astrophys. J.* 929.2 (2022), p. 123. arXiv: 2203.04777 [astro-ph.CO].

[195] A. Esteban-Gutiérrez et al. "Constraints on the Abundance of Primordial Black Holes from X-Ray Quasar Microlensing Observations: Substellar to Planetary Mass Range". *Astrophys. J.* 954.2 (2023), p. 172. arXiv: 2307.07473 [astro-ph.CO].

[196] J. Miralda-Escude. "The Magnification of Stars Crossing a Caustic. I. Lenses with Smooth Potentials". *Astrophysical Journal* 379 (1991), p. 94.

[197] P. L. Kelly et al. "Extreme magnification of an individual star at redshift 1.5 by a galaxy-cluster lens". *Nature Astron.* 2.4 (2018), pp. 334–342. arXiv: 1706.10279 [astro-ph.GA].

[198] T. Venumadhav, L. Dai, and J. Miralda-Escudé. "Microlensing of Extremely Magnified Stars near Caustics of Galaxy Clusters". *Astrophys. J.* 850.1 (2017), p. 49. arXiv: 1707.00003 [astro-ph.CO].

[199] M. Oguri et al. "Understanding caustic crossings in giant arcs: characteristic scales, event rates, and constraints on compact dark matter". *Phys. Rev. D* 97.2 (2018), p. 023518. arXiv: 1710.00148 [astro-ph.CO].

[200] J. M. Diego et al. "Dark Matter under the Microscope: Constraining Compact Dark Matter with Caustic Crossing Events". *Astrophys. J.* 857.1 (2018), p. 25. arXiv: 1706.10281 [astro-ph.CO].

[201] K. P. Rauch. "Gravitational Microlensing of High-Redshift Supernovae by Compact Objects". *Astrophysical Journal* 374 (1991), p. 83.

[202] M. Zumalacarregui and U. Seljak. "Limits on stellar-mass compact objects as dark matter from gravitational lensing of type Ia supernovae". *Phys. Rev. Lett.* 121.14 (2018), p. 141101. arXiv: 1712.02240 [astro-ph.CO].

[203] J. Garcia-Bellido, S. Clesse, and P. Fleury. "Primordial black holes survive SN lensing constraints". *Phys. Dark Univ.* 20 (2018), pp. 95–100. arXiv: 1712.06574 [astro-ph.CO].

[204] T. Nakamura et al. "Gravitational waves from coalescing black hole MACHO binaries". *Astrophys. J. Lett.* 487 (1997), pp. L139–L142. arXiv: astro-ph/9708060.

[205] K. Ioka et al. “Black hole binary formation in the expanding universe: Three body problem approximation”. *Phys. Rev. D* 58 (1998), p. 063003. arXiv: astro-ph/9807018.

[206] Y. Ali-Haïmoud, E. D. Kovetz, and M. Kamionkowski. “Merger rate of primordial black-hole binaries”. *Phys. Rev. D* 96.12 (2017), p. 123523. arXiv: 1709.06576 [astro-ph.CO].

[207] B. J. Kavanagh, D. Gaggero, and G. Bertone. “Merger rate of a subdominant population of primordial black holes”. *Phys. Rev. D* 98.2 (2018), p. 023536. arXiv: 1805.09034 [astro-ph.CO].

[208] A. H. Nitz and Y.-F. Wang. “Broad search for gravitational waves from subsolar-mass binaries through LIGO and Virgo’s third observing run”. *Phys. Rev. D* 106.2 (2022), p. 023024. arXiv: 2202.11024 [astro-ph.HE].

[209] M. Andrés-Carcasona et al. “Constraints on primordial black holes from LIGO-Virgo-KAGRA O3 events”. *Phys. Rev. D* 110.2 (2024), p. 023040. arXiv: 2405.05732 [astro-ph.CO].

[210] A. L. Miller et al. “Gravitational wave constraints on planetary-mass primordial black holes using LIGO O3a data” (2024). arXiv: 2402.19468 [gr-qc].

[211] S. Bird et al. “Did LIGO detect dark matter?” *Phys. Rev. Lett.* 116.20 (2016), p. 201301. arXiv: 1603.00464 [astro-ph.CO].

[212] S. Clesse and J. García-Bellido. “Detecting the gravitational wave background from primordial black hole dark matter”. *Phys. Dark Univ.* 18 (2017), pp. 105–114. arXiv: 1610.08479 [astro-ph.CO].

[213] G. Franciolini et al. “Primordial black hole mergers from three-body interactions”. *Phys. Rev. D* 106.8 (2022), p. 083529. arXiv: 2205.15340 [astro-ph.CO].

[214] M. Raidal, V. Vaskonen, and H. Veermäe. "Gravitational Waves from Primordial Black Hole Mergers". *JCAP* 09 (2017), p. 037. arXiv: 1707.01480 [astro-ph.CO].

[215] R. Abbott et al. "Upper limits on the isotropic gravitational-wave background from Advanced LIGO and Advanced Virgo's third observing run". *Phys. Rev. D* 104.2 (2021), p. 022004. arXiv: 2101.12130 [gr-qc].

[216] Z.-C. Chen and Q.-G. Huang. "Distinguishing Primordial Black Holes from Astrophysical Black Holes by Einstein Telescope and Cosmic Explorer". *JCAP* 08 (2020), p. 039. arXiv: 1904.02396 [astro-ph.CO].

[217] M. Raidal et al. "Formation and Evolution of Primordial Black Hole Binaries in the Early Universe". *JCAP* 02 (2019), p. 018. arXiv: 1812.01930 [astro-ph.CO].

[218] K. Jedamzik. "Primordial Black Hole Dark Matter and the LIGO/Virgo observations". *JCAP* 09 (2020), p. 022. arXiv: 2006.11172 [astro-ph.CO].

[219] V. Vaskonen and H. Veermäe. "Lower bound on the primordial black hole merger rate". *Phys. Rev. D* 101.4 (2020), p. 043015. arXiv: 1908.09752 [astro-ph.CO].

[220] V. Stasenko and K. Belotsky. "Influence of early dark matter haloes on the primordial black holes merger rate". *Mon. Not. Roy. Astron. Soc.* 526.3 (2023), pp. 4308–4314. arXiv: 2307.12924 [astro-ph.CO].

[221] T. Bringmann et al. "Towards closing the window of primordial black holes as dark matter: The case of large clustering". *Phys. Rev. D* 99.6 (2019), p. 063532. arXiv: 1808.05910 [astro-ph.CO].

[222] G. Ballesteros, P. D. Serpico, and M. Taoso. "On the merger rate of primordial black holes: effects of nearest neighbours distribution and clustering". *JCAP* 10 (2018), p. 043. arXiv: 1807.02084 [astro-ph.CO].

[223] V. Atal, A. Sanglas, and N. Triantafyllou. "LIGO/Virgo black holes and dark matter: The effect of spatial clustering". *JCAP* 11 (2020), p. 036. arXiv: 2007.07212 [astro-ph.CO].

[224] K. J. Mack, J. P. Ostriker, and M. Ricotti. "Growth of structure seeded by primordial black holes". *Astrophys. J.* 665 (2007), pp. 1277–1287. arXiv: astro-ph/0608642.

[225] J. Adamek et al. "WIMPs and stellar-mass primordial black holes are incompatible". *Phys. Rev. D* 100.2 (2019), p. 023506. arXiv: 1901.08528 [astro-ph.CO].

[226] S. Pilipenko, M. Tkachev, and P. Ivanov. "Evolution of a primordial binary black hole due to interaction with cold dark matter and the formation rate of gravitational wave events". *Phys. Rev. D* 105.12 (2022), p. 123504. arXiv: 2205.10792 [astro-ph.CO].

[227] P. Jangra, B. J. Kavanagh, and J. M. Diego. "Impact of dark matter spikes on the merger rates of Primordial Black Holes". *JCAP* 11 (2023), p. 069. arXiv: 2304.05892 [astro-ph.CO].

[228] M. Ricotti, J. P. Ostriker, and K. J. Mack. "Effect of Primordial Black Holes on the Cosmic Microwave Background and Cosmological Parameter Estimates". *Astrophys. J.* 680 (2008), p. 829. arXiv: 0709.0524 [astro-ph].

[229] Y. Ali-Haïmoud and M. Kamionkowski. "Cosmic microwave background limits on accreting primordial black holes". *Phys. Rev. D* 95.4 (2017), p. 043534. arXiv: 1612.05644 [astro-ph.CO].

[230] A. Hektor et al. "Constraining Primordial Black Holes with the EDGES 21-cm Absorption Signal". *Phys. Rev. D* 98.2 (2018), p. 023503. arXiv: 1803.09697 [astro-ph.CO].

[231] D. Gaggero et al. "Searching for Primordial Black Holes in the radio and X-ray sky". *Phys. Rev. Lett.* 118.24 (2017), p. 241101. arXiv: 1612.00457 [astro-ph.HE].

[232] J. Manshanden et al. "Multi-wavelength astronomical searches for primordial black holes". *JCAP* 06 (2019), p. 026. arXiv: 1812.07967 [astro-ph.HE].

[233] Y. Inoue and A. Kusenko. "New X-ray bound on density of primordial black holes". *JCAP* 10 (2017), p. 034. arXiv: 1705.00791 [astro-ph.CO].

[234] P. Lu et al. "Constraining Primordial Black Holes with Dwarf Galaxy Heating". *Astrophys. J. Lett.* 908.2 (2021), p. L23. arXiv: 2007.02213 [astro-ph.CO].

[235] V. Takhistov et al. "Interstellar gas heating by primordial black holes". *JCAP* 03.03 (2022), p. 017. arXiv: 2105.06099 [astro-ph.GA].

[236] V. Poulin et al. "CMB bounds on disk-accreting massive primordial black holes". *Phys. Rev. D* 96.8 (2017), p. 083524. arXiv: 1707.04206 [astro-ph.CO].

[237] L. Piga et al. "The effect of outflows on CMB bounds from Primordial Black Hole accretion". *JCAP* 12 (2022), p. 016. arXiv: 2210.14934 [astro-ph.CO].

[238] V. Bosch-Ramon and N. Bellomo. "Mechanical feedback effects on primordial black hole accretion". *Astron. Astrophys.* 638 (2020), A132. arXiv: 2004.11224 [astro-ph.CO].

[239] G. Facchinetti, M. Lucca, and S. Clesse. "Relaxing CMB bounds on primordial black holes: The role of ionization fronts". *Phys. Rev. D* 107.4 (2023), p. 043537. arXiv: 2212.07969 [astro-ph.CO].

[240] D. Agius et al. "Feedback in the dark: a critical examination of CMB bounds on primordial black holes". *JCAP* 07 (2024), p. 003. arXiv: 2403.18895 [hep-ph].

[241] G. Hütsi, M. Raidal, and H. Veermäe. "Small-scale structure of primordial black hole dark matter and its implications for accretion". *Phys. Rev. D* 100.8 (2019), p. 083016. arXiv: 1907.06533 [astro-ph.CO].

[242] P. D. Serpico et al. "Cosmic microwave background bounds on primordial black holes including dark matter halo accretion". *Phys. Rev. Res.* 2.2 (2020), p. 023204. arXiv: 2002.10771 [astro-ph.CO].

[243] T. D. Brandt. "Constraints on MACHO Dark Matter from Compact Stellar Systems in Ultra-Faint Dwarf Galaxies". *Astrophys. J. Lett.* 824.2 (2016), p. L31. arXiv: 1605.03665 [astro-ph.GA].

[244] P. W. Graham and H. Ramani. "Constraints on Dark Matter from Dynamical Heating of Stars in Ultrafaint Dwarfs. Part 1: MACHOs and Primordial Black Holes" (2023). arXiv: 2311.07654 [hep-ph].

[245] S. M. Koushiappas and A. Loeb. "Dynamics of Dwarf Galaxies Disfavor Stellar-Mass Black Holes as Dark Matter". *Phys. Rev. Lett.* 119.4 (2017), p. 041102. arXiv: 1704.01668 [astro-ph.GA].

[246] Q. Zhu et al. "Primordial Black Holes as Dark Matter: Constraints From Compact Ultra-Faint Dwarfs". *Mon. Not. Roy. Astron. Soc.* 476.1 (2018), pp. 2–11. arXiv: 1710.05032 [astro-ph.CO].

[247] J. Stegmann et al. “Improved constraints from ultra-faint dwarf galaxies on primordial black holes as dark matter”. *Mon. Not. Roy. Astron. Soc.* 492.4 (2020), pp. 5247–5260. arXiv: 1910.04793 [astro-ph.GA].

[248] J. N. Bahcall, P. Hut, and S. Tremaine. “Maximum mass of objects that constitute unseen disk material”. *Astrophysical Journal* 290 (1985), pp. 15–20.

[249] J. Yoo, J. Chaname, and A. Gould. “The end of the MACHO era: limits on halo dark matter from stellar halo wide binaries”. *Astrophys. J.* 601 (2004), pp. 311–318. arXiv: astro-ph/0307437.

[250] D. P. Quinn et al. “On the Reported Death of the MACHO Era”. *Mon. Not. Roy. Astron. Soc.* 396 (2009), p. 11. arXiv: 0903.1644 [astro-ph.GA].

[251] M. A. Monroy-Rodríguez and C. Allen. “The end of the MACHO era, revisited: new limits on MACHO masses from halo wide binaries”. *Astrophys. J.* 790.2 (2014), p. 159. arXiv: 1406.5169 [astro-ph.GA].

[252] H.-J. Tian et al. “The Separation Distribution of Ultrawide Binaries across Galactic Populations”. *Astrophysical Journal, Supplement* 246.1, 4 (2020), p. 4. arXiv: 1909.04765 [astro-ph.GA].

[253] E. Tyler, A. M. Green, and S. P. Goodwin. “Modelling uncertainties in wide binary constraints on primordial black holes”. *Mon. Not. Roy. Astron. Soc.* 524.2 (2023), pp. 3052–3059. arXiv: 2207.08668 [astro-ph.GA].

[254] S. Young. “The primordial black hole formation criterion re-examined: Parametrisation, timing and the choice of window function”. *Int. J. Mod. Phys. D* 29.02 (2019), p. 2030002. arXiv: 1905.01230 [astro-ph.CO].

[255] B. J. Carr and J. E. Lidsey. "Primordial black holes and generalized constraints on chaotic inflation". *Phys. Rev. D* 48 (1993), pp. 543–553.

[256] K. Kohri, T. Nakama, and T. Suyama. "Testing scenarios of primordial black holes being the seeds of supermassive black holes by ultracompact minihalos and CMB μ-distortions". *Phys. Rev. D* 90.8 (2014), p. 083514. arXiv: 1405.5999 [astro-ph.CO].

[257] T. Nakama, T. Suyama, and J. Yokoyama. "Supermassive black holes formed by direct collapse of inflationary perturbations". *Phys. Rev. D* 94.10 (2016), p. 103522. arXiv: 1609.02245 [gr-qc].

[258] T. Nakama, B. Carr, and J. Silk. "Limits on primordial black holes from μ distortions in cosmic microwave background". *Phys. Rev. D* 97.4 (2018), p. 043525. arXiv: 1710.06945 [astro-ph.CO].

[259] C. T. Byrnes, J. Lesgourgues, and D. Sharma. "Robust μ-distortion constraints on primordial supermassive black holes from non-Gaussian perturbations" (2024). arXiv: 2404.18475 [astro-ph.CO].

[260] S. Mollerach, D. Harari, and S. Matarrese. "CMB polarization from secondary vector and tensor modes". *Phys. Rev. D* 69 (2004), p. 063002. arXiv: astro-ph/0310711.

[261] K. N. Ananda, C. Clarkson, and D. Wands. "The Cosmological gravitational wave background from primordial density perturbations". *Phys. Rev. D* 75 (2007), p. 123518. arXiv: gr-qc/0612013.

[262] D. Baumann et al. "Gravitational Wave Spectrum Induced by Primordial Scalar Perturbations". *Phys. Rev. D* 76 (2007), p. 084019. arXiv: hep-th/0703290.

[263] R. Saito and J. Yokoyama. "Gravitational wave background as a probe of the primordial black hole abundance". *Phys. Rev. Lett.* 102 (2009). [Erratum: Phys.Rev.Lett. 107, 069901 (2011)], p. 161101. arXiv: 0812.4339 [astro-ph].

[264] A. J. Iovino et al. "Curbing PBHs with PTAs" (2024). arXiv: 2406.20089 [astro-ph.CO].

[265] G. Agazie et al. "The NANOGrav 15 yr Data Set: Evidence for a Gravitational-wave Background". *Astrophys. J. Lett.* 951.1 (2023), p. L8. arXiv: 2306.16213 [astro-ph.HE].

[266] G. Agazie et al. "The NANOGrav 15 yr Data Set: Observations and Timing of 68 Millisecond Pulsars". *Astrophys. J. Lett.* 951.1 (2023), p. L9. arXiv: 2306.16217 [astro-ph.HE].

[267] K. Inomata, M. Kawasaki, and Y. Tada. "Revisiting constraints on small scale perturbations from big-bang nucleosynthesis". *Phys. Rev. D* 94.4 (2016), p. 043527. arXiv: 1605.04646 [astro-ph.CO].

[268] R. Murgia et al. "Lyman-α Forest Constraints on Primordial Black Holes as Dark Matter". *Phys. Rev. Lett.* 123.7 (2019), p. 071102. arXiv: 1903.10509 [astro-ph.CO].

[269] B. C. Lacki and J. F. Beacom. "Primordial Black Holes as Dark Matter: Almost All or Almost Nothing". *Astrophys. J. Lett.* 720 (2010), pp. L67–L71. arXiv: 1003.3466 [astro-ph.CO].

[270] E. U. Ginés, O. Mena, and S. J. Witte. "Revisiting constraints on WIMPs around primordial black holes". *Phys. Rev. D* 106.6 (2022), p. 063538. arXiv: 2207.09481 [astro-ph.CO].

[271] F. Capela, M. Pshirkov, and P. Tinyakov. "Constraints on primordial black holes as dark matter candidates from capture by neutron

stars". *Phys. Rev. D* 87.12 (2013), p. 123524. arXiv: 1301.4984 [astro-ph.CO].

[272] P. Pani and A. Loeb. "Tidal capture of a primordial black hole by a neutron star: implications for constraints on dark matter". *JCAP* 06 (2014), p. 026. arXiv: 1401.3025 [astro-ph.CO].

[273] P. Montero-Camacho et al. "Revisiting constraints on asteroid-mass primordial black holes as dark matter candidates". *JCAP* 08 (2019), p. 031. arXiv: 1906.05950 [astro-ph.CO].

[274] P. W. Graham, S. Rajendran, and J. Varela. "Dark Matter Triggers of Supernovae". *Phys. Rev. D* 92.6 (2015), p. 063007. arXiv: 1505.04444 [hep-ph].

[275] J. Smirnov et al. "White Dwarfs in Dwarf Spheroidal Galaxies: A New Class of Compact-Dark-Matter Detectors". *Phys. Rev. Lett.* 132.15 (2024), p. 151401. arXiv: 2211.00013 [astro-ph.CO].

[276] N. Esser and P. Tinyakov. "Constraints on primordial black holes from observation of stars in dwarf galaxies". *Phys. Rev. D* 107.10 (2023), p. 103052. arXiv: 2207.07412 [astro-ph.HE].

[277] A. Gould. "Femtolensing of Gamma-Ray Bursters". *Astrophysical Journal, Letters* 386 (1992), p. L5.

[278] A. Barnacka, J. F. Glicenstein, and R. Moderski. "New constraints on primordial black holes abundance from femtolensing of gamma-ray bursts". *Phys. Rev. D* 86 (2012), p. 043001. arXiv: 1204.2056 [astro-ph.CO].

[279] A. Katz et al. "Femtolensing by Dark Matter Revisited". *JCAP* 12 (2018), p. 005. arXiv: 1807.11495 [astro-ph.CO].

[280] R. J. Nemiroff and A. Gould. "Probing for MACHOs of mass 10^{-15}-solar-mass - 10^{-7}-solar-mass with gamma-ray burst parallax spacecraft". *Astrophys. J. Lett.* 452 (1995), p. L111. arXiv: astro-ph/9505019.

[281] S. Jung and T. Kim. "Gamma-ray burst lensing parallax: Closing the primordial black hole dark matter mass window". *Phys. Rev. Res.* 2.1 (2020), p. 013113. arXiv: 1908.00078 [astro-ph.CO].

[282] P. Gawade, S. More, and V. Bhalerao. "On the feasibility of primordial black hole abundance constraints using lensing parallax of GRBs". *Mon. Not. Roy. Astron. Soc.* 527.2 (2023), pp. 3306–3314. arXiv: 2308.01775 [astro-ph.CO].

[283] Y. Bai and N. Orlofsky. "Microlensing of X-ray Pulsars: a Method to Detect Primordial Black Hole Dark Matter". *Phys. Rev. D* 99.12 (2019), p. 123019. arXiv: 1812.01427 [astro-ph.HE].

[284] M. Tamta, N. Raj, and P. Sharma. "Breaking into the window of primordial black hole dark matter with x-ray microlensing" (2024). arXiv: 2405.20365 [astro-ph.HE].

[285] T. X. Tran et al. "Close encounters of the primordial kind: a new observable for primordial black holes as dark matter" (2023). arXiv: 2312.17217 [astro-ph.CO].

[286] B. Bertrand et al. "Observing dark matter clumps and asteroid-mass primordial black holes in the solar system with gravimeters and GNSS networks". arXiv: 2312.14520 [astro-ph.CO].

[287] B. Carr et al. "Primordial black hole constraints for extended mass functions". *Phys. Rev. D* 96.2 (2017), p. 023514. arXiv: 1705.05567 [astro-ph.CO].

[288] F. Kühnel and K. Freese. "Constraints on Primordial Black Holes with Extended Mass Functions". *Phys. Rev. D* 95.8 (2017), p. 083508. arXiv: 1701.07223 [astro-ph.CO].

[289] N. Bellomo et al. "Primordial Black Holes as Dark Matter: Converting Constraints from Monochromatic to Extended Mass Distributions". *JCAP* 01 (2018), p. 004. arXiv: 1709.07467 [astro-ph.CO].

[290] J. García-Bellido and S. Clesse. "Constraints from microlensing experiments on clustered primordial black holes". *Phys. Dark Univ.* 19 (2018), pp. 144–148. arXiv: 1710.04694 [astro-ph.CO].

[291] R. I. Epstein. "Proto-galactic perturbations". *Mon. Not. Roy. Astron. Soc.* 205 (1983), pp. 207–229.

[292] G. Pietrzyński et al. "A distance to the Large Magellanic Cloud that is precise to one per cent". *Nature* 567.7747 (2019), pp. 200–203. arXiv: 1903.08096 [astro-ph.GA].

[293] K. Griest. "Galactic Microlensing as a Method of Detecting Massive Compact Halo Objects". *Astrophysical Journal* 366 (1991), p. 412.

[294] R. Abuter et al. "A geometric distance measurement to the Galactic center black hole with 0.3% uncertainty". *Astron. Astrophys.* 625 (2019). arXiv: 1904.05721 [astro-ph.GA].

[295] M. Petač, J. Lavalle, and K. Jedamzik. "Microlensing constraints on clustered primordial black holes". *Phys. Rev. D* 105.8 (2022), p. 083520. arXiv: 2201.02521 [astro-ph.CO].

[296] E. Maoz. "Gravitational Microlensing by Dark Clusters in the Galactic Halo". *Astrophysical Journal, Letters* 428 (1994), p. L5. arXiv: astro-ph/9402027 [astro-ph].

[297] R. B. Metcalf and J. Silk. "Gravitational microlensing by clustered MACHOs". *Astrophys. J.* 464 (1996), p. 218. arXiv: astro-ph/9509127.

[298] S. Mao. "Introduction to Gravitational Microlensing" (2008). arXiv: 0811.0441 [astro-ph].

[299] T. Blaineau et al. "New limits from microlensing on Galactic black holes in the mass range 10 $M_\odot$ < M < 1000 $M_\odot$". *Astron. Astrophys.* 664 (2022), A106. arXiv: 2202.13819 [astro-ph.GA].

[300] A. Mirhosseini and M. Moniez. "The MEMO project: Combining all microlensing surveys to search for intermediate-mass Galactic black holes". *Astron. Astrophys.* 618 (2018), p. L4. arXiv: 1711.10898 [astro-ph.GA].

[301] M. Gorton and A. M. Green. "Effect of clustering on primordial black hole microlensing constraints". *JCAP* 08.08 (2022), p. 035. arXiv: 2203.04209 [astro-ph.CO].

[302] P. Tisserand et al. "EROS 2 photometry of probable R Coronae Borealis stars in the Small Magellanic Cloud". *Astron. Astrophys.* 424 (2004), pp. 245–252. arXiv: astro-ph/0405551.

[303] V. De Luca et al. "Ruling Out Initially Clustered Primordial Black Holes as Dark Matter". *Phys. Rev. Lett.* 129.19 (2022), p. 191302. arXiv: 2208.01683 [astro-ph.CO].

[304] B. Carter. "Charge and particle conservation in black hole decay". *Phys. Rev. Lett.* 33 (1974), pp. 558–561.

[305] D. N. Page. "Particle Emission Rates from a Black Hole. 3. Charged Leptons from a Nonrotating Hole". *Phys. Rev. D* 16 (1977), pp. 2402–2411.

[306] D. Croon et al. "Subaru-HSC through a different lens: Microlensing by extended dark matter structures". *Phys. Rev. D* 102.8 (2020), p. 083021.

[307] A. Coogan et al. "Hunting for dark matter and new physics with GECCO". *Phys. Rev. D* 107.2 (2023), p. 023022. arXiv: 2101.10370 [astro-ph.HE].

[308] S. Sugiyama, T. Kurita, and M. Takada. "On the wave optics effect on primordial black hole constraints from optical microlensing search". *Mon. Not. Roy. Astron. Soc.* 493.3 (2020), pp. 3632–3641. arXiv: 1905.06066 [astro-ph.CO].

[309] A. Coogan, L. Morrison, and S. Profumo. "Direct Detection of Hawking Radiation from Asteroid-Mass Primordial Black Holes". *Phys. Rev. Lett.* 126.17 (2021), p. 171101. arXiv: 2010.04797 [astro-ph.CO].

[310] A. Ray et al. "Near future MeV telescopes can discover asteroid-mass primordial black hole dark matter". *Phys. Rev. D* 104.2 (2021), p. 023516. arXiv: 2102.06714 [astro-ph.CO].

[311] N. Smyth et al. "Updated Constraints on Asteroid-Mass Primordial Black Holes as Dark Matter". *Phys. Rev. D* 101.6 (2020), p. 063005. arXiv: 1910.01285 [astro-ph.CO].

[312] C. Germani and R. K. Sheth. "The Statistics of Primordial Black Holes in a Radiation-Dominated Universe: Recent and New Results". *Universe* 9.9 (2023), p. 421. arXiv: 2308.02971 [astro-ph.CO].

[313] B. J. Carr et al. "Constraints on primordial black holes from the Galactic gamma-ray background". *Phys. Rev. D* 94.4 (2016), p. 044029. arXiv: 1604.05349 [astro-ph.CO].

[314] Y.-F. Cai et al. “Cosmological standard timers from unstable primordial relics”. *Eur. Phys. J. C* 83.10 (2023), p. 913. arXiv: 2112.10422 [astro-ph.CO].

[315] M. R. Mosbech and Z. S. C. Picker. “Effects of Hawking evaporation on PBH distributions”. *SciPost Phys.* 13.4 (2022), p. 100. arXiv: 2203.05743 [astro-ph.HE].

[316] X. Boluna et al. “Searching for Exploding black holes”. *JCAP* 04 (2024), p. 024. arXiv: 2307.06467 [astro-ph.HE].

[317] A. Arbey and J. Auffinger. “BlackHawk: A public code for calculating the Hawking evaporation spectra of any black hole distribution”. *Eur. Phys. J. C* 79.8 (2019), p. 693. arXiv: 1905.04268 [gr-qc].

[318] A. Arbey and J. Auffinger. “Physics Beyond the Standard Model with BlackHawk v2.0”. *Eur. Phys. J. C* 81 (2021), p. 910. arXiv: 2108.02737 [gr-qc].

[319] D. N. Page and S. W. Hawking. “Gamma rays from primordial black holes”. *Astrophys. J.* 206 (1976), pp. 1–7.